
TIME-RESOLVED HIGH-RESOLUTION SPECTROSCOPY
OF CARBON DIMER ANION C_2^-
IN A CRYOGENIC ION STORAGE RING RICE

極低温イオン蓄積リング RICE を用いた
 C_2^- イオンの時間分解高分解能分光

A dissertation submitted to
the Graduate School of Science of Rikkyo University

by

MASATOMI IIZAWA

in partial fulfilment of the requirements for
the degree of Doctor of Philosophy

January, 2023

Abstract

二原子炭素 C_2 は炭素原子 2 個から成る最も単純な炭素分子であり、有機物や炭素同素体をはじめとする様々な物質の構成要素として、物理化学的性質や生成・崩壊の過程が詳細に調べられてきた。その負イオン C_2^- は 1954 年に実験室で発見され、分子としては電子親和力が極めて大きいこと、それゆえ基底状態 $X^2\Sigma_g^+$ 以外に複数の束縛状態（電子励起状態 $A^2\Pi_u$ と $B^2\Sigma_u^+$ ）を持つことが、分光学的な研究と量子化学計算によって明らかにされてきた。このような特異な性質を持った C_2^- は、宇宙分野では星間ガスや恒星を構成する重要な分子の 1 つである可能性が指摘されており、また、レーザー科学分野では分子負イオンとして初めてレーザー冷却の対象として提唱されるなど、広い分野で高い関心を集めている。しかし C_2^- の持つ複雑な電子構造ゆえにその反応や遷移過程は十分に理解されておらず、孤立系の振動緩和のような単分子過程ですら未解明の現象が多く見つかっている。

例えば、 C_2^- が ms オーダーで電子を放出して緩和する自動電子脱離過程が、複数の実験で観測されているがその起源は明らかでない。いくつかの理論研究は長い寿命 (\sim ms) をもった電子スピン四重項状態 ($4\Sigma_u^+$ など) の存在を示唆しているが、最新の量子化学計算では否定的な結果が得られている。このような問題が生じるのは、分子負イオンの形成には電子相関相互作用の寄与が相対的に大きく、また電子波動関数の空間拡がりが大きいため、正イオンに比べて高精度な計算が難しいからである。そこで本研究では高分解能レーザー分光により C_2^- の電子構造および緩和過程を実験的に明らかにすることを目指し、 C_2^- の振動回転スペクトルとその時間変化に関する研究を行った。

近年開発された理化学研究所の極低温イオン蓄積リング RICE (RIKEN Cryogenic Electrostatic ring) に C_2^- ビームを蓄積してレーザー分光を行った。本研究では、セシウムスパッタイオン源によって C_2^- ビームを生成、パルス化して入射する新しいビームラインの開発を行い、さらに光パラメトリック発振 (OPO) レーザーによる分光セットアップを独自に構築した。これによって高励起状態を含む「高温」の C_2^- ビームを生成し、赤外輻射のない極低温環境下で分光することが可能になり、その時間変化から、これまでになく知見を得られるようになった。

まず、 C_2^- ビームを RICE に蓄積し、生成された中性粒子の数の時間変化を観測したところ時定数 2.9 ms の減衰成分が観測された。この減衰成分は既に先行研究で報告されている、高温 C_2^- イオンの自動電子脱離 $C_2^{*-} \rightarrow C_2 + e^-$ にともなうものと考えられるが、上述のようにその起源は未解明である。

次に、10 ms 蓄積後に波長可変可視パルスレーザーを導入し、光脱離 $C_2^- + h\nu \rightarrow C_2 + e^-$ によって生成された中性 C_2 分子を検出することで光脱離スペクトルを得た。スペクトルシミュレーションプログラム PGOPHOR を用いてピークの同定を行い、 $B^2\Sigma_u^+$ 状態の $v' = 5-8$ の分光定数を導出した。本研究で得られた回転定数は先行研究より精度が改善されており、今回得られた回転定数が量子化学計算を行う際のベンチマークとなることが期待される。本研究で測定した光脱離スペクトルには、既知の $B^2\Sigma_u^+ - X^2\Sigma_g^+$, $A^2\Pi_u - X^2\Sigma_g^+$ 間の遷移では説明できないピークが多数観測された。これら未同定ピークの起源を追究するため、蓄積時間を 0.1–80 ms の範囲で変化させてスペクトルの強度変化を観測した。その結果、複数のピークについて、その強度が 1.5 ms から 3 ms の時定数で減衰することを発見した。これは自動電子脱離の時定数 2.9 ms と非常によく一致しており、観測された未同定の状態が自動電子脱離を引き起こしていると考えられる。また、これ以外にも基底

状態 $X^2\Sigma_g^+$ 以外に 100 ms を超える長寿命の状態が存在することが明らかになった。これは、 $X^2\Sigma_g^+$, $A^2\Pi_u$, $B^2\Sigma_u^+$ 状態以外に束縛励起状態が存在する可能性を示唆している。

以上のように本研究では、近年開発された極低温イオン蓄積技術を基礎として、炭素分子負イオン C_2^- の時間分解高分解能分光を行った。これにより、既知の束縛状態 ($X^2\Sigma_g^+$, $A^2\Pi_u$, $B^2\Sigma_u^+$) 以外に長寿命の束縛状態が存在し、これが長年未解決である ms オーダーの自動電子脱離に関与していることを強く示唆する結論を導き出した。未同定ピークの起源については未だ分かっていないものの、本研究成果は C_2^- および多様な分子負イオンの電子構造の詳細を明らかにする糸口として、今後多くの実験、理論研究の発端となることが期待される。

Contents

Abstract		i
Chapter 1	Introduction	1
	1.0.1 Background	1
	1.0.2 The aim of this study	2
	1.0.3 Structure of this thesis	2
1.1	Spectroscopy of diatomic molecules	4
	1.1.1 Electronic structure and selection rule	4
	1.1.2 Vibrational structure	8
	1.1.3 Rotational structure	10
1.2	Outline of the previous spectroscopic studies of carbon dimer anion	26
	1.2.1 Electronic state of C_2^-	26
	1.2.2 Adiabatic electron affinity of C_2	28
	1.2.3 Spectroscopy of the ground state and bound excited states	31
	1.2.4 Electronic and vibrational relaxation processes of the bound excited states and the ground states	36
	1.2.5 Autodetachment from $B^2\Sigma_u^+$ state	36
	1.2.6 Earlier experiments with ion storage rings and ion trap on autodetachment of C_2^-	37
Chapter 2	Experimental method	39
	2.1 Photodetachment spectroscopy	39
	2.2 Ion source and mass selection	43
	2.3 Cryogenic electrostatic ion storage ring RICE	47
	2.4 Tunable laser	50
	2.5 Neutral particle detector	52
Chapter 3	Result and discussion	55
	3.1 Counting detached neutral particles without laser	55
	3.2 Laser-induced photodetachment spectroscopy: the $B-X$ transition	56
	3.3 Laser-induced photodetachment spectroscopy and temporal evolution	61
	3.4 Normalization for spectra of each storage time	63
	3.5 Lifetime analysis of the unassigned peaks	67
	3.6 Negative ion formation in the cesium-sputter source	84

Chapter 4	Conclusions	87
AppendixA	State-selective ion–Neutral low-energy collision experiments	89
A.1	Background from astrochemistry	89
A.2	Overview : merged beam experiment	90
A.3	Overview : neutral beam source	91
A.3.1	Requirement of neutral beam source	91
A.3.2	Neutral carbon atomic beam	91
A.3.3	Brief evaluation of neutral beam source	94
A.4	Outlook: merged beam experiment with RICE	94
	Acknowledgements	99
	Bibliography	101
	List of Publications	119

Chapter 1

Introduction

1.0.1 Background

Diatomic carbon C_2 is the simplest carbon molecule consisting of two carbon atoms. As a constituent of various substances including organic materials, its physicochemical properties and formation and decay processes have been studied in detail.

This anion, C_2^- appears as a reactant and product in various chemical reactions in the chemical vapor deposition of diamonds [1] and the formation of C_2^- in the gas phase when graphite is heated [2, 3], discharged by radio frequency [4], vaporized by laser [5–7], or bombarded with argon ion [8–12] and cesium ion [13–15]. The existence of C_2^- in the late-type star, comet, and interstellar medium has attracted much attention.^{*1} Furthermore, in the field of laser science, it was the first molecular anion to be proposed as a target for laser cooling [44]. Thus, it has attracted high interest in a wide range of fields.

Since the diatomic carbon anion C_2^- was successfully isolated via mass spectrometry by Honig in 1954 [2], the C_2^- anion is one of the most studied molecular anions in the gas phase. The spectroscopic studies and quantum chemical calculations have revealed that the molecule has a large electron affinity (see § 1.2.2) and, therefore, multiple electronic excited states under the electron detachment threshold, called bound excited states (see § 1.2.1). The currently known bound excited states are $A^2\Pi_u$ and $B^2\Sigma_u^+$, and there are numerous theoretical calculations and spectroscopic studies (see § 1.2.3). However, due to the complex electronic structure of C_2^- , its reaction and transition processes, such as vibrational relaxation in isolated systems, have not yet been elucidated.

^{*1} There are some proposals that C_2^- may be observed in late-type stars such as carbon stars, but there are no reports of the observation of C_2^- [16–20]. On the other hand, the neutral C_2 was observed in carbon stars [21–24], supergiant star [25], and post-asymptotic giant branch star [26]. The existence of neutral C_2 has long been proposed in an interstellar [27] and it has been observed [28–34]. It has also been proposed that C_2^- can be formed by proton transfer of C_2H in an interstellar medium [35]. The radiative attachment ($C_2 + e^- \rightarrow C_2^{*-} \rightarrow C_2^- + h\nu$), charge transfer ($C_2 + X^- \rightarrow C_2^- + X$), and dissociative attachment ($C_2X + e^- \rightarrow C_2^- + X$) were also the candidate of major process of creating C_2^- in a diffuse cloud [36]. However C_2^- have not been observed. C_2^- has been observed in comets [37–40]. The presence of neutral C_2 in comets has also long been proposed [41] and has been observed [37–39, 42, 43].

1.0.2 The aim of this study

C_2^- has excited states above photodetachment threshold that undergo the electron emission on the time scale of ms, as evidenced by lifetime measurements in ion storage rings [45–48] and ion trap [49]. This relaxation process is called *autodetachment*. However electronic configuration of the autodetaching state is clearly known.

Several calculations have been performed for highly excited electronic states not only of $A^2\Pi_u$ state and $B^2\Sigma_u^+$ state (e.g., $^4\Sigma_u^+$). Earlier calculations have shown that some highly excited electronic states have bounded [50–52], and recent modern calculations with a large basis set implied there are no boundary excited states except $A^2\Pi_u$ and $B^2\Sigma_u^+$ states [53,54]. The difficulty of the quantum chemical calculation on molecular anions comes from the relatively large contribution of electron correlation to the formation of molecular anions and the large spatial broadening of the electronic wavefunction compared to cations. Additionally, the calculation of C_2^- has the difficulty that the ground state is nearly degenerated with the first bound excited state $A^2\Pi_u$.

Spectroscopic studies of C_2^- dawned with respect to the ground state $X^2\Sigma_g^+$ and the bounded excited states $A^2\Pi_u$ and $B^2\Sigma_u^+$ since the experimental study by Herzberg and Lagerqvist in 1968 [55]. However, the electronic excited states except $A^2\Pi_u$ and $B^2\Sigma_u^+$ states are not well known, although they have been suggested to play an important role in spectroscopic study and time evolution study of C_2^- . For instance, early spectroscopic experiments have shown that $B^2\Sigma_u^+ v' = 0 N' = 47$ and $v' = 1 N' = 30$ might be rotationally perturbed by $^4\Sigma_u^+$, and the energy levels are shifted [55]. Moreover, the existence of a vibrational relaxation process via $^4\Sigma_u^+$ has also been suggested through a matrix experiment [56].

In this study, we aim to experimentally clarify the electronic structure and relaxation processes of C_2^- by a time-resolved high-resolution laser spectroscopy, and study the rovibrational spectra of C_2^- and its time evolution. Laser spectroscopy was performed for C_2^- stored in the recently developed RICE (RIKEN Cryogenic Electrostatic ring), a cryogenic ion storage ring at RIKEN [57].

1.0.3 Structure of this thesis

Section 1.2 outlines the general theory of diatomic molecules including some examples of carbon dimer and its anion. Section 1.3 introduces previous spectroscopic and theoretical studies of carbon dimer anion. Chapter 2 describes experimental techniques for spectroscopy of highly excited states. In Chapter 3, we will discuss the origin of the autodetachment processes from highly excited states, as well as the acquisition and analysis of photodetachment spectra. Acquired by photodetachment spectra for each storage time, we observe the relaxation process of C_2^- at high temperatures. The decay lifetime of each transition peak is thereby obtained. Chapter 4 describes conclusion and outlook for study of highly electronic excited state.

As an extension of this work, we plan to conduct a merged-beam experiment in an ion storage ring for low-energy reaction studies using molecular ion beams with

well-defined internal states. The appendix describes the development of a neutral beam for this purpose.

1.1 Spectroscopy of diatomic molecules

This section outlines the general theory of diatomic molecules. In the beginning, the electronic structure, its parity, and selection rules are outlined. As an example of allowed transition spectra between low-lying electronic states, the electronic transitions of neutral carbon dimer are shown. After that, rovibrational structures are outlined. Nonsinglet–Nonsinglet rotational transitions present a complex picture. Carbon dimer anion, the subject of this paper, has doublet and quartet electronic states near the ground state, which will be outlined in some detail.

1.1.1 Electronic structure and selection rule

1.1.1.1 Angular momenta and term symbols

Under the Born-Oppenheimer approximation, which regards the motion of the nucleus as very slow relative to that of the electron, nuclear motion and electron motion can be separated. Then the Hamiltonian of the electronic part of diatomic molecule A–B is written as

$$\hat{H}_{\text{el}} = -\frac{\hbar^2}{2m_e} \sum_i \nabla_i^2 - \sum_i \frac{Z_A e^2}{4\pi\epsilon_0 r_{Ai}} - \sum_i \frac{Z_B e^2}{4\pi\epsilon_0 r_{Bi}} + \frac{Z_A Z_B e^2}{4\pi\epsilon_0 r_{AB}} + \sum_i \sum_{j>i} \frac{e^2}{4\pi\epsilon_0 r_{ij}} \quad (1.1)$$

where m_e is the mass of an electron, Z_A and Z_B are the atomic numbers of A and B, r_{Ai} and r_{Bi} are the distances between electrons and each nucleus, r_{AB} is the distance of the nuclei A and B, r_{ij} are the distances between the electrons, e is the elementary charge and ϵ_0 is the electric constant. The solution of the electronic Schrödinger equation $\hat{H}_{\text{el}}\psi_{\text{el}} = E_{\text{el}}\psi_{\text{el}}$ is the Slater determinant of molecular orbitals ϕ_i such that

$$\psi_{\text{el}}(x_1, \dots, x_N) = \frac{1}{\sqrt{N!}} \begin{vmatrix} \phi_1(x_1) & \cdots & \phi_1(x_N) \\ \vdots & \ddots & \vdots \\ \phi_N(x_1) & \cdots & \phi_N(x_N) \end{vmatrix} \quad (1.2)$$

and each molecular orbital is a linear combination of the atomic orbitals ϕ_j^A and ϕ_j^B such that

$$\phi_i = \sum_j (C_{iA_j} \phi_j^A + C_{iB_j} \phi_j^B). \quad (1.3)$$

Fig. 1.1 shows the typical diatomic molecular orbital diagram. The symmetry of the molecule is $D_{\infty h}$ for homonuclear and $C_{\infty v}$ for heteronuclear. The irreducible representation of $D_{\infty h}$ is $\sigma, \pi, \delta, \dots$ with the subscripts of g (gerade) and u (ungerade). The superscript asterisk * indicates that its molecular orbital is an antibonding orbital, which means its energy level is higher than the original atomic orbital. The main configuration of the ground state of the neutral carbon dimer represents

$$1\sigma_g^2 1\sigma_u^2 2\sigma_g^2 2\sigma_u^2 1\pi_u^4.$$

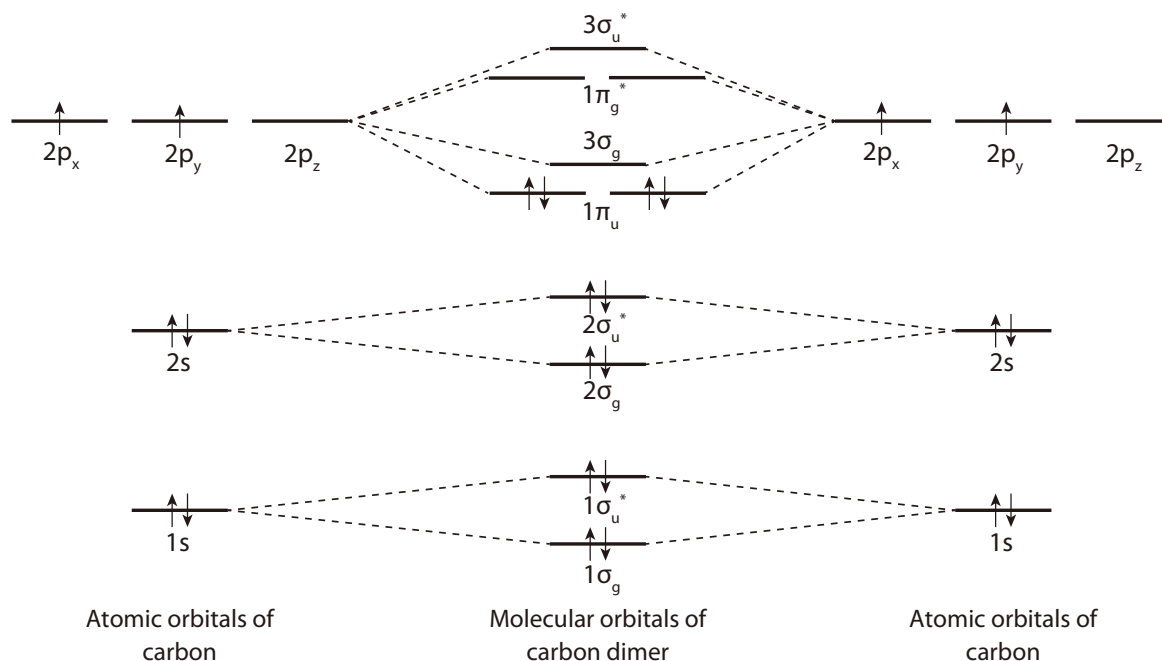


Figure 1.1: The molecular orbital diagram of carbon dimer C_2 . For the diagram of the diatomic molecules except Li_2 , Be_2 , B_2 , C_2 , N_2 , $1\pi_u$ and $3\sigma_g$ are reversed.

The bond order represents the number of bonds between two atoms in a given configuration. It derived as

$$(\text{bond order}) = \frac{(\text{number of bonding electrons}) - (\text{number of antibonding electrons})}{2} \quad (1.4)$$

in molecular orbital theory. For example, the bond order of the main configuration of the ground state of C_2 is 2.

Notice that this definition of bond order is based on molecular orbital theory, and other theories may derive different bond orders. For example, C_2 has a bond order of 4 in valence bond theory [58] and natural orbital functional theory [59]. The difference in the bond order of C_2 between each theories is still under the discussion [60–64].

The term symbol for a diatomic molecule is written as $^{2S+1}\Lambda_{\Omega}$. The meaning of each number is the same as that of the atomic term symbols: Λ is the total orbital angular momentum, $2S + 1$ is the spin multiplicity, and Ω is the total angular momentum. Λ is a capital letter for multi-electron molecular labels. Lowercase λ is for one-electron orbital labels.

In order to derive the selection rule, it is essential to understand the coupling of angular momentum. For diatomic molecules, in addition to orbital and spin as well as an atom, nuclear rotation must also be considered. Then the total angular momentum \hat{J} can be expressed as

$$\hat{J} = \hat{L} + \hat{S} + \hat{R} \quad (1.5)$$

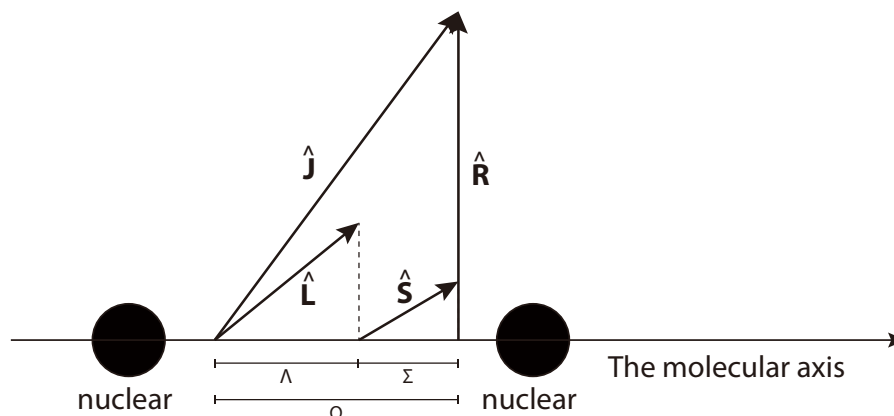


Figure 1.2: An example of the coupling of angular momenta in a diatomic molecule employing the molecular axis as a quantization axis.

where $\hat{\mathbf{L}}$ is orbital angular momentum, $\hat{\mathbf{S}}$ is spin angular momentum, and $\hat{\mathbf{R}}$ is nuclear rotation angular momentum. The projection of the total angular momentum $\hat{\mathbf{J}}$ onto the molecular axis is represented as $\Omega\hbar = \Lambda\hbar + \Sigma\hbar$ where $\Lambda\hbar$ is the projection of the orbital angular momentum $\hat{\mathbf{L}}$ and $\Sigma\hbar$ is the projection of the spin angular momentum $\hat{\mathbf{S}}$. Note that the nuclear rotation angular momentum $\hat{\mathbf{R}}$ is orthogonal to the molecular axis and does not affect the projection, as shown in Fig. 1.2.

The ground electronic states are labeled with a capital X (e.g. $\text{C}_2 X^1\Sigma_g^+$). The other electronic states are labeled with Latin letters, beginning with A , in order of increasing energy level. Electronic states with spin multiplicity equivalent to the ground state are capitalized (e.g. $\text{C}_2 A^1\Pi_u$); all other electronic states are lowercased (e.g. $\text{C}_2 a^3\Pi_u$).

Hund's rule generally holds for molecules. For instance, the ground electronic state of the oxygen dimer is $X^3\Sigma_g^-$, and the singlet oxygens $a^1\Delta_g$ and $b^1\Sigma_g^+$ are excited states. For carbon dimer, $X^1\Sigma_g^+$, that each subshell is closed, is the electronic ground state.

1.1.1.2 Parity related with the electronic structure

In diatomic molecules, there are four types of notable parities: total parity (+/-), gerade/ungerade parity (g/u), rotationless parity (e/f), and symmetric/antisymmetric parity (s/a). Rotationless parity (e/f) is related to rovibrational parts and will be described in the corresponding sections. Since symmetric/antisymmetric parity (s/a) relates to nuclear spin, it is omitted in this thesis. Note that the nucleus of carbon is a boson because the nuclear spin is zero. Then the nuclear spin wave function ψ_{nuc} is symmetry, and it has to be combined with the wave function of the other parts (electron spin, orbital, vibrational, and rotational parts) ψ which is symmetry. For $^1\Sigma_g^+$, the rotationless parity of each rotational level, which will be described, is e and the

total parity is alternately, such that $J = 0 (+), 1 (-), 2 (+), \dots$. The ψ of C_2 is symmetry and then the $C_2 X^1\Sigma_g^+$ has only odd rotational quantum number $J = 0, 2, 4, \dots$

■ **Total parity (+/-)** Now we suppose the eigenfunction ψ of the Hamiltonian for the entire molecule, taking into account electronic, vibrational, and rotational parts. Let \hat{E}^* be the symmetry operator, which inverts all the coordinates of the nuclei and electrons (X_i, Y_i, Z_i) in the laboratory frame that the origin which sets to the center of mass, that is,

$$\hat{E}^*\psi(X_i, Y_i, Z_i) = \psi(-X_i, -Y_i, -Z_i) \quad (1.6)$$

and we can say

$$\hat{E}^*\psi(X_i, Y_i, Z_i) = \pm\psi(X_i, Y_i, Z_i) \quad (1.7)$$

since $\hat{E}^*\hat{E}^*\psi = \psi$.

The wave function is divided into each part and denoted $\psi = \psi_{\text{el}}\psi_{\text{vib}}\psi_{\text{rot}}$. The vibrational and rotational structures will be discussed in more detail later. Since the vibrational wavefunction ψ_{vib} depends only on the internuclear separation r , \hat{E}^* does not change the wavefunction ψ_{vib} , i.e. $\hat{E}^*\psi_{\text{vib}}(r) = \psi_{\text{vib}}(r)$. Therefore, there is no effect of the vibrational part on parity. The rotational wavefunction ψ_{rot} depends on θ and ϕ , which are transformed by E into $\pi - \theta$ and $\pi + \phi$, i.e. $\hat{E}^*\psi_{\text{rot}}(\theta, \phi) = \psi_{\text{rot}}(\pi - \theta, \pi + \phi)$. ψ_{rot} is generally represented as $|\Omega, J, M\rangle$. According to Hougen [65], $\hat{E}^*|\Omega, J, M\rangle = (-1)^{J-\Omega} |-\Omega, J, M\rangle$ is hold where M is the secondary total angular momentum quantum number.

It is difficult to derive the results of the transformation of the electronic wavefunction by \hat{E}^* in the laboratory system. It is known that \hat{E}^* in the laboratory system is $\hat{\sigma}_v$ in the molecular frame [65–67]. Thus, we can say $\hat{\sigma}_v |S, \Sigma\rangle = (-1)^{S-\Sigma} |S, -\Sigma\rangle$ for the spin part and $\hat{\sigma}_v |\Lambda\rangle = \pm(-1)^\Lambda |-\Lambda\rangle$ for the orbital part. When $\Lambda = 0$, i.e., in Σ state, $\hat{\sigma}_v |\Lambda = 0\rangle = \pm(-1)^\Lambda |\Lambda = 0\rangle$ is hold for the orbital part. This parity is written in the upper right corner of the term symbol such that Σ^+ or Σ^- . When $\Lambda > 0$, the orbital is twofold degenerated. Therefore there are no cases for the wavefunction of the orbital part to have only + parity or - parity. Then it is only in Σ that the total parity of the orbital part is written in the upper left corner of the term symbol.

In summary,

$$\hat{E}^*\psi = \hat{\sigma}_v (|n, \Lambda, S, \Sigma\rangle |v\rangle |\Omega, J, M\rangle) \quad (1.8)$$

$$= (-1)^{J-2\Sigma+S+\sigma} |n, -\Lambda, S, -\Sigma\rangle |v\rangle |-\Omega, J, M\rangle \quad (1.9)$$

is hold where $\sigma = 1$ for Σ^- state and $\sigma = 0$ for the other states. The selection rule for the total parity is that the transition moment integral $\langle \psi_f | \boldsymbol{\mu} | \psi_i \rangle$ should be positive. Since the parity of the transition moment operator is negative, i.e. $\hat{E}^*\boldsymbol{\mu} = -\boldsymbol{\mu}$, one-photon electron dipole transitions occur only when the total parity changes ($+ \leftrightarrow -$).

■ **Gerade/ungerade parity (g/u)** The symmetry of the molecule is $D_{\infty h}$ for homonuclear and $C_{\infty v}$ for heteronuclear. The gerade/ungerade parity is only concerned with

a homonuclear molecule. Consider the inversion operator \hat{i} with respect to $D_{\infty h}$, which inverts the all coordinate of the nuclei and electrons (x_i, y_i, z_i) in the molecular frame. Note that \hat{E}^* is an invert operator in the laboratory frame but not in the molecular frame.

Operator \hat{i} only reverses the displacement of the electrons and does not affect the nucleus. The vibration, rotation, and electron spin parts of the wavefunction are also not affected by \hat{i} . Therefore,

$$\hat{i}\psi_{\text{el}}(x_i, y_i, z_i) = \pm\psi_{\text{el}}(x_i, y_i, z_i), \quad (1.10)$$

in other words, $\hat{i}|\Lambda\rangle = \pm|\Lambda\rangle$.

When a wavefunction has a sign of + with respect to \hat{i} , its parity is called gerade parity, and when it has a sign of -, it is called ungerade parity. This parity is written in the lower right corner of the term symbol such that $^1\Sigma_g^+$ or $^1\Delta_g$. Since $\hat{i}\boldsymbol{\mu} = -\boldsymbol{\mu}$, one-photon electron dipole transitions occur only when the total parity changes ($g \leftrightarrow u$).

1.1.1.3 Selection rule

The six selection rules for electronic states are as follows:

1. $\Delta\Lambda = 0, \pm 1$
2. $\Delta S = 0$
3. $\Delta\Sigma = 0$
4. $\Delta\Omega = 0, \pm 1$
5. conservation of the total parity (+/-)
6. conservation of the gerade/ungerade parity (g/u)

For example, $^1\Sigma-^3\Sigma$ is allowed in rule 1 but not in rule 2, then it is the forbidden transition. Note that for molecules composed of heavy atoms, Λ and S are no longer good quantum numbers due to the increased spin-orbit interaction and then some selection rules no longer hold. For example, $\Delta S \neq 0$ transitions are also optically allowable for heavy atoms. Since each electronic transition on the photosensitive plate appears as a bundle of many lines of rovibrational transitions, electronic transitions are called a band system from the early days of spectroscopy.

Fig. 1.3 shows the famous allowable transitions on neutral carbon dimer. Swan [69] firstly reported the green color light emission in the flame, and this knowledge has been used to analyze the composition of comets [41]. The transition spectrum he discovered ($d^3\Pi_g-a^3\Pi_u$) is called the Swan band. For 90 years until Phillips' discovery of the $A^1\Pi_u-X^1\Sigma_g^+$ transition [70], the existence of states lower than $a^3\Pi_u$ state was not known. Among the many known transitions, laser cooling using Swan, Duck, Phillips, and Ballik-Ramsay has recently been proposed [71].

1.1.2 Vibrational structure

The energy level of the vibrational transition in the spectrum, not accounting for rotational structure, is expressed by the energy difference between the initial and

final vibrational state, such as

$$\begin{aligned} \tilde{\nu}_{v'v''} = \Delta T_e & \\ & + (\omega'_e(v' + 1/2) - \omega'_e x'_e(v' + 1/2)^2 + \omega'_e y'_e(v' + 1/2)^3 + \omega'_e z'_e(v' + 1/2)^3 + \dots) \\ & - (\omega''_e(v'' + 1/2) - \omega''_e x''_e(v'' + 1/2)^2 + \omega''_e y''_e(v'' + 1/2)^3 + \omega''_e z''_e(v'' + 1/2)^3 + \dots) \end{aligned} \quad (1.11)$$

where ΔT_e is the difference of each term energy, which means the potential minimum of the electronic states, ω'_e , x'_e , and so on are the coefficients for expansion of energy eigenvalues in terms of vibrational quantum numbers. As an example of expansion coefficients, we introduce an example of the Morse potential [72]

$$V(r) = D \left(1 - e^{-a(r-r_e)}\right)^2. \quad (1.12)$$

The vibrational energy level of the Morse potential can be expanded such as

$$E(v) = \omega_e(v + 1/2) - \omega_e x_e(v + 1/2)^2 \quad (1.13)$$

in the unit of cm^{-1} where

$$\omega_e = a \left(\frac{Dh \times 10^2}{2\pi^2 c \mu} \right)^{1/2}, \quad (1.14)$$

$$\omega_e x_e = \frac{ha \times 10^2}{8\pi^2 \mu c}. \quad (1.15)$$

Note that the Morse potential takes into account terms up to the second order of the vibrational quantum number. In other words, the potential energy curve can be derived from the vibration spectrum up to the second order of the vibrational quantum number.

The set of vibrational transitions with the same difference Δv in vibrational quantum numbers, such as $v' = 0 - v'' = 0$ (called 0-0), 1-1, 2-2, ... is called a sequence. For example, a set of the vibrational transition with 0-1, 1-2, 2-3, ... is called a $\Delta v = -1$ sequence. Also, the set of vibrational transitions 1-0, 2-1, 3-2, ... is said to be a $\Delta v = 1$ sequence. The set of transitions with the same lower state is called lower state progression, and the set of transitions with the same upper state is called upper state progression. For example, 0-1, 1-1, 2-1, ... is a lower state progression. This progression is useful to examine the energy levels of the other state if one state is reliable.

The peak intensity of the vibrational transition is determined by the intrinsic strength of the electronic transition as well as the vibrational level population and the Frank-Condon factor $q_{v'v''} = |\langle v' | v'' \rangle|^2$. The intensity ratio of two vibrational transitions with the same initial vibrational level is determined by the ratio of the Frank-Condon factors. For example, assuming a Morse potential and the transition between electronic states where r_e , ω_e and x_e are almost the same, the $\Delta v = 0$ sequence has the strongest intensity since the $\Delta v = 0$ sequence has the largest overlap

of the wavefunctions of the initial and final states. If the Franck-Condon factor tends to be large for sequences with large Δv , the upper vibrational level is close to the dissociation limit, and the molecule could be directly dissociated by the vibrational transition.

The vibrational transition is also affected by the rotational quantum number. For large J , the effective potential energy curve changes significantly compared to when $J = 0$. For example, the silver dimer ion Ag_2^- is electronically detached from the high vibration state when the rotational angular momentum $L = 0$ (specifically, for instance, the transition $\text{Ag}_2^- X^2\Sigma_u^+ v' = 110 - \text{Ag}_2 X^1\Sigma_g^+ v'' = 7$), because the dissociation limit of Ag_2^- is above the detachment threshold. On the other hand, when $L = 300$, there are not only the detachment threshold above the dissociation limit but also some vibrational states (for instance, $\text{Ag}_2^- X^2\Sigma_u^+ v'' \geq 88$) above the dissociation limit, i.e., a quasibound state, which dissociates in a finite time. This dissociation is called tunneling fragmentation. This phenomenon has been observed experimentally using the cryogenic ion storage ring DESIREE [73].

1.1.3 Rotational structure

1.1.3.1 Rotational energy and spectra

Assuming a diatomic molecule is a rigid rotor, its Hamiltonian can be written as

$$\hat{H} = \frac{\hat{J}^2}{2I}. \quad (1.16)$$

Solving the Schrödinger equation, we obtain that the eigenvalue of the Hamiltonian $F(J)$ in the unit of a joule is

$$F(J) = BJ(J + 1) \quad (1.17)$$

where $B = \frac{\hbar^2}{2I}$ and I is the moment of inertia, that is, $I = \mu r$ where μ is the reduced mass and r is the internuclear distance. The rotational wave function of a linear molecule can be written as

$$\psi_{JM} = Y_J^M(\theta, \phi) = (-1)^M \sqrt{\frac{(2J+1)(J-M)!}{4\pi(J+M)!}} P_J^M(\cos \theta) \exp(iM\phi) \quad (1.18)$$

$$= N_{JM} P_J^M(\cos \theta) \exp(iM\phi) \quad (1.19)$$

where P_J^M is associated Legendre polynomials and N_{JM} is defined as $N_{JM} = (-1)^M \sqrt{\frac{(2J+1)(J-M)!}{4\pi(J+M)!}}$.

The transition dipole moment is described as

$$\mathbf{M} = \int \psi_{J'M'} \boldsymbol{\mu} \psi_{JM} d\tau \quad (1.20)$$

where $\boldsymbol{\mu}$ is the dipole moment in the molecular frame

$$\boldsymbol{\mu} = \mu_0(\sin \theta \cos \phi \hat{\mathbf{e}}_1 + \sin \theta \sin \phi \hat{\mathbf{e}}_2 + \cos \theta \hat{\mathbf{e}}_3). \quad (1.21)$$

Then

$$\begin{aligned}
\mathbf{M} = \frac{\mu_0}{2\pi} & \left(\hat{e}_1 \int_0^{2\pi} \int_0^\pi N_{J'M'} P_{J'}^{M'}(\cos \theta) \exp(iM'\phi) \sin \theta \cos \phi \right. \\
& N_{JM} P_J^M(\cos \theta) \exp(iM\phi) \sin \theta d\theta d\phi \\
& + \hat{e}_2 \int_0^{2\pi} \int_0^\pi N_{J'M'} P_{J'}^{M'}(\cos \theta) \exp(iM'\phi) \sin \theta \sin \phi \\
& N_{JM} P_J^M(\cos \theta) \exp(iM\phi) \sin \theta d\theta d\phi \\
& \left. + \hat{e}_3 \int_0^{2\pi} \int_0^\pi N_{J'M'} P_{J'}^{M'}(\cos \theta) \exp(iM'\phi) \cos \theta \right. \\
& \left. N_{JM} P_J^M(\cos \theta) \exp(iM\phi) \sin \theta d\theta d\phi \right). \quad (1.22)
\end{aligned}$$

From the relationship of the associated Legendre polynomials

$$(2J + 1) \cos \theta P_J^M(\cos \theta) = (J + M) P_{J-1}^M(\cos \theta) + (J - M + 1) P_{J+1}^M(\cos \theta), \quad (1.23)$$

we find selection rules

$$\Delta J = \pm 1, \quad (1.24)$$

$$\Delta M = 0, \pm 1. \quad (1.25)$$

The series of rotational transition lines with $\Delta J = -1$ in the spectrum is called P-branch, and one with $\Delta J = 1$ is called R-branch. Since the frequency of the transition line is

$$\begin{aligned}
\nu_{J+1,J} &= F(J + 1) - F(J) \\
&= B(J + 1)(J + 2) - BJ(J + 1) \\
&= 2B(J + 1), \quad (1.26)
\end{aligned}$$

the transition lines are equally spaced. Note that the transitions in which the non-rotational angular momentum (i.e., orbital, spin, vibrational angular momenta) changes can result in the rotational quantum number change other than ± 1 .

The homonuclear diatomic molecule has no permanent dipole moment, so there are no rotational allowed transitions.

We have assumed that the molecule is a rigid rotor, but we must consider that the actual molecule is affected by the centrifugal forces of its constituent atoms. The rotational energy is expanded to a higher order, and we describe it as

$$F(J) = BJ(J + 1) - D(J(J + 1))^2 + H(J(J + 1))^3 + L(J(J + 1))^4 + \dots \quad (1.27)$$

where D is called a centrifugal distortion constant. As J increases, the effect of higher order terms on rotational energy increases. Then the frequency of the transition line

can be described as

$$\begin{aligned}
 \nu_{J+1,J} &= F(J+1) - F(J) \\
 &= (B(J+1)(J+2) - D((J+1)(J+2))^2) - (BJ(J+1) - D(J(J+1))^2) \\
 &= 2B(J+1) - 4D(J+1)^3.
 \end{aligned} \tag{1.28}$$

The rotational constant B and higher order constants D, H, \dots are also affected by the vibrational quantum number v . Expanding B and D with respect to v , we can express them with v as

$$B_v = B_e - \alpha_e(v + 1/2) + \gamma_e(v + 1/2)^2 + \dots \tag{1.29}$$

$$D_v = D_e + \beta_e(v + 1/2) + \dots \tag{1.30}$$

The eigenvalues for Morse potential (eq. 1.12) with the centrifugal term in the unit of cm^{-1} is derived as

$$E = \omega_e(v + 1/2) - \omega_e x_e(v + 1/2)^2 + B_e J(J + 1) - D_e(J(J + 1))^2 - \alpha_e(v + 1/2)J(J + 1) \tag{1.31}$$

where

$$\omega_e = \beta \left(\frac{Dh \times 10^2}{2\pi^2 c \mu} \right)^{1/2}, \tag{1.32}$$

$$\omega_e x_e = \frac{h\beta \times 10^2}{8\pi^2 \mu c}, \tag{1.33}$$

$$B_e = \frac{h \times 10^{-2}}{8\pi^2 \mu r_e^2 c}, \tag{1.34}$$

$$D_e = \frac{4B_e^3}{\omega_e^2} \quad (\text{called Kratzer relationship}), \tag{1.35}$$

$$\alpha_e = \frac{6(\omega_e x_e B_e^3)^{1/2}}{\omega_e} - \frac{6B_e^2}{\omega_e} \quad (\text{called Pekeris relationship}). \tag{1.36}$$

Note that D in those equations is the constant of the Morse potential but not the centrifugal distortion constant.

The Taylor expansion of molecular potential

$$V(\xi) = hca_0 \xi^2 (1 + a_1 \xi + a_2 \xi^2 + a_3 \xi^3 + \dots) \tag{1.37}$$

where

$$\xi = \frac{r - r_e}{r_e} \tag{1.38}$$

and r_e is the equilibrium nuclear separation is called Dunham potential, which is a more generalized form than Morse potential [74]. The Schrödinger equation with

centrifugal potential is

$$\frac{d^2\psi}{d\xi^2} + \frac{8\pi^2\mu r_e^2}{h^2} \left(E - V(\xi) - \frac{\hbar^2 J(J+1)}{8\pi^2\mu r_e^2(1+\xi)^2} \right) \psi = 0. \quad (1.39)$$

Using WKB (Wentzel-Kramers-Brillouin) approximation, which is an approximation based on first-order semiclassical quantization conditions, Dunham got the action integral:

$$I = (hc)^{-1/2} \oint (E - V)^{1/2} d\xi = 2\pi^{1/2}(v + 1/2) \quad (1.40)$$

with the integral path of the $r_- \rightarrow r_+ \rightarrow r_-$ where r_- is the inner turning point for $V(r)$ at the energy E and r_+ is the outer one. He also got the eigenvalue

$$E_{vJ} = \sum_{jk} Y_{jk} (v + 1/2)^j (J(J+1))^k. \quad (1.41)$$

Compared to the expansion of vibrational energy

$$G(v) = \omega_e(v + 1/2) - \omega_e x_e(v + 1/2)^2 + \omega_e y_e(v + 1/2)^3 + \omega_e z_e(v + 1/2)^3 + \dots \quad (1.42)$$

and rotational energy (eqs. 1.27, 1.29, 1.30), Y_{jk} , called Dunham parameter can be expressed by some spectroscopic constants such that

$$Y_{10} \sim \omega_e, \quad (1.43)$$

$$Y_{20} \sim -\omega_e x_e, \quad (1.44)$$

$$Y_{30} \sim \omega_e y_e, \quad (1.45)$$

$$Y_{01} \sim B_e, \quad (1.46)$$

$$Y_{11} \sim -\alpha_e, \quad (1.47)$$

$$Y_{21} \sim \gamma_e, \quad (1.48)$$

$$Y_{02} \sim -D_e, \quad (1.49)$$

$$Y_{12} \sim -\beta_e, \quad (1.50)$$

$$Y_{40} \sim \omega_e z_e, \quad (1.51)$$

$$Y_{03} \sim H_e. \quad (1.52)$$

Since eqs. 1.32–1.36, we obtain

$$\omega_e \propto \mu^{1/2}, \quad (1.53)$$

$$B_e \propto \mu^{-1}, \quad (1.54)$$

$$\omega_e x_e \propto \mu^{-1}, \quad (1.55)$$

$$D_e \propto \mu^{-2}, \quad (1.56)$$

$$\alpha_e \propto \mu^{-3/2}. \quad (1.57)$$

Therefore,

$$Y_{jk} \propto \mu^{-(j+2k)/2} \quad (1.58)$$

is obtained. This proportionality holds for general j, k . The above discussion is valid only when the Born-Oppenheimer and WKB approximations are valid. Otherwise, a small correction term must be added to eq. 1.41.

As described above, the Dunham potential can be used to determine the potential from the spectral constants. However, today, when deriving potentials from spectral constants, it is common to use the RKR (Rydberg-Klein-Rees) potential [75–77], and the numerical software LEVEL [78] is regularly used for this purpose. The RKR potential is similar to the Dunham potential in that the WKB approximation is assumed to be well established; in other words, eq. 1.40 allows.

The RKR method determines the potential energy curve $V(r)$ by finding r_- and r_+ using spectral constants. From action integral eq. 1.40, the Klein integrals

$$r_+(v) - r_-(v) = \sqrt{2\hbar/\mu} \int_{v_{\min}^v} \frac{dv'}{\sqrt{G(v) - G(v')}} \quad (1.59)$$

$$\frac{1}{r_-(v)} - \frac{1}{r_+(v)} = \sqrt{8\mu/\hbar^2} \int_{v_{\min}^v} \frac{B_{v'} dv'}{\sqrt{G(v) - G(v')}} \quad (1.60)$$

were derived (see. Miller [79]). This equation is semiclassical, and v is a continuous value. v_{\min} is $-1/2$ and integrates over the value of v we wish to find. This allows us to determine the energy level E_{vJ} and its wave function $\psi_{vJ}(r)$. From the obtained wave functions, we can obtain rotational constants, centrifugal distortion constants, and Franck-Condon factors. LEVEL [78] also performs these calculations.

1.1.3.2 Selection rules

In the case of rotational transitions with electronic transitions, the discussion on angular momentum is complicated. Depending on the spin multiplicity of the initial and final states, we have different selection rules.

■ For singlet–singlet transitions The selection rule for Singlet-Singlet transitions is simple and is as follows:

1. $\Delta\Lambda = 0$
 - (a) $\Lambda'' = \Lambda' = 0$
 - (b) $\Lambda'' = \Lambda' \neq 0$
2. $\Delta\Lambda = \pm 1$

The only cases that apply to 1(a) are $^1\Sigma^+ - ^1\Sigma^+$ and $^1\Sigma^- - ^1\Sigma^-$. Since $\Delta J = \pm 1$, They have only P and R branches. Their transition dipole moments are along the z-axis. The examples of case 1(b) are $^1\Pi - ^1\Pi$ and $^1\Delta - ^1\Delta$, etc. They have P and R branches ($\Delta J = \pm 1$) and weak Q branch ($\Delta J = 0$). The examples of case 2 are $^1\Pi - ^1\Sigma^+$ and $^1\Delta - ^1\Pi$, etc. They have P and R branches ($\Delta J = \pm 1$) and strong Q branch ($\Delta J = 0$). Their transition dipole moments are perpendicular to the molecular axis.

The power emitted in the transition from $|n'v'J'\rangle$ to $|n''v''J''\rangle$ is

$$P_{J'J''} = \frac{64\pi^4}{(4\pi\epsilon_0)3c^3} \frac{N_{J'}}{(2J'+1)} \nu_{J'J''}^4 q_{v'v''} |\mathbf{R}_e|^2 S_{J''}^{\Delta J} \quad (1.61)$$

where $P_{J'J''}$ is the power per unit volume (Wm^{-3}), $N_{J'}$ the number density of J' level (m^{-3}), $\nu_{J'J''}$ is the frequency of emitted radiation (Hz), $q_{v'v''}$ is the Franck-Condon factor, \mathbf{R}_e is the the electronic transition dipole moment ($\text{C} \cdot \text{m}$) and $S_{J''}^{\Delta J}$ is the rotational line strength [65, 80, 81]. $S_{J''}^{\Delta J}$ is called *Hönl–London factor* and is known to be as shown in Table 1.1. The wavenumbers of the spectrum for the P, R, and Q branches are

$$\tilde{\nu}_P = \tilde{\nu}_0 - (B' + B'')J'' + (B' - B'')J''^2, \quad (1.62)$$

$$\tilde{\nu}_R = \tilde{\nu}_0 + 2B' + (3B' - B'')J'' + (B' - B'')J''^2 \quad (1.63)$$

$$= \tilde{\nu}_0 + (B' + B'')(J'' + 1) + (B' - B'')(J'' + 1)^2, \quad (1.64)$$

$$\tilde{\nu}_Q = \tilde{\nu}_0 + (B' - B'')J''(J'' + 1), \quad (1.65)$$

where B' and B'' are rotational constants. Let m be as the following:

$$m = \begin{cases} -J'' & \text{for P branch} \\ J'' + 1 & \text{for R branch} \end{cases} \quad (1.66)$$

then $\tilde{\nu}_P$ and $\tilde{\nu}_R$ are described as

$$\tilde{\nu}_{P,R} = \tilde{\nu}_0 + (B' + B'')m + (B' - B'')m^2. \quad (1.67)$$

The m plot of $\tilde{\nu}_{P,R}$ is called *Fortrat parabola* and The $|m|$ plot of $\tilde{\nu}_{P,R}$ is called *Fortrat diagram*. Note that the head of rotational band $\tilde{\nu}_H$ is not the origin $\tilde{\nu}_0$ but the extremum of Fortrat parabola. Since

$$\frac{d\tilde{\nu}_{P,R}}{dm} = (B' + B'') + 2m(B' - B'') = 0 \quad (1.68)$$

$\tilde{\nu}_{P,R}$ reaches an extreme at

$$m_H = -\frac{(B' + B'')}{2(B' - B'')}. \quad (1.69)$$

Then the head-origin separation is described as

$$\tilde{\nu}_H - \tilde{\nu}_0 = -\frac{(B' + B'')^2}{4(B' - B'')}. \quad (1.70)$$

As an example of a Fortrat diagram of a Singlet–Singlet transition, the $A^1\Pi_u \ v' = 3 - X^1\Sigma_g \ v'' = 1$ transition of C_2 (Phillips band) is shown in Fig. 1.4.

Table1.1: Hönl–London factor referenced to Herzberg [82] and Hansson [83]. The superscripts P , Q , and R in S indicate $\Delta J = -1, 0, 1$, respectively.

for $\Delta\Lambda = 0$

$$S_J^R = \frac{(J''+1+\Lambda'')(J''+1-\Lambda'')} {J''+1} = \frac{(J'+\Lambda')(J'-\Lambda')}{J'}$$

$$S_J^Q = \frac{(2J''+1)\Lambda''^2}{J''(J''+1)} = \frac{(2J'+1)\Lambda'^2}{J'(J'+1)}$$

$$S_J^P = \frac{(J''+\Lambda'')(J''-\Lambda'')} {J''} = \frac{(J'+1+\Lambda')(J'+1-\Lambda')}{J'+1}$$

for $\Delta\Lambda = +1$

$$S_J^R = \frac{(J''+2+\Lambda'')(J''+1+\Lambda'')} {2(J''+1)} = \frac{(J'+\Lambda')(J'-1+\Lambda')}{2J'}$$

$$S_J^Q = \frac{(J''+1+\Lambda'')(J''-\Lambda'')(2J''+1)} {2J''(J''+1)} = \frac{(J'+\Lambda')(J'+1-\Lambda')(2J'+1)} {2J'(J'+1)}$$

$$S_J^P = \frac{(J''-1-\Lambda'')(J''-\Lambda'')} {2J''} = \frac{(J'+1-\Lambda')(J'+2-\Lambda')}{2(J'+1)}$$

for $\Delta\Lambda = -1$

$$S_J^R = \frac{(J''+2-\Lambda'')(J''+1-\Lambda'')} {2(J''+1)} = \frac{(J'-\Lambda')(J'-1+\Lambda')}{2J'}$$

$$S_J^Q = \frac{(J''+1-\Lambda'')(J''+\Lambda'')(2J''+1)} {2J''(J''+1)} = \frac{(J'-\Lambda')(J'+1+\Lambda')(2J'+1)} {2J'(J'+1)}$$

$$S_J^P = \frac{(J''-1+\Lambda'')(J''+\Lambda'')} {2J''} = \frac{(J'+1+\Lambda')(J'+2+\Lambda')}{2(J'+1)}$$

■ For nonsinglet–nonsinglet transitions For nonsinglet–nonsinglet transitions, spin-orbit interaction must be taken into account. The Hamiltonian is

$$\hat{H} = \hat{H}_{\text{el}} + \hat{H}_{\text{vib}} + \hat{H}_{\text{rot}} + \hat{H}_{\text{so}} \quad (1.71)$$

where $\hat{H}_{\text{so}} = A\hat{L} \cdot \hat{S}$ is a part of Hamiltonian regarding spin-orbit interaction and the electronic and vibrational portions are assumed to be constant i.e. $\langle \hat{H}_{\text{el}} + \hat{H}_{\text{vib}} \rangle = E_{\text{ev}}$

since only the rotational structure will be considered in this section. Here we use the following basis: $|\text{electronic}\rangle |\text{vibrational}\rangle |\text{rotational}\rangle = |n, \Lambda, S, \Sigma\rangle |v\rangle |\Omega, J, M\rangle$. From eq. 1.5

$$\begin{aligned}\hat{H}_{\text{rot}} &= B(\hat{\mathbf{R}})^2 \\ &= B(\hat{\mathbf{J}} - \hat{\mathbf{L}} - \hat{\mathbf{S}})^2 \\ &= B(\hat{J}^2 - \hat{J}_z^2) + B(\hat{S}^2 - \hat{S}_z^2) + B(\hat{L}^2 - \hat{L}_z^2) - B(\hat{J}^+ \hat{L}^- + \hat{J}^- \hat{L}^+) \\ &\quad - B(\hat{J}^+ \hat{S}^- + \hat{J}^- \hat{S}^+) + B(\hat{L}^+ \hat{S}^- + \hat{L}^- \hat{S}^+)\end{aligned}\quad (1.72)$$

$$\begin{aligned}\hat{H}_{\text{so}} &= A\hat{\mathbf{L}} \cdot \hat{\mathbf{S}} \\ &= A\hat{L}_z \hat{S}_z + \frac{A(\hat{L}^+ \hat{S}^- + \hat{L}^- \hat{S}^+)}{2}\end{aligned}\quad (1.73)$$

where $\hat{J}^\pm = \hat{J}_x \pm i\hat{J}_y$, $\hat{L}^\pm = \hat{L}_x \pm i\hat{L}_y$ and $\hat{S}^\pm = \hat{S}_x \pm i\hat{S}_y$ are ladder operators and the all operator is in the molecular frame. Applying the ladder operator \hat{J}^\pm to a rotational state $|\Omega, J, M\rangle$,

$$\hat{J}^+ |\Omega, J, M\rangle = \hbar\sqrt{J(J+1) - \Omega(\Omega-1)} |\Omega-1, J, M\rangle \quad (1.74)$$

$$\hat{J}^- |\Omega, J, M\rangle = \hbar\sqrt{J(J+1) - \Omega(\Omega+1)} |\Omega+1, J, M\rangle, \quad (1.75)$$

and \hat{S}^\pm can also be applied to an electronic state $|\Lambda, S, \Sigma\rangle$ such that

$$\hat{S}^+ |\Lambda, S, \Sigma\rangle = \hbar\sqrt{S(S+1) - \Sigma(\Sigma+1)} |\Lambda, S, \Sigma+1\rangle \quad (1.76)$$

$$\hat{S}^- |\Lambda, S, \Sigma\rangle = \hbar\sqrt{S(S+1) - \Sigma(\Sigma-1)} |\Lambda, S, \Sigma-1\rangle. \quad (1.77)$$

Then the off-diagonal matrix elements of \hat{J}^\pm and \hat{S}^\pm are

$$\langle \Omega \mp 1, J, M | \hat{J}^\pm | \Omega, J, M \rangle = \hbar\sqrt{J(J+1) - \Omega(\Omega \mp 1)} \quad (1.78)$$

$$\langle \Lambda, S, \Sigma \pm 1 | \hat{S}^\pm | \Lambda, S, \Sigma \rangle = \hbar\sqrt{S(S+1) - \Sigma(\Sigma \pm 1)}. \quad (1.79)$$

Since the electron wave function is not an eigenfunction of $\hat{\mathbf{L}}$, \hat{L}^\pm cannot be expressed simply as above, with an expression that increases or decreases the quantum number by one.

As examples of nonsinglet-nonsinglet transitions, we introduce transitions between ${}^2\Sigma^+$ states ($|{}^2\Sigma_{1/2}\rangle, |{}^2\Sigma_{-1/2}\rangle$) and between ${}^2\Pi$ states ($|{}^2\Pi_{3/2}\rangle, |{}^2\Pi_{1/2}\rangle, |{}^2\Pi_{-1/2}\rangle, |{}^2\Pi_{-3/2}\rangle$).

The ${}^2\Sigma^+$ states can be expressed as

$$|{}^2\Sigma_{1/2}\rangle = |n, \Lambda = 0, S = 1/2, \Sigma = 1/2\rangle |v\rangle |\Omega = 1/2, J, M\rangle, \quad (1.80)$$

$$|{}^2\Sigma_{-1/2}\rangle = |n, \Lambda = 0, S = 1/2, \Sigma = -1/2\rangle |v\rangle |\Omega = -1/2, J, M\rangle. \quad (1.81)$$

The representation matrix of \hat{H}_{rot} with $|^2\Sigma_{1/2}\rangle$ and $|^2\Sigma_{-1/2}\rangle$ as the elements of the basis is

$$\begin{pmatrix} \langle ^2\Sigma_{1/2} | \hat{H}_{\text{rot}} | ^2\Sigma_{1/2} \rangle & \langle ^2\Sigma_{1/2} | \hat{H}_{\text{rot}} | ^2\Sigma_{-1/2} \rangle \\ \langle ^2\Sigma_{-1/2} | \hat{H}_{\text{rot}} | ^2\Sigma_{1/2} \rangle & \langle ^2\Sigma_{-1/2} | \hat{H}_{\text{rot}} | ^2\Sigma_{-1/2} \rangle \end{pmatrix} = \begin{pmatrix} B(J+1/2)^2 & -B(J+1/2) \\ -B(J+1/2) & B(J+1/2)^2 \end{pmatrix} \quad (1.82)$$

since

$$\begin{aligned} \langle ^2\Sigma_{1/2} | \hat{H}_{\text{rot}} | ^2\Sigma_{1/2} \rangle &= B(J(J+1) - 1/4) + B(3/4 - 1/4) \\ &= B(J+1/2)^2, \end{aligned} \quad (1.83)$$

$$\begin{aligned} \langle ^2\Sigma_{-1/2} | \hat{H}_{\text{rot}} | ^2\Sigma_{-1/2} \rangle &= B(J(J+1) - 1/4) + B(3/4 - 1/4) \\ &= B(J+1/2)^2, \end{aligned} \quad (1.84)$$

$$\begin{aligned} \langle ^2\Sigma_{1/2} | \hat{H}_{\text{rot}} | ^2\Sigma_{-1/2} \rangle &= B(J(J+1) - \Omega(\Omega-1))^{1/2} (S(S+1) - \Sigma(\Sigma-1))^{1/2} \\ &= -B(J+1/2), \end{aligned} \quad (1.85)$$

$$\begin{aligned} \langle ^2\Sigma_{-1/2} | \hat{H}_{\text{rot}} | ^2\Sigma_{1/2} \rangle &= B(J(J+1) - \Omega(\Omega-1))^{1/2} (S(S+1) - \Sigma(\Sigma-1))^{1/2} \\ &= -B(J+1/2). \end{aligned} \quad (1.86)$$

Note that the \hat{H}_{SO} term does not need to be considered since the transition is between $\Lambda = 0$. Diagonalizing this, it is transformed to

$$\begin{pmatrix} B(J+1/2)^2 - B(J+1/2) & 0 \\ 0 & B(J+1/2)^2 + B(J+1/2) \end{pmatrix} \quad (1.87)$$

with the following elements of the basis :

$$|^2\Sigma^+(e)\rangle = \frac{|^2\Sigma_{1/2}\rangle + |^2\Sigma_{-1/2}\rangle}{\sqrt{2}}, \quad (1.88)$$

$$|^2\Sigma^+(f)\rangle = \frac{|^2\Sigma_{1/2}\rangle - |^2\Sigma_{-1/2}\rangle}{\sqrt{2}}. \quad (1.89)$$

Let a quantum number N be the total angular momentum excluding electrons and spin of nuclei. For the e level, $N = J - 1/2$. Then,

$$B(J+1/2)^2 - B(J+1/2) = B(N+1)^2 - B(N+1) = BN(N+1). \quad (1.90)$$

For the f level, $N = J + 1/2$. Then,

$$B(J+1/2)^2 + B(J+1/2) = BN^2 + BN = BN(N+1). \quad (1.91)$$

This indicates that these two levels are degenerate if spin-orbit interactions are not taken into account. The energy level diagram of $^2\Sigma^+$ is shown in Fig. 1.5. As an example of a Fortrat diagram of $^2\Sigma^+ - ^2\Sigma^+$, the diagram of the $B^2\Sigma_u^+ v' = 0 - X^2\Sigma_g^+ v'' = 0$ transition of C_2^- is shown in Fig. 1.6.

Next, we present another example of a Π - Π transition. The ${}^2\Pi$ states can be expressed as

$$|{}^2\Pi_{3/2}\rangle = |n, \Lambda = 1, S = 1/2, \Sigma = 1/2\rangle |v\rangle |\Omega = 3/2, J, M\rangle, \quad (1.92)$$

$$|{}^2\Pi_{1/2}\rangle = |n, \Lambda = 1, S = 1/2, \Sigma = -1/2\rangle |v\rangle |\Omega = 1/2, J, M\rangle, \quad (1.93)$$

$$|{}^2\Pi_{-1/2}\rangle = |n, \Lambda = -1, S = 1/2, \Sigma = 1/2\rangle |v\rangle |\Omega = -1/2, J, M\rangle, \quad (1.94)$$

$$|{}^2\Pi_{-3/2}\rangle = |n, \Lambda = -1, S = 1/2, \Sigma = -1/2\rangle |v\rangle |\Omega = -3/2, J, M\rangle. \quad (1.95)$$

The representation matrix of $\hat{H}_{\text{rot}} + \hat{H}_{\text{SO}}$ with $|{}^2\Pi_{3/2}\rangle$, $|{}^2\Pi_{1/2}\rangle$, $|{}^2\Pi_{-1/2}\rangle$ and $|{}^2\Pi_{-3/2}\rangle$ as the elements of the basis is

$$\begin{pmatrix} A/2 + B((J+1/2)^2 - 2) & -B\sqrt{(J+1/2)^2 - 1} & 0 & 0 \\ -B\sqrt{(J+1/2)^2 - 1} & -A/2 + B(J+1/2)^2 & 0 & 0 \\ 0 & 0 & -A/2 + B(J+1/2)^2 & -B\sqrt{(J+1/2)^2 - 1} \\ 0 & 0 & -B\sqrt{(J+1/2)^2 - 1} & A/2 + B((J+1/2)^2 - 2) \end{pmatrix} \quad (1.96)$$

since

$$\begin{aligned} \langle {}^2\Pi_{3/2} | \hat{H}_{\text{rot}} + \hat{H}_{\text{SO}} | {}^2\Pi_{3/2} \rangle &= \langle {}^2\Pi_{3/2} | \hat{H}_{\text{rot}} | {}^2\Pi_{3/2} \rangle + \langle {}^2\Pi_{3/2} | \hat{H}_{\text{SO}} | {}^2\Pi_{3/2} \rangle \\ &= B((J+1/2)^2 - 2) + A/2 \end{aligned} \quad (1.97)$$

$$\begin{aligned} \langle {}^2\Pi_{1/2} | \hat{H}_{\text{rot}} + \hat{H}_{\text{SO}} | {}^2\Pi_{1/2} \rangle &= \langle {}^2\Pi_{1/2} | \hat{H}_{\text{rot}} | {}^2\Pi_{1/2} \rangle + \langle {}^2\Pi_{1/2} | \hat{H}_{\text{SO}} | {}^2\Pi_{1/2} \rangle \\ &= -B\sqrt{(J+1/2)^2 - 1} + 0 \end{aligned} \quad (1.98)$$

⋮

It can be diagonalized with the following elements of the basis:

$$|{}^2\Pi_{3/2}(e)\rangle = \frac{|{}^2\Pi_{3/2}\rangle + |{}^2\Pi_{-3/2}\rangle}{\sqrt{2}}, \quad (1.99)$$

$$|{}^2\Pi_{3/2}(f)\rangle = \frac{|{}^2\Pi_{3/2}\rangle - |{}^2\Pi_{-3/2}\rangle}{\sqrt{2}}, \quad (1.100)$$

$$|{}^2\Pi_{1/2}(e)\rangle = \frac{|{}^2\Pi_{1/2}\rangle + |{}^2\Pi_{-1/2}\rangle}{\sqrt{2}}, \quad (1.101)$$

$$|{}^2\Pi_{1/2}(f)\rangle = \frac{|{}^2\Pi_{1/2}\rangle - |{}^2\Pi_{-1/2}\rangle}{\sqrt{2}}. \quad (1.102)$$

Since the e and f levels degenerate, the Hamiltonian can be represented by

$$\begin{pmatrix} A/2 + B((J+1/2)^2 - 2) & -B\sqrt{(J+1/2)^2 - 1} \\ -B\sqrt{(J+1/2)^2 - 1} & -A/2 + B(J+1/2)^2 \end{pmatrix} \quad (1.103)$$

with the basis $\{|^2\Pi_{3/2}(e/f)\rangle, |^2\Pi_{1/2}(e/f)\rangle\}$.

The discussion on the degenerated levels depends on the strength of the coupling between the angular momenta and is commonly discussed using the *Hund's cases* [65, 82, 86, 87]. Hougen [65] classified Hund's cases using the quantum numbers that appear in the rotational energy level and the good quantum numbers in non-rotating molecules. Table. 1.2 summarize Hund's cases.

Table1.2: Summary of Hund's cases

Coupling case	Rotational energy level expression	Good quantum numbers in the nonrotating molecule	Degeneracy in the nonrotating molecule
Hund's case (a)	$BJ(J+1)$	$\Lambda, S, \Sigma, \Omega$	1 (for Σ states) 2 (for others)
Hund's case (b)	$BN(N+1)$	$\Lambda, S, \Sigma, \Omega$	$(2S+1)$ (for Σ states) $2(2S+1)$ (for others)
Hund's case (c)	$BJ(J+1)$	Ω	1 (for 0 states) 2 (for others)
Hund's case (d)	$BR(R+1)$	$L, \Lambda, S, \Sigma, \Omega$	$(2L+1)(2S+1)$

Hund's case (a) is the case of $A \gg BJ$, i.e., the spin-orbit coupling term \hat{H}_{SO} is large relative to the rotational term \hat{H}_{rot} . Hund's case (b) is the other case ($A \ll BJ$). In Hund's case (a), the larger separation of the diagonal element $\Delta E = (A/2 + B((J+1/2)^2 - 2)) - (-A/2 + B(J+1/2)^2) \sim A$ than the off-diagonal element $-B\sqrt{(J+1/2)^2 - 1} \sim -BJ$, then the energy levels are shifted by $\pm(-BJ)^2/A$. The eigenvalues are

$$\begin{aligned} E_{3/2}(J) &= A/2 + B((J+1/2)^2 - 2) + B^2((J+1/2)^2 - 1)/A + \dots \\ &= A_{\text{eff}}/2 + B_{3/2(\text{eff})}((J+1/2)^2 - 1), \end{aligned} \quad (1.104)$$

$$\begin{aligned} E_{1/2}(J) &= A/2 + B(J+1/2)^2 - B^2((J+1/2)^2 - 1)/A + \dots \\ &= -A_{\text{eff}}/2 + B_{1/2(\text{eff})}((J+1/2)^2 - 1) \end{aligned} \quad (1.105)$$

where

$$A_{\text{eff}} := A - 2B, \quad (1.106)$$

$$B_{3/2(\text{eff})} := B + B^2/A, \quad (1.107)$$

$$B_{1/2(\text{eff})} := B - B^2/A. \quad (1.108)$$

Considering the e and f components, the energy diagram can be written as shown in Fig. 1.7. The energy levels are twofold degenerated for each J . Considering Hund's case (b) for the general states $^{2S+1}\Lambda$ as well as the $^2\Pi$ states, the energy levels are $B_{\Omega(\text{eff})}J(J+1)$ and twofold degenerated (e/f) [88].

Hund's case (b) is the case of $A \ll BJ$, i.e., the splitting between the spin components of $^2\Pi_{1/2}$ and $^2\Pi_{3/2}$ is smaller than Hund's case (a). Suppose spin-orbit coupling is

zero, i.e., $A = 0$. In other words, it is a pure Hund's case (b). Diagonalizing the Hamiltonian, the energy levels are derived as

$$\begin{aligned} E_{\pm}(J) &= B((J + 1/2)^2 - 1) \pm (4B^2 + 4B^2((J + 1/2)^2 - 1))^{1/2}/2 \\ &= B((J + 1/2)^2 - 1) \pm B(J + 1/2). \end{aligned} \quad (1.109)$$

Then,

$$E_+ = B(N^2 - 1) + BN = B(N(N + 1) - 1), \quad (1.110)$$

$$E_- = B((N + 1)^2 - 1) - B(N + 1) = B(N(N + 1) - 1). \quad (1.111)$$

It means the energy levels are $B(N(N + 1) - 1)$ and fourfold degenerated (+/- and e/f) for each N as shown in Fig. 1.8

Considering Hund's case (b) for the general states $^{2S+1}\Lambda$ as well as the 2Pi states, the energy levels are $BN(N + 1)$ and the degeneracy is $2S + 1$ for $\Lambda = 0$ i.e. Σ states and $2(2S + 1)$ for $\Lambda \neq 0$ [88].

Hund's cases (a) and (b) are quite simplified and do not consider some coupling (spin-rotation, spin-spin), Λ doubling, centrifugal distortion, and so on. Hund's cases (c) and (d) point to cases where the difference between the level of the electronic states is smaller than A and BJ .

Hund's case (c) is the case of small separation for each electronic state with the large spin-orbit coupling (similar to Hund's case (a)), i.e., $A \gg BJ$ and $A \gg \Delta E_{el}$, where ΔE_{el} is the difference between nearby electronic levels. Molecules with heavy atoms tend to Hund's case (c) because spin-orbit coupling increases for Z .

In this case, since \hat{H}_{SO} induces large spin-orbit splittings and extensive mixing of electronic wavefunctions, except for J and Ω , no other numbers are good quantum numbers. Therefore, the term symbol $^{2S+1}\Lambda_{\Omega}$ is no longer meaningful. The term symbol in Hund's case (c) is described as Ω with parity, e.g., 0_u^+ . The rotational energy level is $B_{eff}J(J + 1)$ for each Ω state as similar as Hund's case (a).

Hund's case (d) is the case of small separation for each electronic state with the small spin-orbit coupling in the internuclear axis for Rydberg electrons, i.e., $A \ll BJ$ and $A \gg \Delta E_{el}$. The example of this case is molecules with Rydberg electronic states. The Rydberg electron is far from the nuclei, and then the spin-orbit coupling is quite weak. In this case, the rotational energy level is $BR(R + 1)$ and the degeneracy is $(2L + 1)(2S + 1)$ [88].

Mulliken [89] defined Hund's case (e) that the L and S are strongly coupled, but the coupling of L to the electric axis is small [82]. This case is quite rare, and few examples are reported [90].

1.1.3.3 Parity and selection rules

■ **Rotationless parity (e/f)** The total parity clearly depends on $J - 2\Sigma + S + \sigma$ from equation 1.9. e/f states have different parities even though they have the same J .

This parity is called Rotationless Parity and is defined as follows:

$$\hat{E}^* \psi = +(-1)^J \psi \quad \text{for } e \text{ and } J \text{ is intager,} \quad (1.112)$$

$$\hat{E}^* \psi = +(-1)^{J-1/2} \psi \quad \text{for } e \text{ and } J \text{ is half-intager,} \quad (1.113)$$

$$\hat{E}^* \psi = -(-1)^J \psi \quad \text{for } f \text{ and } J \text{ is intager,} \quad (1.114)$$

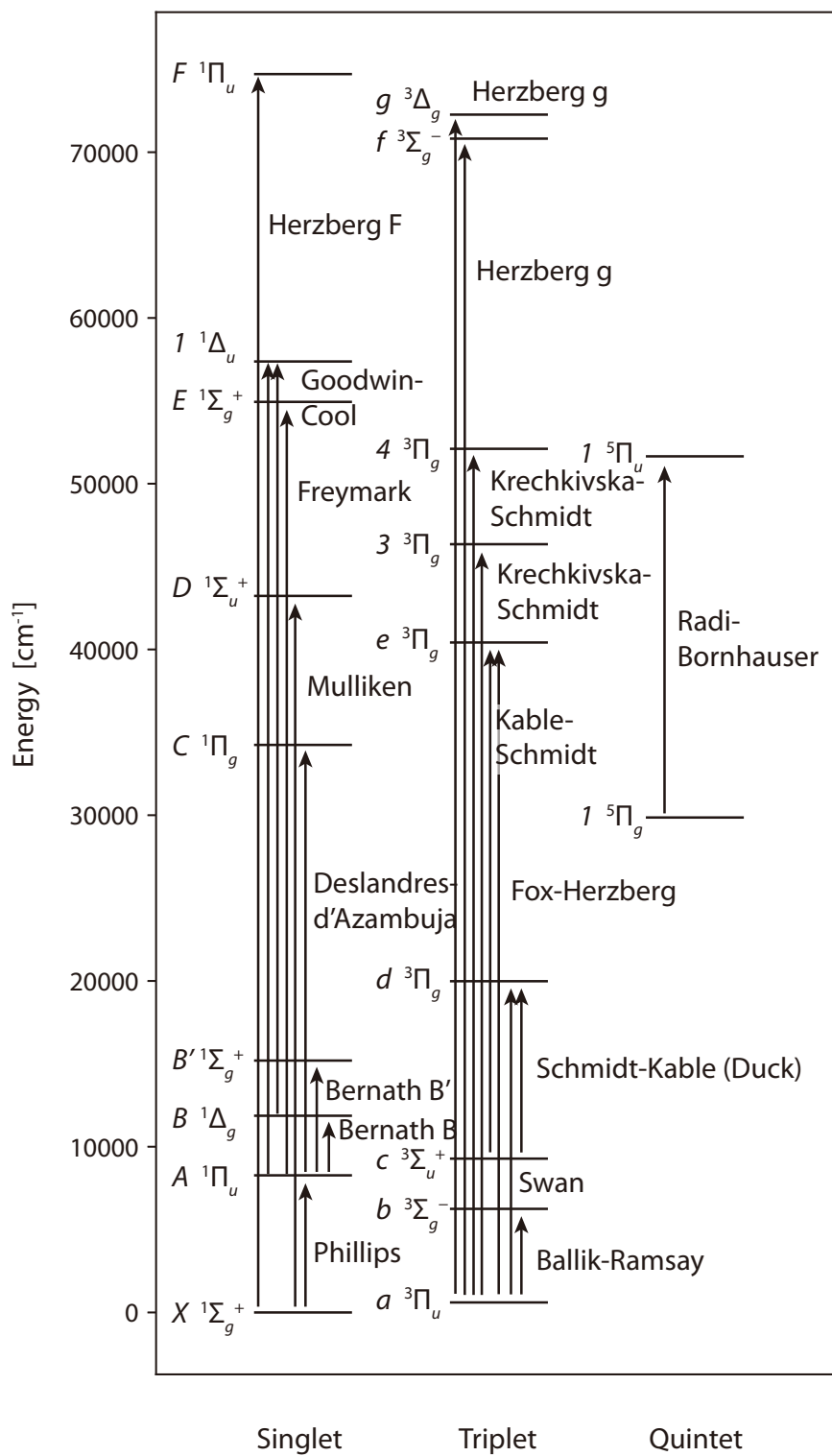
$$\hat{E}^* \psi = -(-1)^{J-1/2} \psi \quad \text{for } f \text{ and } J \text{ is half-intager.} \quad (1.115)$$

Note that all rotational energy levels of $^1\Sigma^+$ states have e parity, those of $^1\Sigma^-$ states have f parity, and those of $^1\Pi$ states have e/f pairs.

The allowable transitions regarding rotationless parity are

$$e \leftrightarrow e \quad \text{and} \quad f \leftrightarrow f \quad \text{for } P \text{ and } R \text{ branches } (\Delta J = \pm 1), \quad (1.116)$$

$$e \leftrightarrow f \quad \text{for } Q \text{ branch } (\Delta J = 0). \quad (1.117)$$



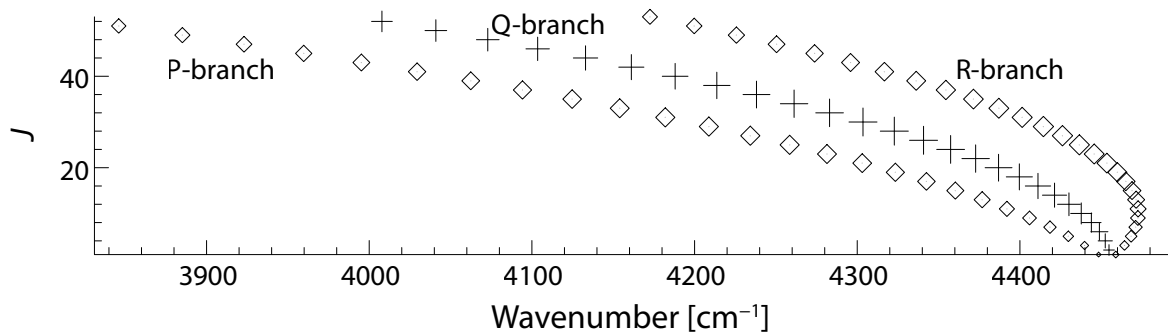


Figure 1.4: The Fortrat diagram of the transition $A^1\Pi_u v' = 3 - X^1\Sigma_g v'' = 1$ of the neutral carbon dimer C_2 (Phillips band) as an example of Singlet–Singlet transition. Spectral constants were taken from Davis *et al.* [84].

N	J	total parity	rotationless parity	
3	3.5	–	e	=====
	2.5	–	f	=====
2	3.5	+	e	=====
	1.5	+	f	=====
1	1.5	–	e	=====
	0.5	–	f	=====
0	0.5	+	e	=====

Figure 1.5: The energy level diagram of $^2\Sigma^+$ states. In the case of $^2\Sigma^-$, the total parity is inverted.

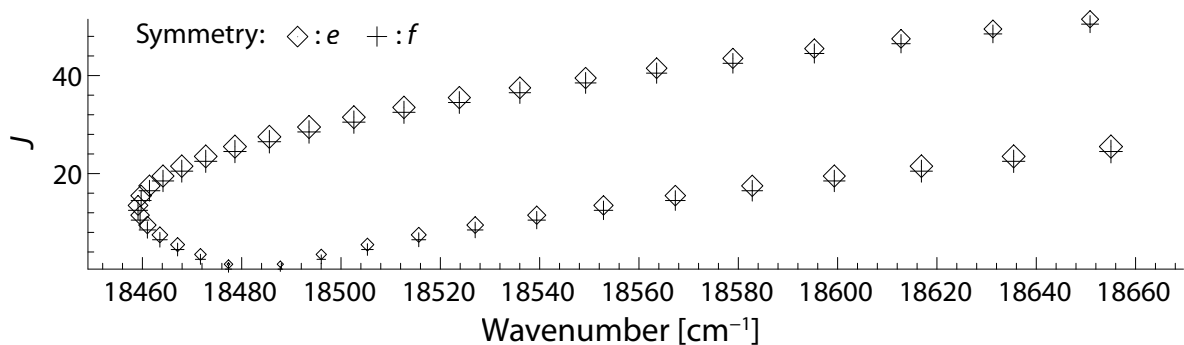


Figure 1.6: The Fortrat diagram of the transition $B^2\Sigma_u^+ v' = 0 - X^2\Sigma_g^+ v'' = 0$ of the carbon dimer anion C_2^- (Herzberg-Lagerquist band) as an example of $^2\Sigma^+ - ^2\Sigma^+$ transition. Spectral constants were taken from Jones *et al.* [85].

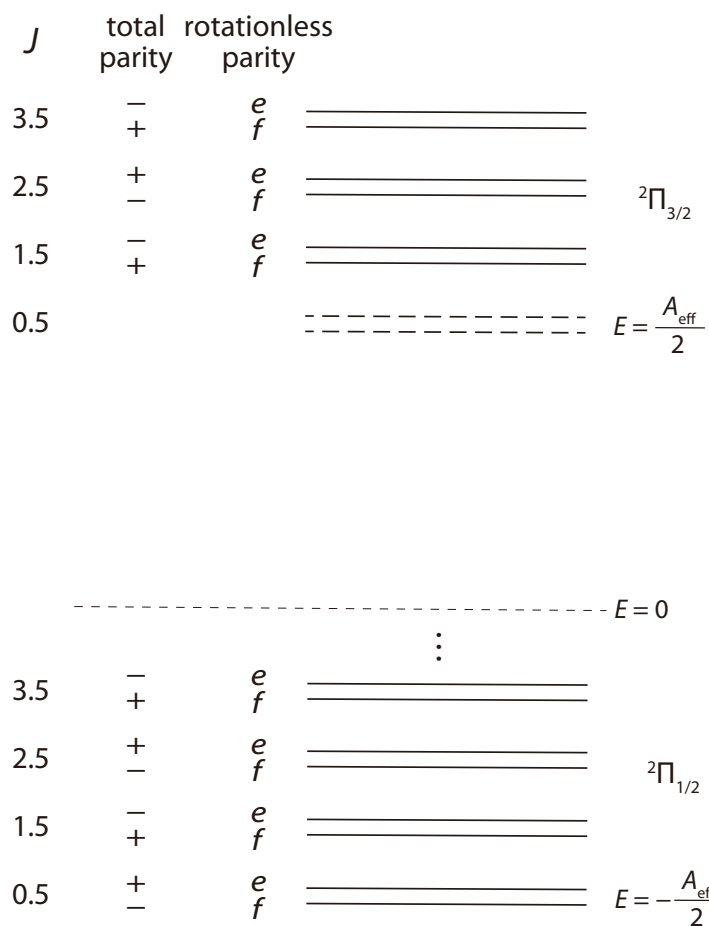


Figure 1.7: The energy level diagram of ${}^2\Pi$ state corresponding to Hund's case (a).

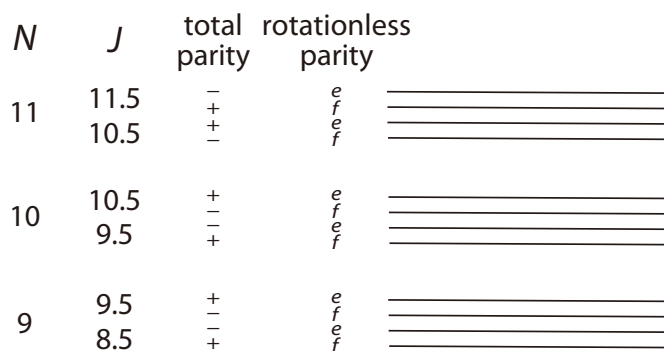


Figure 1.8: The energy level diagram of ${}^2\Pi$ state corresponding to Hund's case (b).

1.2 Outline of the previous spectroscopic studies of carbon dimer anion

In this section, the previous studies on spectroscopy and time evolution of carbon dimer will be outlined. The carbon dimer anion C_2^- has been the subject of extensive spectroscopic research and theoretical calculations for over half a century. Gas-phase and matrix studies of the $X^2\Sigma_g^+$, $A^2\Pi_u$, and $B^2\Sigma_u^+$ states will be outlined. The previous study of the time evolution of electronic detachment from highly excited states will also be outlined.

1.2.1 Electronic state of C_2^-

Negative molecular ions have long been the focus of much attention due to their unique characteristics. An electron experiences no net Coulomb attraction at large distances r from a neutral molecule. However, many molecules can bind this extra electron and thus have a positive electron affinity due in part to short-range attractive polarization potentials, which falls off as $1/r^4$ [91, 92]. Binding energies of valence electrons in anions tend to be much smaller than those of neutrals and cations, and the weakly bound electron densities make them largely polarizable and, therefore, reactive with surrounding atoms and molecules. Molecular anions possess few, if any, bound electric excited states, again in sharp contrast to cations and neutrals; however, their precise properties or even existence have often been debated. This is partly due to the need for theoretical calculations that rigorously treat electron correlation effects, which play an essential role in anions, and partly due to the relative lack of experimental techniques for preparing and storing these anions in a vacuum for long periods of time.

Among the variety of molecular anions, C_2^- is one of the most studied anions in the gas phase ever since its successful isolation via mass spectrometry by Honig. [2]. Since it has been studied for a long time, there are several old reviews on spectroscopy [93–96].

Fig. 1.9 shows the molecular orbital diagram of carbon dimer and Table 1.3 shows the main configuration of C_2^- from Zeitz *et al.* [52]. Since the ground state of C_2^- is near-degenerate from the first excited state, Hartree-Fock and density functional theory are not sufficient to obtain the eigenstates. Then the eigenstates are expressed as a linear combination of configuration state functions (CSF) by the configuration interaction method (CI). The configuration state function is usually called *configuration* for short, and the configuration with the largest coefficient in the eigenstate is called the main configuration. The configuration depends greatly on the internuclear distances. For example, regarding $B^2\Sigma_u^+$ state, the percentage of $1\sigma_g^2 1\sigma_u^2 2\sigma_g^2 2\sigma_u^1 1\pi_u^4 3\sigma_g^2$ is 83.5 % at the potential minimum (1.24 Å), but around 2.1 Å it is 0.5 %, and the main configuration is $1\sigma_g^2 1\sigma_u^2 2\sigma_g^2 2\sigma_u^1 1\pi_u^3 3\sigma_g^1 1\pi_g^1$ (59.4 %), and the next is $1\sigma_g^2 1\sigma_u^2 2\sigma_g^2 2\sigma_u^1 1\pi_u^3 3\sigma_g^1 2\pi_g^1$ (20.7 %).

Using the nature that C_2^- has multiple bound electronic states, Yzombard *et al.* [44]

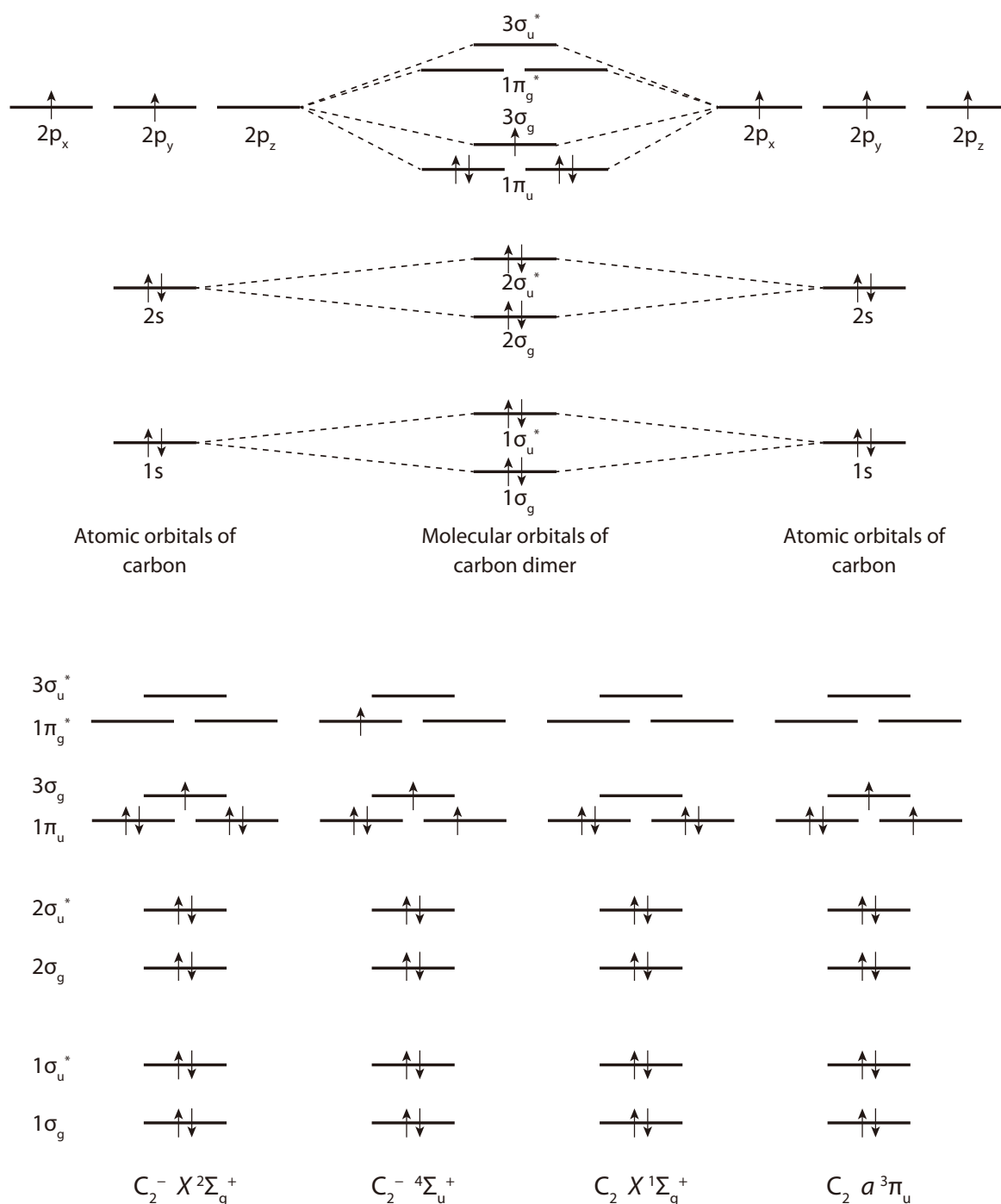


Figure 1.9: The molecular orbital diagrams of the electronic ground state of carbon dimer anion $C_2^- X^2\Sigma_g^+$, a state with no optical transition from the ground state $C_2^- X^4\Sigma_u^+$, and the states of neutral carbon dimer $C_2 X^1\Sigma_g^+$, $a^3\Pi_u$

Table 1.3: Main configuration of C_2^- cited from Zeitz *et al.* [52].

State	Main configurations
$X^2\Sigma_g^+$	$1\sigma_g^2 1\sigma_u^2 2\sigma_g^2 2\sigma_u^2 1\pi_u^4 3\sigma_g^1$ (88.0 % at the internuclear distances of 1.24 Å)
$A^2\Pi_u$	$1\sigma_g^2 1\sigma_u^2 2\sigma_g^2 2\sigma_u^2 1\pi_u^3 3\sigma_g^2$ (90.0 % at the internuclear distances of 1.24 Å)
$B^2\Sigma_u^+$	$1\sigma_g^2 1\sigma_u^2 2\sigma_g^2 2\sigma_u^1 1\pi_u^4 3\sigma_g^2$ (83.5 % at the internuclear distances of 1.24 Å)
$^4\Sigma_u^+$	$1\sigma_g^2 1\sigma_u^2 2\sigma_g^2 2\sigma_u^1 1\pi_u^3 3\sigma_g^1 2\pi_g^1$ (68.5 % at the internuclear distances of 1.38 Å)
$^4\Delta_u^+$	$1\sigma_g^2 1\sigma_u^2 2\sigma_g^2 2\sigma_u^1 1\pi_u^3 3\sigma_g^1 2\pi_g^1$ (62.6 % at the internuclear distances of 1.38 Å)
$^4\Sigma_u^-$	—
$^4\Sigma_g^+$	—
$^4\Sigma_g^-$	—

recently proposed it as a target for laser cooling, which has yet to be achieved for any negative ion. Fig. 1.10 shows potential energy curves of C_2^- plotted using Morse potentials [72] based on existing experimental data [84, 97–101] and theoretical calculations [51]. The proposal by Yzombard *et al.* [44] uses the transitions of $X^2\Sigma_g^+ \leftrightarrow A^2\Pi_u$ and $X^2\Sigma_g^+ \leftrightarrow B^2\Sigma_u^+$.

The particular feature of C_2^- as a dimer anion is the existence of two bound electronic excited states $A^2\Pi_u$ and $B^2\Sigma_u^+$, both of which are allowed to decay into the ground state $X^2\Sigma_g^+$ by electric-dipole (E1) transitions.

1.2.2 Adiabatic electron affinity of C_2

C_2 is one of the molecules with a large electron affinity.*² Table. 1.4 shows the list of the electron affinity of diatomic molecules from Rienstra-Kiracofe *et al.* [102].

There are two definitions of electron affinity: *adiabatic electron affinity* is defined by the energy difference between the rovibrational ground states of the neutral and its anion. On the other hand, *vertical electron affinity* is the difference between the energy of the neutral's rovibrational ground state and the anion's potential energy at the same internuclear distance as the neutral.

In C_2 , the adiabatic electron affinity is defined as the energy of the $C_2 X^1\Sigma_g^+ v = 0 - C_2^- X^2\Sigma_g^+ v'' = 0$ transition, and this value is 3.2727 ± 0.0004 eV [63].

The experimental studies of the electron affinity is listed in Table 1.5. The measurement of the electron affinity of C_2 originated with Honig [2] and can be precisely measured by photoelectron spectroscopy. The theoretical calculations of the electron affinity of C_2 have difficulty even when large-scale basis functions can be used. Because the electronic ground state of C_2 is substantially multi-referential, the electron correlation plays a crucial role [103]. The theoretical calculation is listed in Table 1.6. Only Lu [104] is in agreement with the latest measurement results of Laws *et al.* [63].

*² C_2 has the largest electron affinity of all the homonuclear diatomic molecules listed in a large survey, Rienstra-Kiracofe *et al.* [102].

Table1.4: the electron affinity the diatomic molecules with molecular weight less than 57 obtained by photoelectron spectroscopy cited from Rienstra-Kiracofe *et al.* [102]

species	EA [eV]	transition ($M^- \rightarrow M$)
LiH	0.342 ± 0.012	$2\Sigma^+ \rightarrow 1\Sigma^+$
LiD	0.337 ± 0.012	$2\Sigma^+ \rightarrow 1\Sigma^+$
BeH	0.70 ± 0.10	$\text{---} \rightarrow 2\Sigma^+$
CH	1.238 ± 0.008	$3\Sigma^- \rightarrow 2\Pi$
Li ₂	0.437 ± 0.009	$2\Sigma_u^+ \rightarrow 1\Sigma_g^+$
NH	0.370 ± 0.004	$2\Pi^- \rightarrow 3\Sigma^-$
OH	1.827653 ± 0.000004	$1\Sigma^+ \rightarrow 2\Pi$
OD	1.825548 ± 0.000037	$1\Sigma^+ \rightarrow 2\Pi$
C ₂	3.269 ± 0.006	$2\Sigma_g^+ \rightarrow 1\Sigma_g^+$
MgH	1.05 ± 0.06	$\text{---} \rightarrow 2\Sigma^+$
BN	3.160 ± 0.005	$2\Sigma^+ \rightarrow 3\Sigma^-$
¹³ C ₂	3.270 ± 0.010	$2\Sigma_g^+ \rightarrow 1\Sigma_g^+$
CN	3.862 ± 0.004	$1\Sigma^+ \rightarrow 2\Sigma^+$
BO	2.508 ± 0.008	$1\Sigma^- \rightarrow 2\Sigma^+$
SiH	1.277 ± 0.009	$3\Sigma^- \rightarrow 2\Pi$
NO	0.026 ± 0.005	$3\Sigma^- \rightarrow 2\Pi$
O ₂	0.451 ± 0.007	$2\Pi \rightarrow 3\Sigma_g^-$
PH	1.028 ± 0.010	$2\Pi \rightarrow 3\Sigma^-$
SH	2.317 ± 0.002	$1\Sigma^+ \rightarrow 2\Pi$
SD	2.315 ± 0.002	$1\Sigma^+ \rightarrow 2\Pi$
FO	2.272 ± 0.006	$1\Sigma^+ \rightarrow 2\Pi$
CaH	0.93 ± 0.05	$\text{---} \rightarrow 2\Sigma^+$
LiCl	0.593 ± 0.010	$2\Sigma^+ \rightarrow 1\Sigma^+$
NaF	0.520 ± 0.010	$2\Sigma^+ \rightarrow 1\Sigma^+$
AlO	2.60 ± 0.01	$\text{---} \rightarrow 2\Sigma^+$
CS	0.205 ± 0.021	$2\Pi \rightarrow 1\Sigma^+$
Na ₂	0.430 ± 0.015	$2\Pi \rightarrow 1\Sigma_g^+$
NS	1.194 ± 0.011	$1\Sigma^+ \rightarrow 2\Pi$
PO	1.092 ± 0.010	$1\Sigma^+ \rightarrow 2\Pi$
SO	1.125 ± 0.005	$2\Pi \rightarrow 3\Sigma^-$
ClO	2.276 ± 0.006	$1\Sigma^+ \rightarrow 2\Pi$
SF	2.285 ± 0.006	$1\Sigma^+ \rightarrow 2\Pi$
CrH	0.563 ± 0.010	—
Al ₂	1.46 ± 0.06	—
AlSi	1.32 ± 0.05	$3\Sigma^- \rightarrow 4\Sigma^-$
MnH	0.869 ± 0.010	$6\Delta \rightarrow 7\Sigma^+$
Si ₂	2.202 ± 0.010	$2\Sigma_g^+ \rightarrow 3\Sigma_g^-$

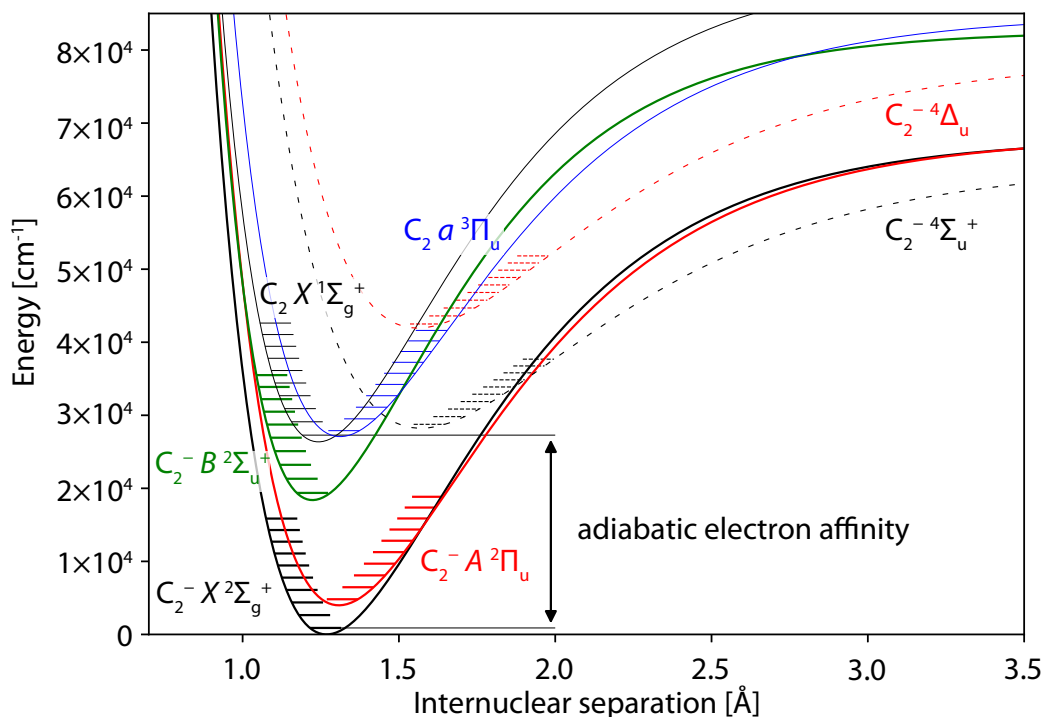


Figure 1.10: Potential energy curves of C_2^- based on existing experimental data (C_2^- : $X^2\Sigma_g^+$, $A^2\Pi_u$ [97, 98], $B^2\Sigma_u^+$ [99], C_2 : $X^1\Sigma_g^+$ [84], $a^3\Pi_u$ [100]). As an example of existing theoretical suggestion of the quartet states of C_2^- , the potential energy curves of $^4\Sigma_u^+$ and $^4\Delta_u$ calculated by Thulstrup & Thulstrup [51] are shown with dashed lines. The electron affinity is 3.2727 ± 0.0004 eV [63].

Table 1.5: The experimental studies for the adiabatic electron affinity of C_2^-

reference	year	method	electron affinity [eV]
Honig [2]	1954	graphite sublimation	4.0 or 3.1
Trepka <i>et al.</i> [105]	1963	electron impact	≥ 2.9
Feldmann [106]	1970	photodetachment threshold	3.54 ± 0.05
Locht <i>et al.</i> [107]	1970	electron impact threshold	3.3 ± 0.2
Jones <i>et al.</i> [85]	1980	autodetachment spectroscopy	$3.374 \geq EA \geq 3.408$
Yang <i>et al.</i> [7]	1988	photoelectron spectroscopy	3.3 ± 0.1
Ervin <i>et al.</i> [101]	1991	photoelectron spectroscopy	3.268 ± 0.007
Arnold <i>et al.</i> [108]	1991	photoelectron spectroscopy	3.273 ± 0.008
Laws <i>et al.</i> [63]	2019	photoelectron spectroscopy	3.2727 ± 0.0004

Table 1.6: The theoretical calculations for the adiabatic electron affinity of C_2^-

reference	year	method	electron affinity [eV]
Barsuhn <i>et al.</i> [50]	1974	SCF CI	1.6
Thulstrup <i>et al.</i> [51]	1974	CI	3.5
Cederbaum <i>et al.</i> [109]	1977	Green's function method	3.60
Zeitz <i>et al.</i> [52]	1979	MRD-CI	3.43
Dupuis <i>et al.</i> [110]	1980	CISD+Q/STO	3.30
Gollisch [111]	1981	density matrix	3.97
Novoa <i>et al.</i> [112]	1986	MP2(FC)/6-311+G(2d,2p)	3.43
Novoa <i>et al.</i> [112]	1986	MP3(FC)/6-311+G(2d,2p)	2.94
Nichols <i>et al.</i> [113]	1987	MCSCF-MCEP	3.112
Watts <i>et al.</i> [103]	1992	CCSD(T) PVQZ+ <i>sp</i>	3.198
Sordo [114]	2001	CCSD(T) (FC)/CBS(aVDTQZ)	3.239
Sordo [114]	2001	CCSDT(FC)/CBS(aVDTQZ)	3.300
Musia <i>et al.</i> [115]	2003	EA-EOM-CCSDT/cc-pV ∞ Z	3.23
Musia <i>et al.</i> [115]	2003	EA-EOM-CCSDT/aug-cc-pV ∞ Z	3.24
Lu [104]	2004	OUQMC/FSGO-SGG	3.264 \pm 0.043
Feller <i>et al.</i> [116]	2016	CCSD(T)/aV8Z	3.267 \pm 0.002
Gulania <i>et al.</i> [117]	2019	EOM-CC/ROHF	3.42

1.2.3 Spectroscopy of the ground state and bound excited states

The beginning of C_2^- rovibronic spectroscopy was the discovery of the $B-X$ transition spectrum by Herzberg and Lagerquist [55] in absorption spectroscopy, then $B-X$ transition band is called Herzberg-Lagerquist band (HL band). Cathro *et al.* [118] also measured the absorption spectrum in the same way.

The high intensity tunable and fixed-frequency lasers has made it possible to perform advanced studies of the interaction of negative ions with photons such as photodetachment spectroscopy. There are two types of experimental approach of photodetachment [119]. The first approach is to fix the laser wavelength and detect the kinetic energy of the photoelectron with an electron energy analyzer. A fixed frequency laser is inserted to the ion beam. This method is suitable for measuring the electron affinity with high accuracy. The other method is to use a wavelength tunable laser to detach the electron and count neutralized particles or detached electrons.

In 1972, Lineberger *et al.* [120] obtained the photodetachment spectra in the low-vibration region of X state by a two-photon process through the B state. Jones *et al.* [85,121], Mead *et al.* [119] and Mead *et al.* [99], also in the Lineberger group, obtained the photodetachment spectra of the high rotational states ($X v'' \geq 6$, $B v' \geq 5$) by a one-photon process. Especially, Mead *et al.* [99] discussed the perturbation of B states by $A^2\Pi_u$ state. Nakajima [122] obtained the spectroscopic constant of $B v = 4-6$, which is complementary work of Jones *et al.* [85] and Mead *et al.* [99]. The

spectroscopic constants they obtained are summarised in Table. 1.7.

Table 1.7: The experimental studies for the spectroscopic constants of C_2^-

Dunham parameter	$X^2\Sigma_g^+$			$A^2\Pi_u$			$B^2\Sigma_u^+$		
	Herzberg ^{*1}	Jones	Mead	Rehfuss	Mead	Rehfuss	Herzberg ^{*1}	Jones	Mead
T_e	0	0	0	0	4064(91)	3985.83(50)	18390.88	18391.047(93)	18390.723(35)
$Y_{10} (\omega_e)$	1781.04	1781.329(66)	1781.202(20)	1781.189(18)	1656(10)	1666.4(10)	1968.73	1969.076(165)	1969.542(84)
$Y_{20} (-\omega_e x_e)$	-11.58	-11.719(18)	-11.6716(48)	-11.6717(48)	-10.80(26)	10.80(26) ^{*2}	-14.43	-14.902(98)	-15.100(57)
$Y_{30} (\omega_e y_e)$	-0.027	-0.00683(129)	-0.00998(28)	0.00998128 ^{*2}	—	—	-0.324	-0.1500(220)	-0.135(16)
$Y_{40} (\omega_e z_e)$	—	—	—	—	—	—	—	-0.0191(16)	-0.0153(17)
$Y_{01} (B_e)$	1.7468	1.746510(394)	1.74649(16)	1.74666(32)	1.630(5)	1.64305(334)	1.8774	1.877021(394)	1.87718(27)
$Y_{11} (-\alpha_e)$	-0.0167	-0.016594(68)	-0.016557(76)	-0.01651(46)	-0.0152	-0.01601(44)	-0.0177	-0.017326(92)	-0.01887(28)
$Y_{21} (\gamma_e)$	—	-2.62(89) $\times 10^{-5}$	-3.2(7) $\times 10^{-5}$	—	-2.4 $\times 10^{-5}$	—	0.00037	-4.69(18) $\times 10^{-4}$	1.15(67) $\times 10^{-4}$
$Y_{02} (-D_e)$	-6.69 $\times 10^{-6}$	-6.66(8) $\times 10^{-6}$	—	—	—	—	-6.84 $\times 10^{-6}$	-6.74(9) $\times 10^{-6}$	—
$Y_{12} (-\beta_e)$	0	—	—	—	—	—	-0.10 $\times 10^{-6}$	-0.14(3) $\times 10^{-6}$	—
$Y_{03} (H_e)$	—	—	—	—	—	—	—	—	—

^{*1} Herzberg *et al.* [55] did not explicitly state that those spectral constants are for X, B states.

^{*2} Although the signs appear to be reversed, the original values are quoted verbatim.

citation

Herzberg *et al.* [55], Jones *et al.* [85], Mead *et al.* [99], Rehfuss *et al.* [98]

Ervin *et al.* [101] used photoelectron spectroscopy to determine the vibrational ground state energies of X and A in C_2^- and X and a in C_2 with high accuracy. Arnold *et al.* [108] and Laws *et al.* [63] also obtained photoelectron spectroscopy of $C_2^- X$ and $C_2 X$ and a . De Beer *et al.* [123] succeeded in controlling the vibrational state by exciting $X v'' = 0$ states to $X v'' = 1$ via $B v' = 0$ using stimulated Raman pumping method. They obtained the Raman frequency dependence of the population of each rotational level by detached the electron using a two photon process from $C_2 X$ and detecting the photoelectrons. Bragg *et al.* [124] performed an angle-resolved measurement of photoelectron using time-resolved photoelectron imaging technique.

The spin-splitting constants of $X v'' = 0$ and $v'' = 1$ were obtained by Rehfuß *et al.* [98], and the spin-splitting constants of $B v' = 0$ state was obtained by Royen *et al.* [125] using velocity modulation laser spectroscopy. Recently, Nötzold *et al.* [126] precisely obtained the spin-splitting constants of $X v'' = 0$ and $B v' = 0$ using cryogenic ion trap to study the transition for laser cooling.

Shan-Shan *et al.* [127] also employed a variation of velocity modulation laser spectroscopy [128] and obtained HL band. Mahoney *et al.* [1] obtained the HL band by measuring the optical emission from the plasma produced by microwave plasma-activated chemical vapor deposition reactor [129].

The HL band measurement was often performed spectroscopically with a rare-gas matrices. Milligan *et al.* [130] obtained the absorption spectra of the acetylene and argon matrix and tentatively assigned them to HL band. Frosch [131] obtained the absorption and emission spectra of the HL band and the Swan band [69] ($d^3\Pi_g - a^3\Pi_u$ of C_2 neutral) in Ar, Kr, and Xe matrices. Graham *et al.* [132] obtained emission spectra in Ar and alkali metals matrix. Brus *et al.* [133] found that C_2^- in the Ar matrix causes a Personev effect, a phenomenon in which the emission peaks of molecules in the crystal become extremely narrow despite inhomogeneous broadening of the absorption peaks [134]. Bondybey *et al.* [56] suggested that some of the relaxation processes in the $B^2\Sigma_u^+$ state may go through the $4\Sigma_u^+$ state. Rasanen *et al.* [135] obtained the absorption spectra of the laser-vaporized graphite in solid neon.

Table 1.8: Theoretical calculations on X, A, B states, and higher excited states of C_2^-

reference	year	calculation	calculated states except X, A, B	neutral C_2X	method
Popkie [136]	1971	transition moment	—	none	HF
Barsuhn [50]	1974	potential curve	$4\Sigma_u^+$	none	SCF & CI
Thulstrup <i>et al.</i> [51]	1974	potential curve	$4\Sigma_u^+, 4\Delta_u, 4\Sigma_u^-, 4\Sigma_g^+, 4\Sigma_g^-$	calculated	CI
Cade <i>et al.</i> [137]	1974	HFR wavefunction	—	—	HFR
Zeitz <i>et al.</i> [52]	1979	potential curve	$4\Sigma_u^+, 4\Delta_u$	calculated	CI
Dupuis <i>et al.</i> [110]	1980	potential curve	none	none	SCF, MCSCF, CI
Rosmus <i>et al.</i> [138]	1984	radiative transition probabilities	none	—	MCSCF-SCEP
Nichols <i>et al.</i> [113]	1987	potential curve	none	calculated	MCEP
Watts <i>et al.</i> [103]	1992	molecular constant	none	none	CCSD(T)
Botschwina <i>et al.</i> [139]	1995	molecular constant	none	none	RCCSD(T)
Bruna <i>et al.</i> [140]	2000	g -factor	none	none	CI
Gorfinkiel <i>et al.</i> [141]	2005	scattering calculations	no bound state can be found	calculated	MRMPS
Šedivcová <i>et al.</i> [142]	2006	transition dipole moment	none	none	icMRCI
Halmová <i>et al.</i> [53]	2006	scattering calculations	no bound state can be found	calculated	CASCI
Halmová (PhD thesis) [54]	2008	scattering calculations	no bound state can be found	calculated	CASCI
Shi <i>et al.</i> [143]	2016	potential curve	$4\Sigma_u^+, 4\Sigma_u^-, 4\Pi_u$	none	CASSCF
Gulania <i>et al.</i> [117]	2019	potential curve	none	calculated	EOM-CCSD

Abbreviation

HF : Hartree-Fock method, SCF : self-consistent field method, CI : configuration interaction method, HFR : Hartree-Fock-Roothaan method, MCSCF : multi-configurational self-consistent field method, SCEP : self - consistent electron pairs method, MCEP : multiconfigurational electron propagator method, CCSD(T) : coupled-cluster singles, doubles (and triples) method, RCCSD(T) : coupled-cluster singles, doubles (and triples) method for a partially spin-adapted formalism, MRMPS : molecular R-matrix with pseudostates method, icMRCI : internally contracted multireference configuration interaction method, CASCI : complete active space configuration interaction method, CASSCF : complete active space self-consistent field method, EOM-CCSD : equation-of-motion coupled-cluster singles and doubles method

The first theoretical studies of the A state have been performed by Popkie *et al.* [136], but the low-lying nature of the A state made it difficult to study it experimentally until the development of tunable infrared lasers. The Rehfuss *et al.* [98] and Oka [97] obtained the A - X transition spectrum by absorption spectroscopy and obtained the spectroscopic constants of the A state.

We have found no reports regarding spectroscopic experiments on the other electronic excited state, especially, quartet states. However, several (often conflicting) theoretical calculations of their potential energy curves are available [50–53, 141, 143]. Thulstrup & Thulstrup [51] (CI with AO basis) and Zeitz *et al.* [52] (MRD-CI with AO basis) indicated that the anion quartet state ${}^4\Sigma_u^+$ exists close to and below the ground state of neutral C_2 . They also suggested other quartet states such as ${}^4\Delta_u$ and others above ${}^4\Sigma_u^+$. Shi *et al.* [143] (MRCI with the aug-cc-pcV5Z-dk basis) calculated the lowest quartet state of ${}^4\Sigma_u^+$. However, they suggested the next higher level to be ${}^4\Sigma_g^+$. On the other hand, Gorfinkiel *et al.* [141] and Halmová *et al.* [53] (CASCI with the double-zeta plus polarization Gaussian basis set) reported a negative result on the existence of bound quartet states. For illustrative purposes, the potential energy curves of the quartet states ${}^4\Sigma_u^+$ and ${}^4\Delta_u$ calculated by Thulstrup & Thulstrup [51] are shown in Fig. 1.10.

Table 1.8 shows the published theoretical calculations of X , A , B , and higher excited states of C_2^- except for the calculation of the electron affinity.

1.2.4 Electronic and vibrational relaxation processes of the bound excited states and the ground states

The bound excited states A and B can deexcite to X by emitting a photon. Leutwyler *et al.* [144] experimentally revealed that the lifetime of B $v' = 0$ is 77 ± 8 ns and the lifetime of B $v' = 1$ is 73 ± 7 ns. Rosmus *et al.* [138] theoretically derived that the radiative lifetimes of the A states are several tens of μ s for $v' = 0$ –10. Table. 1.9 shows their theoretical calculation of the lifetimes.

The vibrationally excited states of the X state de-excite via electronic transitions to near-degenerate low-lying vibrational levels of the A states and *vice versa* [46, 49, 138, 145]. Recently, Iida *et al.* [145] succeeded in clear observation of such relaxation process accompanying the A - X vibronic coupling in the region of a few tens of ms utilizing an ion storage ring (TMU E-ring).

1.2.5 Autodetachment from B ${}^2\Sigma_u^+$ state

An excited anion with potential energies above the detachment threshold can make a transition into the neutral by detaching the excess electron. This transition is called *autodetachment*. For instance, the radiative lifetime of the B state to X state is about 80 ns for $v' = 0$ [52, 56, 118, 138, 142–144], while, higher vibrational states ($v' \geq 5$) also decay into C_2 ${}^1\Sigma_g^+ + e^-$ via autodetachment.

Hefter *et al.* [146] found that the autodetachment rate for B $v' = 6$ –10 is about 10^7 – 10^{10} s^{-1} . In addition, because the peak shape in the photodetachment spectrum of B - X was not asymmetric, they revealed that the detachment from X by the one-

Table 1.9: The MCSCF-SCEP calculation of the lifetimes of $C_2^- X^2\Sigma_g^+$, $A^2\Pi$, $B^2\Sigma_u^+$ by Rosmus *et al.* [138]. The energy level of $B^2\Sigma_u^+ v' \geq 5$ is above detachment threshold, but it is not taken into account.

vibrational level	$X^2\Sigma_g^+$ [ms]	$A^2\Pi$ [μ s]	$B^2\Sigma_u^+$ [ns]
0	—	49.9	76.5
1	—	40.6	75.8
2	—	34.6	75.3
3	2000	30.5	75.1
4	541	27.4	75.3
5	206	25.0	76.0
6	98	23.2	77.3
7	55	21.8	79.3
8	34	20.6	82.0
9	23	19.6	85.5
10	16	18.8	90.0

photon process has almost no direct transition to the continuous state. Hence, for $B v' \geq 6$, autodetachment is the dominant decay process of the B state.

1.2.6 Earlier experiments with ion storage rings and ion trap on autodetachment of C_2^-

In several lifetime measurements using ion storage devices, autodetachment from excited states with an extended lifetime of several ms has been observed. Pedersen *et al.* [46] performed lifetime measurements by storing C_2^- in the magnetic storage ring ASTRID [147,148] with the cesium sputter ion source ANIS [149] and a Micro Sphere Plate (MSP) detector. They found a decaying autodetachment component with a lifetime of 2.5 ms and proposed that a hitherto unobserved quartet state, such as $^4\Sigma_u^+$, was responsible as shown in 1.11. Andersen *et al.* [45] employing ASTRID [147,148] and Naaman *et al.* [49] employing an electrostatic ion trap for storage of fast ion beams also reported the observation of such autodetachment component of a few ms lifetime, and Takao *et al.* [47] employing TMU E-ring [150] reported the 3 ms component.

While there is clearly a state which is autodetached on the time scale of ms in C_2^- , it is not clear whether this state is a highly vibrational or rotational state in the X , A , or B states or some other electronic states. If it is a quartet state, as Pedersen *et al.* [46] suggests, it is not in accord with Halmová *et al.*'s theoretical calculation [53] that there are no bound quartet states.

Pedersen *et al.* [46] also argued that there are long-lived quartet states because the neutral signal detached by 415 nm, 478.4 nm, 526 nm lived for ~ 10 s. On the other hand, Naaman *et al.* [49] showed that the neutral signal detached by 532 nm also lived for long time but there are no long-lived components of the neutral signal detached

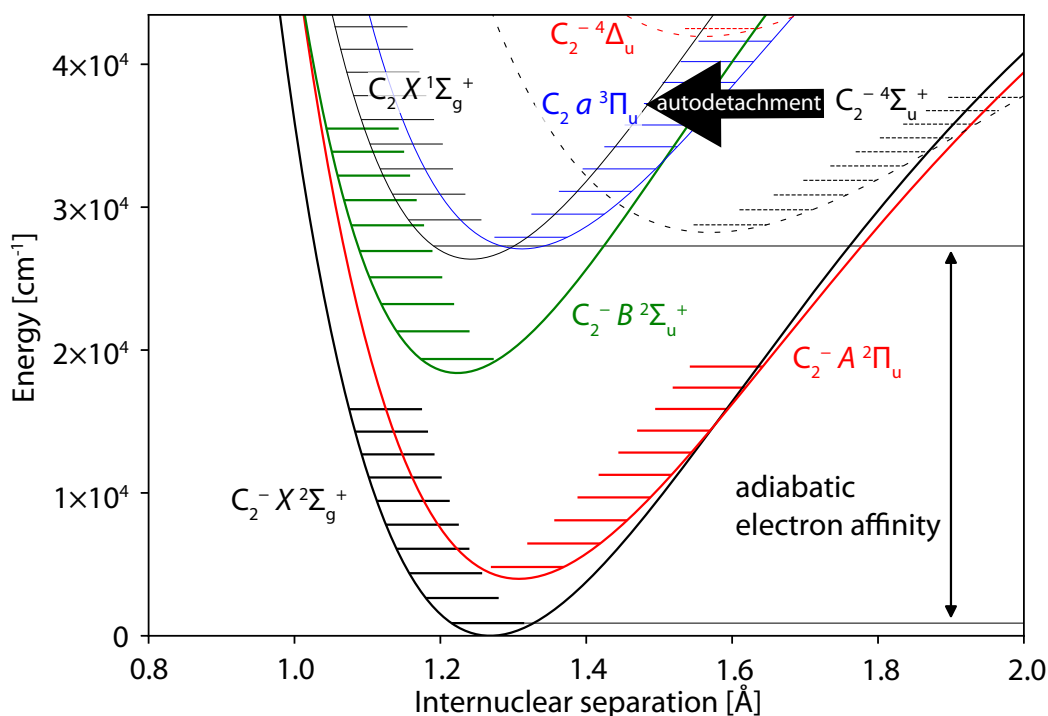


Figure 1.11: The schematics of autodetachment from the excited states with the potential energy above the detachment threshold.

by 1064 nm. The energy of the vibrational ground state of the quartet states should be higher than that of the vibrational ground state of B state, so that even at 1064 nm ($\sim 10^4 \text{ cm}^{-1}$) the detachment threshold is exceeded. It implies there are no long-lived quartet states. However, they did not take into account the possibility that it resonates in 532 nm etc. but not in 1064 nm. To determine whether this is a resonance or not, a wavelength scanning measurement should be performed. The presence or absence of long-lived states other than the ground state X will be analyzed in this thesis through the obtained time-resolved spectra.

C_2^- storage experiments using a cryogenic ion storage ring have recently been started. None of these results have been published. Kono *et al.* (private communication at a conference) [48] simultaneously measured fragment ion yield in addition to neutral yield using a cryogenic ion storage ring DESIREE [151, 152], distinguishing between autodetachment and autodissociation. Their preliminary results show that neutral yield has a decay lifetime on the time scale of several ms, and that autodissociation is the dominant decay process after 25 ms. Göck [153] measured fragment ion yield by storing C_2^- in a cryogenic ion storage ring CSR [154, 155] for 23 s and 520 s with a fragment detector COMPACT [156]. A variety of lifetime components are observed, then the decay of the total fragmentation was approximately $1/t$. The $1/t$ law is also found in autodissociation of some kinds of metal dimer anions, such as Cu_2^- and Ag_2^- [157].

Chapter 2

Experimental method

2.1 Photodetachment spectroscopy

Photodetachment spectroscopy is a technique of obtaining spectra by counting the number of neutral particles or electrons produced by electron detachment of anions using variable wavelength light. Photodetachment spectroscopy is a type of action spectroscopy, that obtains a spectrum by measuring the reciprocal number of photons required to induce a photochemical reaction.

There are three main types of anion spectroscopy: one is absorption spectroscopy. From the absorption spectrum, we can obtain the wavelengths of optical transitions and their transition probabilities. The HL band was first observed by absorption spectroscopy [55]. However, absorption spectroscopy is not suitable for observing transitions from states with small population or with small transition probabilities.

The second method, termed photodetachment spectroscopy, counts neutralized particles by injecting a wavelength-tunable laser into the anion beam. The obtained spectra do not simply show the difference between the energy level of the initial state and the detachment threshold. In the case of C_2^- , for example, the probability of a direct transition from the $C_2^- X^2\Sigma_g^+$ state to the $C_2 + e^-$ (i.e., the continuum state) is very low [146]. On the other hand, from the $B^2\Sigma_u^+$ state ($v' \geq 5$), which is a state higher than the energy level of the ground state $X^1\Sigma_g^+$ of neutral C_2 , autodetachment occurs on the time scale of ns [146]. Thus, electron detachment is induced by photo-transition from the $X^2\Sigma_g^+$ state to the $B^2\Sigma_u^+$ state ($v' \geq 5$) as shown in Figure 2.1. Jones *et al.* [85] was the first to measure the HL band using this technique. They succeeded in observing $B^2\Sigma_u^+ - X^2\Sigma_g^+$ transitions up to $B v' \leq 7$ with $\Delta v = -1$, whereas absorption spectroscopy by Herzberg *et al.* [55] only obtained $v' \leq 3$. If transition spectra with $B v' \leq 4$ as the final state is to be obtained using this technique, it has to be further excited to detach the electron. There are two possible excitation processes for the second transition: 1. direct photoexcitation from the $B^2\Sigma_u^+$ state to the continuum state as shown in Figure 2.2, and 2. autodetachment by excitation from the $B^2\Sigma_u^+$ state to the highly vibrational state of the $X^2\Sigma_g^+$ state. If 2 is correct, the second $B^2\Sigma_u^+ - X^2\Sigma_g^+$ transition should be represented in the spectrum, but no such structure can be found [145]. Also, it is the transition with $\Delta v \sim 25$, which indicates that the transition probability should be very low.

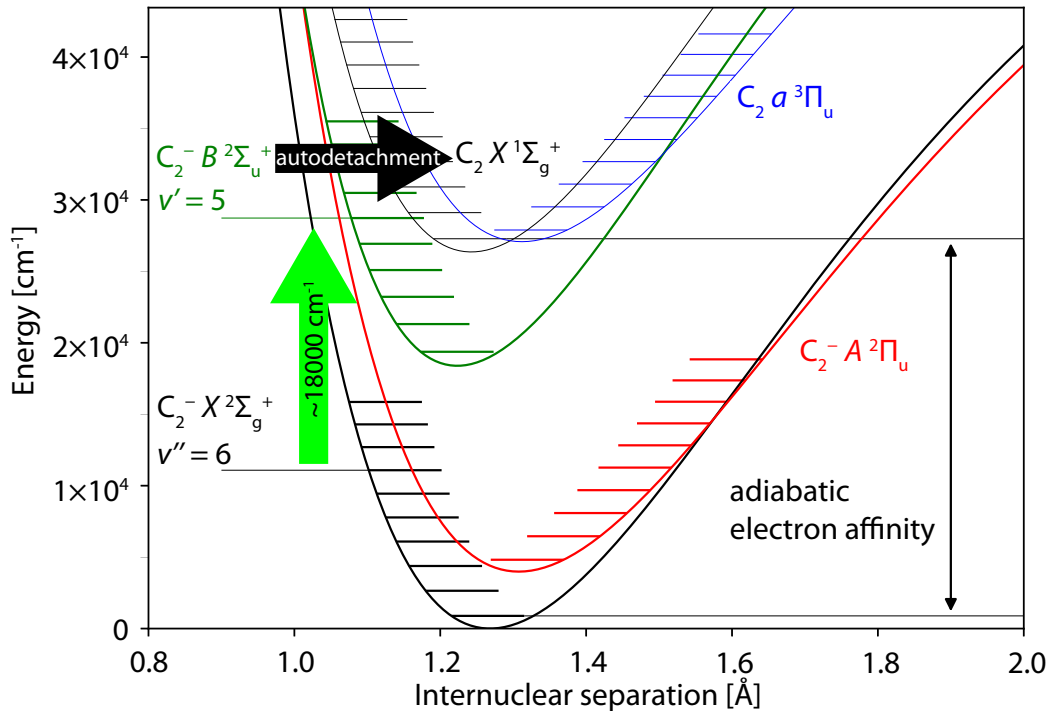


Figure 2.1: The schematics of 1 photon detachment.

The third method, termed photoelectron spectroscopy, is to measure the energy of detached electrons. If the wavelength of the laser for detachment is fixed, the horizontal axis is the energy of the electrons, and the vertical axis is their count number, the transition probabilities to each state of the neutral are obtained. Additionally, it is used to measure electron affinity with high precision, as shown in Table 1.5.

In this study, photodetachment spectroscopy will be employed. This is because Absorption spectroscopy is not suitable for observing small population states, and photoelectron spectroscopy is difficult to perform using an ion storage ring. In order to investigate the spectroscopic constants of the high vibrational state of the bound excited state B ($v' \geq 5$), the process of photoexcitation to $X v'' \rightarrow B v' = v'' - 1$ and autodetachment to neutral C_2 was observed as shown in Fig. 2.1. As discussed later, the process of photoexcitation from $X v'' = 0$ to $B v' = 0$ and then photodetachment from $B v' = 0$ was also observed as shown in Fig. 2.2. Since this photodetachment process is not through resonance, the laser intensity must be large. The laser power dependence of the number of detached neutrals was measured.

We performed spectroscopic experiments using a cesium-sputter ion source, which can produce high-temperature negative ion beams. This ion source could not be used for spectroscopic experiments since the produced beam was quite hot, and too many transition spectra were observed to make the assignment impossible [158]. We cooled this ion beam using a cryogenic ion storage ring RICE to produce a beam that selectively left only the ground state and long-lived highly excited states.

A schematic of the experimental setup is shown in Fig. 2.3. The C_2^- beam was generated with a cesium-sputter ion source and stored in the cryogenic electrostatic

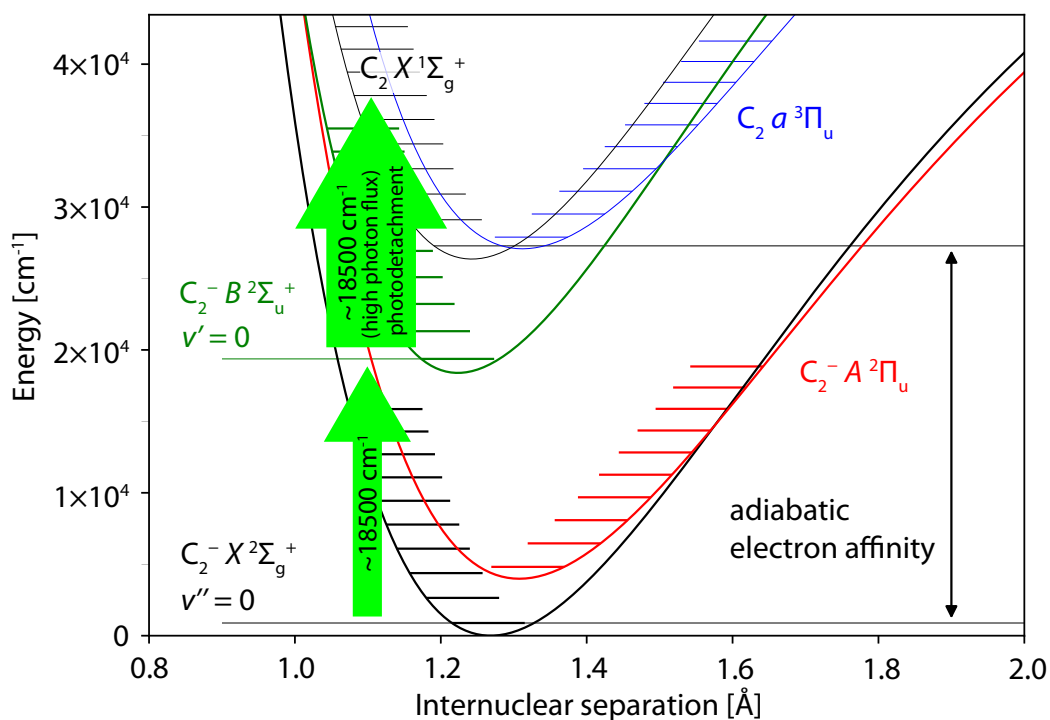


Figure 2.2: The schematics of 2 photon detachment.

ion storage ring RICE [57] with a circulation period of $15\ \mu\text{s}$ after mass-selection. Ions are typically stored in this ring for several thousands of seconds. A tunable pulsed laser was injected coaxially with the ion beam when the ions passed through the straight section of the ring. The wavelength spectrum was obtained by counting the neutral particles. Storage time, defined as the elapsed time from pulsing by the chopper, was controlled by the timing of the laser insertion. The flight time until insertion into RICE was about $15\ \mu\text{s}$. Fig. 2.4 shows the brief timing chart of the switching voltages and neutral counts.

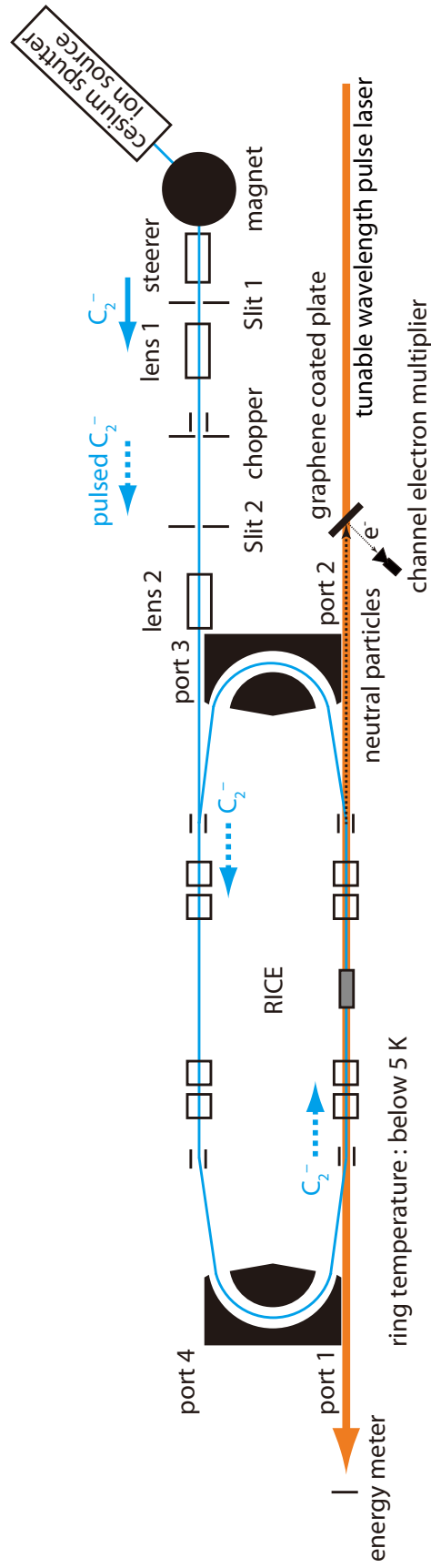


Figure 2.3: Schematic overview of the present experimental setup. This figure is quoted from Iizawa *et al.* [159] under the CC BY 4.0 license.

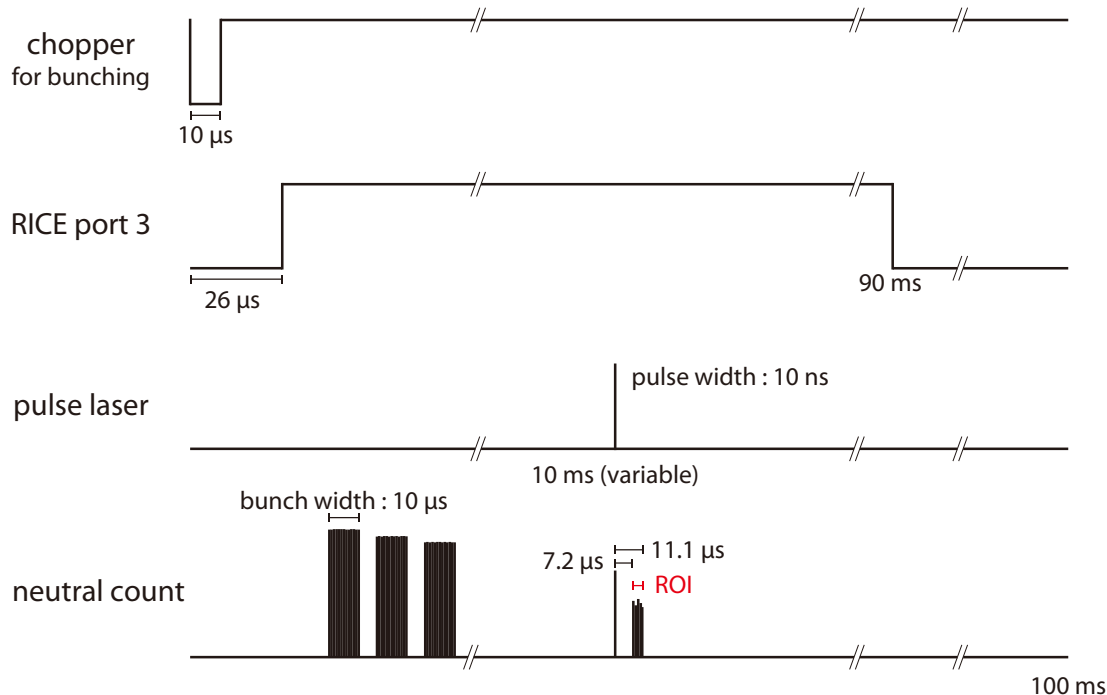


Figure 2.4: The brief timing chart of the switching voltages and neutral counts.

2.2 Ion source and mass selection

A C_2^- beam was generated by a cesium-sputter ion source (NEC, SNICS II). Fig. 2.5 is the brief schematics of a cesium-sputter ion source. A cesium sputter ion source is a device that produces a negative ion beam by sputtering a target (cathode; several kV is applied) with cesium cation, which is made from cesium vapor by surface ionization and extracting only anion from the sputtered material. A cathode was fabricated from isotropic graphite (Toyo Tanso, IG-11) and confined in a copper holder. C_2^- ions were extracted from the ion source at an acceleration voltage of 5 kV and mass-selected by a dipole magnet and Slit 1. In this study, 5 kV was applied to the cathode, 3.85 kV to the extractor (einzellens), 19 A to the ionizer, 25 A to the pipe heating for the cesium vapor, and 0.9 A to the cesium oven. The bias voltage to the entire ion source was 0 V. An electromagnet for mass selection was operated at 0.164 T (1.371 A applied).

To confirm the resolution of the mass selection in advance, we measured the ion beam intensity at the closed Slit 2 after passing through the dipole magnet and Slit 1. The result is shown in Fig. 2.6. The peaks at $m/q = 24$ and 25 are clearly separated, and the width of each peak is consistent with the resolution defined by the dipole magnet and Slit 1, *i.e.*, $\Delta(m/q)/(m/q) = 2.1\%$. The peak $m/q = 25$ is considered to include $^{12}C_2H^-$ in addition to $^{13}C^{12}C^-$ because the observed intensity ratio of peak $m/q = 25$ against $m/q = 24$ is 5%, while the natural abundance of $^{13}C^{12}C$ is 2%. Fig.

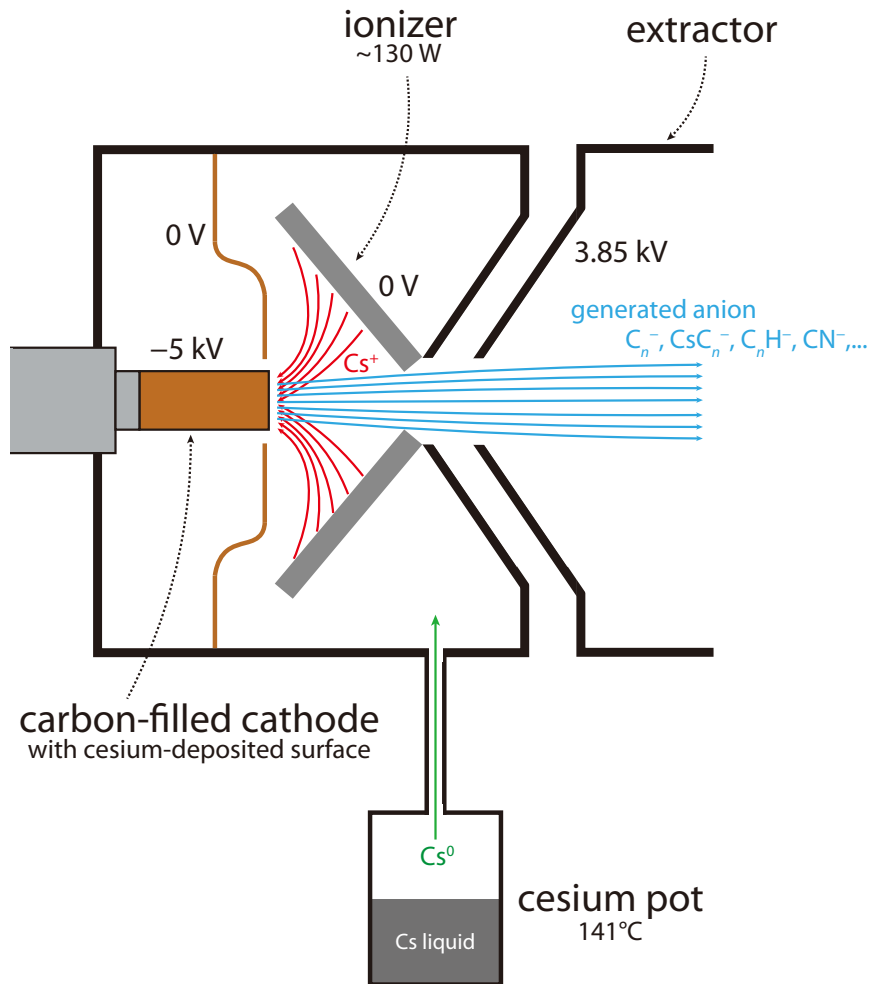


Figure 2.5: Brief schematics of a cesium-sputter ion source.

2.7 shows Gaussian fitting to $m/q = 24, 25$ peaks. By accounting for the possible overlap between peak $m/q = 24$ and the tail of the $m/q = 25$ component, we judged that the contamination of $^{12}\text{C}_2\text{H}^-$ is negligibly small ($\leq 10^{-5}$).

Using a chopper device, the C_2^- ions were pulsed into bunches with a $10\ \mu\text{s}$ width and injected into the cryogenic electrostatic ion storage ring RICE [57] after passing through Slit 2. RICE is operated at cryogenic temperatures below 5 K, and thus $A-X$ excitations due to blackbody radiation are effectively suppressed. Since RICE maintains an ultra-high vacuum of about 1×10^{-10} Pa at a room-temperature-equivalent pressure, the collisional detachment by residual gas is also negligible compared with autodetachment or laser-induced detachment. The circulation period of C_2^- ions is $15\ \mu\text{s}$ at 5 keV beam energy, and the typical lifetime of the stored ions is several orders of magnitude longer than the time region of the present study (100 ms). The purity of the C_2^- beam was also checked by observing the temporal evolution of the ion bunches via the neutral particle detector. If contamination from ions with $m/q = 25$ occurs, broadening or an additional tail in the bunch structure would be expected as the ions circulate in the ring [161].

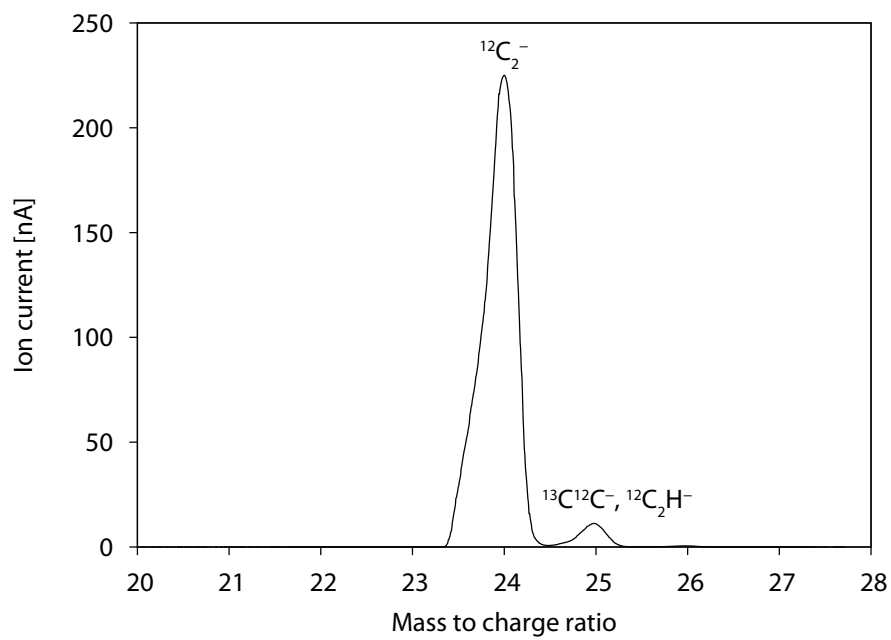


Figure 2.6: A typical mass-scan of the ion beam extracted from the ion source. This figure is quoted from Iizawa *et al.* [159] under the CC BY 4.0 license.

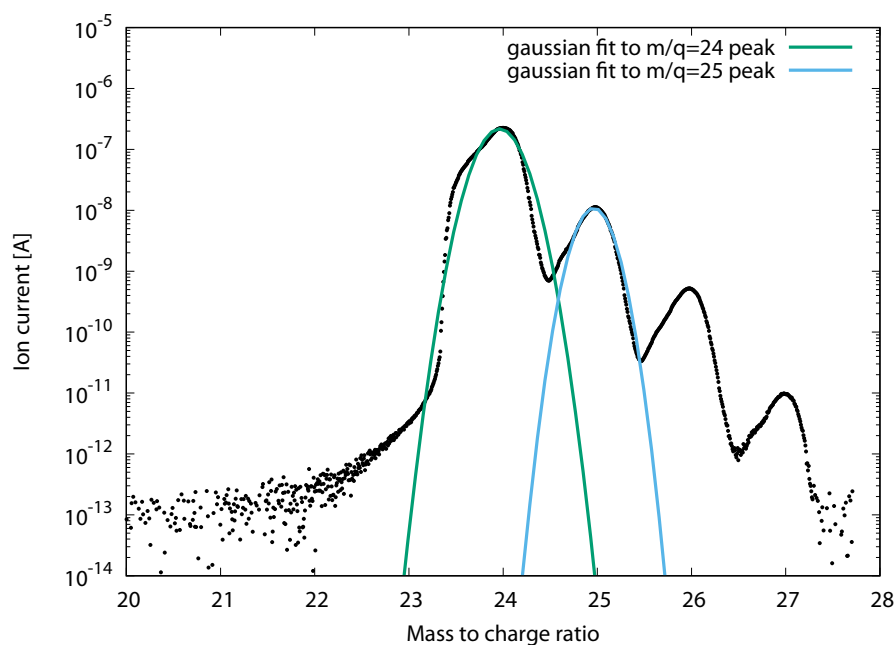


Figure 2.7: Gaussian fitting to $m/q = 24, 25$ peaks, with logarithmic vertical axis. The plotted data are the same as in Fig. 2.6. The peak at $m/q = 26$ contains $^{12}\text{C}^{14}\text{N}^-$ in addition to $^{13}\text{C}_2^-$, $^{13}\text{C}^{12}\text{CH}^-$, $^{12}\text{C}_2\text{D}^-$. Cesium sputter ion sources are known to produce larger amounts of CN^- than C_2^- with carbon cathode under nitrogen gas conditions [160]. Since N_2 was present in the residual gas, CN^- was likely to be generated. $m/q = 27$ peak is about 10^{-2} times the peak height of $m/q = 26$. Since the natural abundance ratio of ^{13}C is about 10^{-2} times that of ^{12}C , this peak contains $^{13}\text{C}^{16}\text{N}^-$, $^{12}\text{C}^{17}\text{N}^-$, $^{13}\text{C}_2\text{H}^-$, and $^{13}\text{C}^{12}\text{CD}^-$.

2.3 Cryogenic electrostatic ion storage ring RICE

An ion storage ring is a device that uses electrostatic or magnetic fields to store and accelerate/decelerate ion beams. The ion storage ring reduces the momentum resolution of the ion beam $\Delta p/p$. This reduction is called *beam cooling*. The phase space volume of the particles that make up the beam is called *emittance* and is used to evaluate the convergence of the beam. Emittance is conserved for beam acceleration and focusing. An ion storage ring can reduce the emittance for beam cooling.

The ion storage ring RICE, used in this experiment, has two major features: the orbit is controlled by an electrostatic field, and the ion beam can be stored in cryogenic environment.

The bending radius of an ion beam in a static magnetic field is proportional to \sqrt{mE}/q where m is the ion mass, E is the translational energy of the ion, and q is the ion charge, making it difficult to store low-charge, heavy ions. In addition, the hysteresis of the electromagnets makes it difficult to modify the magnetic field rapidly to take out the ion beam.

On the other hand, an electrostatic storage ring allows ions to orbit independently of mass and charge because the curvature radius is proportional to E/q and $E = qV$ where V is electrode's voltage, making it easy to store low-valence, heavy ions, such as molecular ions. The ring itself is compact than a static magnetic field ring.

The first atomic and molecular physics experiment using a magnetostatic ion storage ring was performed in 1993 at Test Storage Ring (TSR) [162, 163] developed by the Max Planck Institute [164]. Although there are some examples of molecular ion storage in magnetostatic ion storage rings, such as TRAN II at the University of Tokyo [165], ASTRID at Aarhus University [166, 167] and CRYRING at Stockholm University [168], an electrostatic ion storage ring was necessary for large-molecular ion storage experiments. In 1998, an electrostatic storage ring ELISA at Aarhus University was developed [169], followed by the development of electrostatic ion storage rings such as ES-ring at High Energy Accelerator Research Organization (KEK) [170] and TMU E-ring [150] at Tokyo Metropolitan University.

There are three cryogenic electrostatic ion storage rings, CSR at the Max Planck Institute [154, 155], DESIREE at the Stockholm University [151, 152], and RICE at RIKEN [57], that can be operated at cryogenic temperatures. There are two major advantages of these rings: 1. the stored ions are barely affected by background radiation. 2. The residual gas density is extremely small (e.g. $2.7 \times 10^4 \text{ cm}^{-3}$ in RICE; pressure equivalent to 10^{-10} Pa [57]), which enables long time storage on the time scale of 10^3 s .

The schematic of RICE is shown in Fig. 2.8. The RICE contains two 160° deflectors, four 10° deflectors, and four sets of electrostatic quadrupole lenses. Table 2.1 and 2.2 shows the applied voltages to the electrodes of RICE and the beamline. Beam injection and extraction are enabled by switching the voltage of the 10° deflectors. Pick-up electrodes is installed at ten locations in the center of the straight section, and the beam bunch structure can be observed.

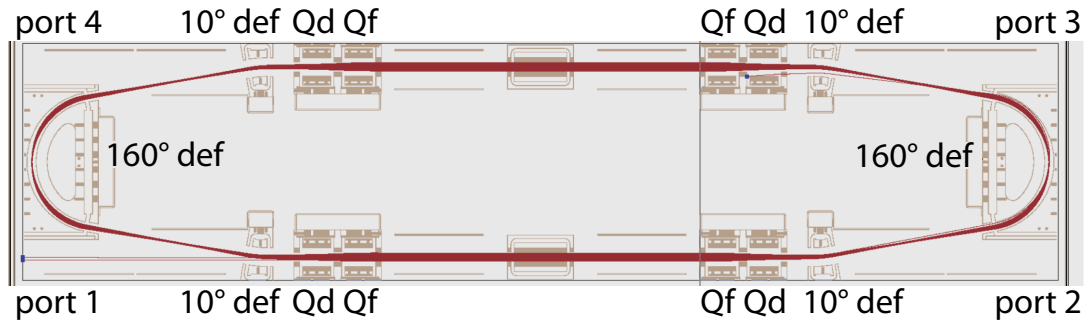


Figure2.8: The schematics of RICE

Table2.1: The applied voltages to the electrodes of RICE.

quadrupole lens			
port No.	lens	horizontal electrodes [V]	vertical electrodes [V]
#1	Qd	-104.072	+125.000
#1	Qf	+119.010	-104.865
#2	Qd	-102.793	+99.000
#2	Qf	+91.456	-115.090
#3	Qd	-111.713	+70.826
#3	Qf	+71.844	-106.493
#4	Qd	-104.072	+125.000
#4	Qf	+119.010	-104.865

10° deflector		
port No.	inner electrodes [V]	outer electrodes [V]
#1	+901.000	-718.700
#2	+814.700	-771.722
#3	+823.000	-772.033
#4	+901.000	-718.700

160° deflector		
port No.	inner electrodes [V]	outer electrodes [V]
#1-4	+613.900	-684.433
#2-3	+697.200	-718.700

Table2.2: The applied voltages to the electrodes of beamline.

steerer		
	horizontal electrodes [V]	vertical electrodes [V]
upstream	25	3
downstream	0	0
quadrupole lens (lens 1)		
	horizontal electrodes [V]	vertical electrodes [V]
upstream	+10	-10
middle	-20	20
downstream	0	0
quadrupole lens (lens 2)		
	horizontal electrodes [V]	vertical electrodes [V]
upstream	-97	+97
downstream	+97	-97
offset		
	horizontal electrodes [V]	vertical electrodes [V]
upstream	+9	-5
downstream	+6	-5

2.4 Tunable laser

Light pulses from a tunable OPO laser (Continuum Sunlite, 10 Hz) were injected collinearly to the stored ion beam at the straight sections from port 2 to port 1. The laser pulse energy was measured by an energy meter (Coherent FieldMaxII-TOP) at port 1, as shown in Fig. 2.3. Fig. 2.9 is the schematics of laser system. The wavenumber of the laser was simultaneously monitored during measurements using a wavemeter (HighFinesse WS-6).

The typical linewidth is 0.075 cm^{-1} and the pulse width is 10 ns. The Doppler shift correction was taken into account. Since $^{12}\text{C}_2^-$ is stored at 5.0 keV, the translational velocity of the ion beam is $2.0 \times 10^5 \text{ m/s}$. Therefore, the Doppler correction can be made as in

$$\lambda' = \lambda \frac{1 - \frac{2.0 \times 10^5}{c}}{\sqrt{1 - \left(\frac{2.0 \times 10^5}{c}\right)^2}} \approx \lambda(1 - 6.7 \times 10^{-4}) \quad (2.1)$$

where λ is the measured wavelength, λ' is the wavelength after Doppler shift correction, and c is the speed of light. The wavenumber $18\,500.0 \text{ cm}^{-1}$ is shifted toward larger 12.3 cm^{-1} by the Doppler shift correction.

The wavenumber range used for the measurement was around $17\,600\text{--}18\,600 \text{ cm}^{-1}$ ($537.63\text{--}568.18 \text{ nm}$ in wavelengths). The fluctuation of the center of the wavenumber for each pulse was around $\pm 0.01 \text{ cm}^{-1}$ (1σ). The maximum laser pulse energy was 5 mJ, and since the diameter of the beam was about 50 mm at the port 2 of the RICE the energy density is $2.6 \times 10^{-1} \text{ mJ/cm}^2$. The laser pulse energy was mainly used as 1 mJ ($5.1 \times 10^{-2} \text{ mJ/cm}^2$ in energy density) to prevent two-photon processes. The fluctuation of the laser pulse energy for each pulse was evaluated to be $\pm 27\%$ (1σ).

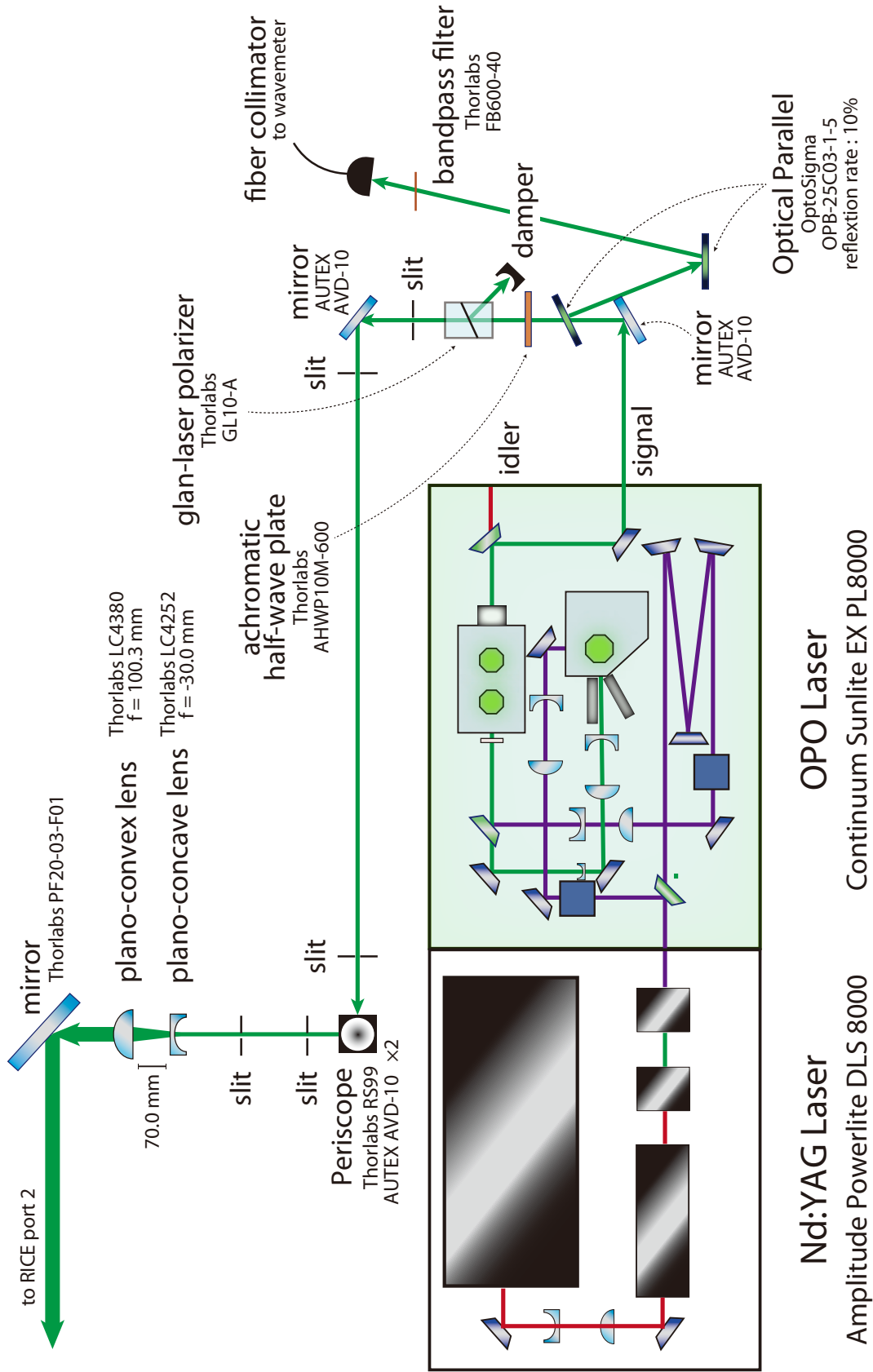


Figure2.9: The schematics of laser system

2.5 Neutral particle detector

Fig. 2.10 shows the schematics of the graphene-based neutral particle detector developed by Warbinek *et al.* [171], which was installed at the port 2 of RICE as shown in Fig. 2.3. When a neutral particle strikes a graphene plate to which a negative voltage is applied, secondary electrons are emitted. These secondary electrons are collected by a channel electron multiplier (Dr. Sjuts Optotechnik GmbH KBL 25RS) through electrostatic lens and counted by a discriminator and a time-to-digital converter. The graphene plate as shown in Fig. 2.11 was fabricated by transcription of two 75×75 mm graphene sheets made by chemical vapor deposition (CVD) to 85×85 mm $t = 2.0$ fused silica plate (Shibuya optical WQ2-80S). The four corners of the plate were gold coated for voltage application. Since the bi-layer graphene has 5% absorbance around 500 nm [172] and the nominal absorbance of the fused silica plate is 7% absorbance at 500 nm, the graphene plate has 12% absorbance.

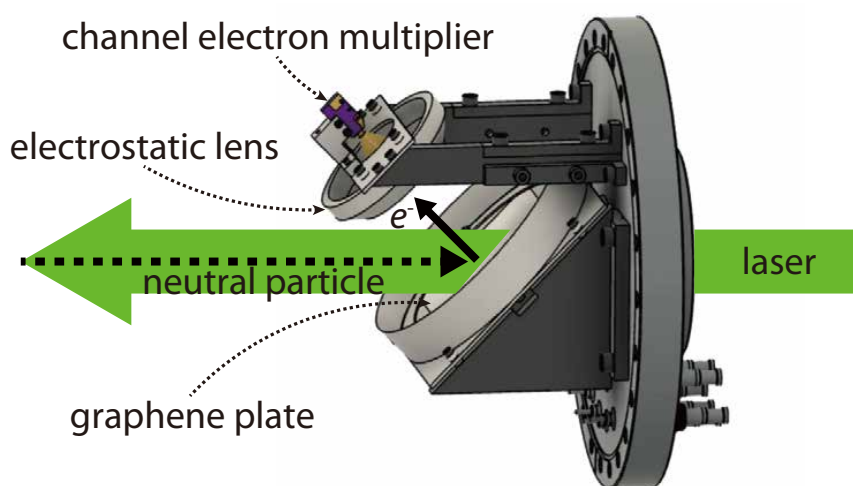


Figure 2.10: The schematics of the neutral particle detector

The typical dark count rate of the CEM is below 0.02 cps, and the typical transit time is 26 ns when the back voltage of the CEM is 2.3 kV. In this experiment, -500 V was applied to the graphene plate, -1300 V to the lens, 0 V to the front of the CEM, and 2300 V to the back of the CEM. The output (anode) of the CEM was high-pass filtered as shown in Fig. 2.12, amplified by a preamplifier (ORTEC VT120), and then discriminated and counted using a time-to-digital Converter (TDC) (Signadyne SD-PXE-TDC-H0003). The discrimination threshold was set to be -0.02 V at falling edge for stop signal and 0.20 V at rising edge for start signal. The TDC can time tag multiple stop signals for a single start signal. Since the nominal maximum pulse rate is 150 MPulses/s, and the detectable signal interval is 7 ns if the signals are always input at the same interval.

The start signal employed a signal from the trigger of the Nd:YAG laser for OPO, delayed by a delay generator (Stanford Research Systems DG645). The delay time was adjusted using a silicon photo detector (Electro-Optics Technology ET-2030) at



Figure 2.11: The graphene plate, which was fabricated by transcription of two 75 × 75 mm graphene sheets to 85 × 85 mm $t = 2.0$ fused silica plate.

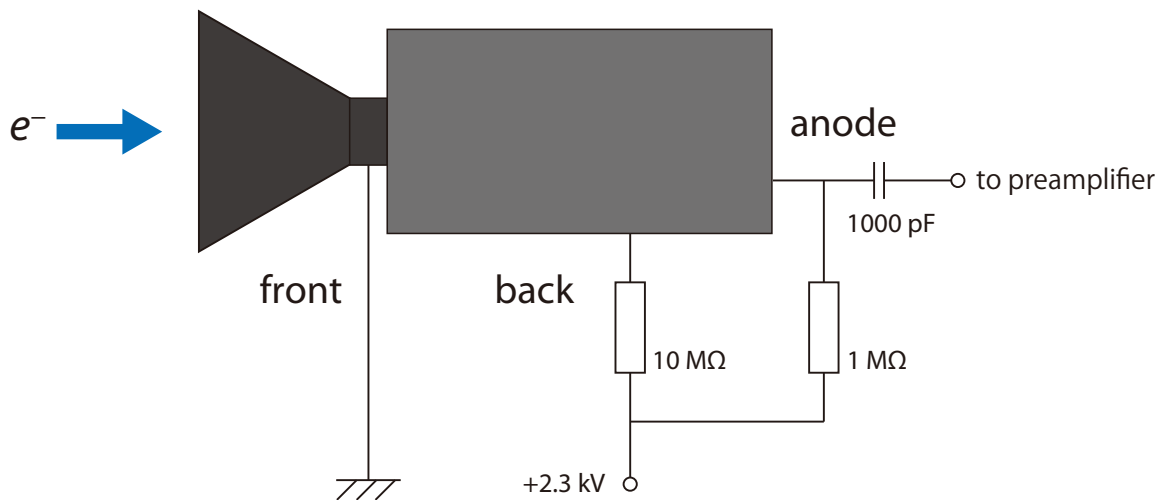


Figure 2.12: Voltage application circuit to CEM and high pass filter.

the window of the neutral particle detector to match the timing. The delay time set was 292.605 μs .

The substrate emitting the secondary electrons can be a metal mirror instead of a graphene plate. The neutral particle detector with a metal mirror reflects the laser, while the neutral particle detector with a graphene plate transmits the laser. Fig. 2.13 shows the counts when only the laser is injected without any ions or neutral particles into the detector with an aluminum mirror. There are signals emitted when the laser is just injected and signals after the laser insertion. Since the neutral particles (the beam energy is 5 keV) emitted from the RICE do not reach the neutral particle detector until after 7 μs from the laser incidence, the signals emitted when the laser

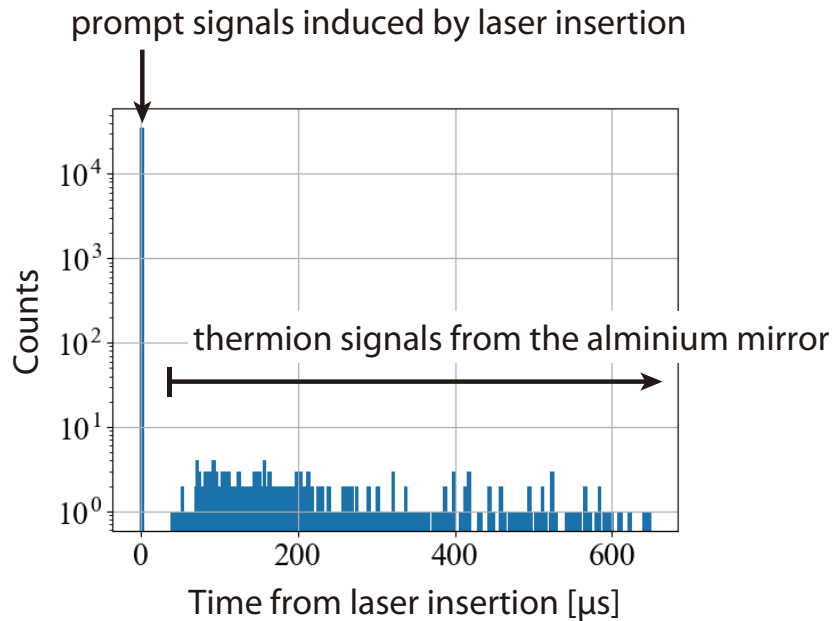


Figure 2.13: The typical signal count of the neutral particle detector utilizing aluminum mirror [174] with laser insertion and no ion and neutral particle. The wavelength was 400 nm and the laser pulse energy was 200 μJ (1.0×10^{-2} mJ/cm² in energy density).

is just injected can be ignored. The signals after the laser insertion are an obstacle for counting. The neutral particle detector with a graphene plate produces less than 0.01 counts per laser shot by 541 nm laser, making it more suitable for this experiment than one with an aluminum mirror. The absorption rate at around 500 nm is about 8% for aluminum [173], compared to about 12% for the graphene plate as mentioned above. Thus, the emission of thermal electrons due to photoabsorption is not a reason. There are two expected reasons why the neutral particle detector with a graphene plate has a few signals after the laser insertion. First, graphene is less susceptible to surface oxidation than aluminum. Secondly, the graphene plate has less roughness than the aluminum mirror and less molecular adsorption, which is delayed release by visible lasers.

Chapter 3

Result and discussion

3.1 Counting detached neutral particles without laser

The C_2^- beam was stored in the RICE, and the number of neutral particles ejected from port 2 was counted with the neutral particle detector. Fig. 3.1 shows a histogram of the number of detected neutral particles with a bin size of 167.772 μs . The number of ion beam injections is 3048000, and the measurement took 84 hours 40 minutes. The obtained decay time was 2.905 ± 0.011 ms. Pedersen *et al.* [46] reported the decay time of 2.5 ms, Naaman *et al.* [49] a few ms, Takao *et al.* [47] 3 ms, and Kono *et al.* (conference poster) [48] a few ms. The decay time obtained here is in good agreement with those previous studies.

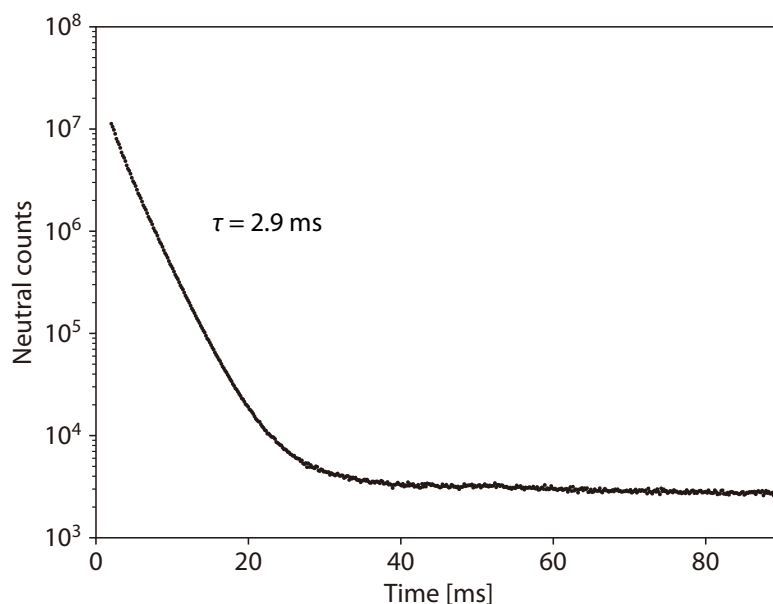


Figure3.1: The histogram of the number of detected neutral particles ejected from port 2 of RICE. This figure is quoted from Iizawa *et al.* [159] under the CC BY 4.0 license.

Pedersen *et al.* [46] pointed out that it could be a component of a quartet state, for example, $^4\Sigma_u^+$, due to autodetachment, but theoretical calculations by Halmová *et*

al. [53] suggested there are no bound quadruplet states. In another possibility, this component is due to the high vibration state of the X state. Since the A and B states relax on the time scale of μ s and ns as shown in table 1.9, respectively, they are not the cause of the component.

3.2 Laser-induced photodetachment spectroscopy: the $B-X$ transition

The transition spectrum between B and X (HL band) was then measured for $Xv'' \geq 6$, $Bv' \geq 5$ after 10 ms storage. By identifying the largest vibrational level of X at which the transition spectrum is observed, we can restrict the peaks that can be explained by the transitions between X , A , and B .

Under the laser pulse energy condition of 1 mJ (5.1×10^{-2} mJ/cm²) at a storage time of 10 ms, we measured photodetachment spectra over a wide range of wavenumbers from 17608 to 18588 cm⁻¹, where the $B-X$ $\Delta v = -1$ transitions of $v' = 5-8$ are included. We selected the condition of 10 ms storage time because the autodetachment component, which is regarded to be the background against photodetachment, is sufficiently suppressed to observe $B-X$ transition. According to the theoretical calculations by Rosmus *et al.* [138], the lifetime of $X v'' = 6-10$ is several tens of ms. Then the peaks oriented from $X v'' = 6-10$ can be observed even after 10 ms if the X state is produced by the ion source. Also in Iida *et al.* [145], $X v'' = 6, 7$ has been observed even after tens of ms storage.

Fig. 3.2 shows the number of counts obtained with the neutral detector. The number of neutral particles was counted only during the time window in which the neutral particle arrived from the straight section of ports 1-2. Since a 5keV carbon dimer ($m=24$) reaches the detector at 7.2-11.1 μ s after laser insertion, the region of interest (ROI) was set to 7.2-11.1 μ s.

We performed this measurement by changing the laser wavenumber, and the obtained spectrum is shown in Fig. 3.3. The ion beam was injected 50 times per point (5 s) and the step was 0.001 nm (0.03 cm⁻¹). The total measurement time was about 43 hours. Since the number of incident ions and their angular spread vary depending on the condition of the ion source, the spectrum has to be normalized for each shot by the number of accumulated ions after a certain storage time. The number of accumulated ions is proportional to the number of the detached neutral particles at the same time, and then we normalized by the sum of the number of neutrals from 500 to 1298 μ s.

In obtained wavenumber range, $\Delta v = -1$ spectra were seen. Then we used the spectral simulation program PGOPHER to make spectral assignments for $\Delta v = -1$. The spectral constants of the X states are referenced to Jones *et al.* [85]. We found that the maximum observable vibrational level of X state is $v'' = 9$, and no more vibrational states can be observed.

The intensity of the band head of $X v'' = 6 \rightarrow B v' = 5$ is weaker than that of other transition bands ($X v'' = 7 \rightarrow B v' = 6$, $X v'' = 8 \rightarrow B v' = 7$, $X v'' = 9 \rightarrow B v' = 8$), which was already reported by Jones *et al.* [85]. This is due to the competing radiative

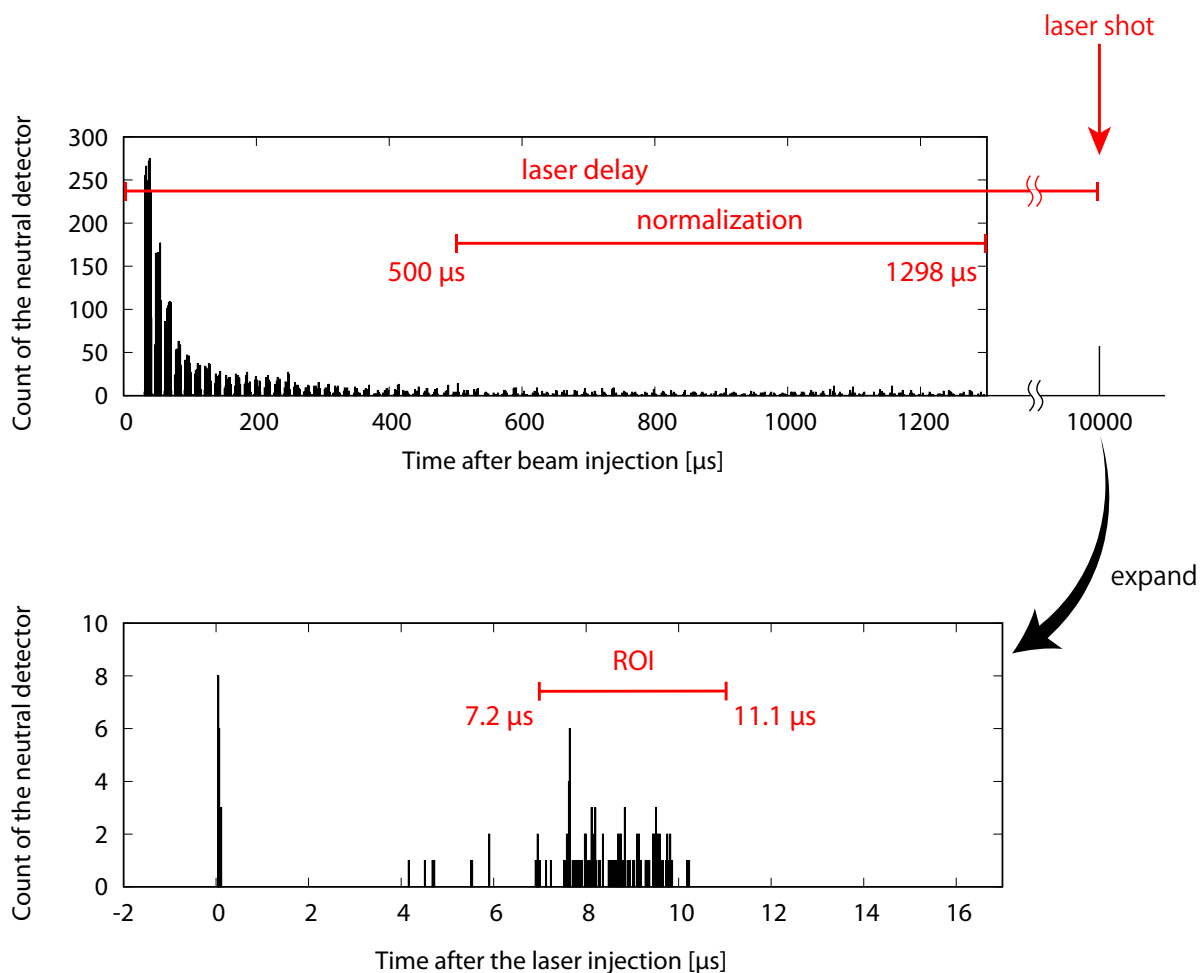


Figure 3.2: The typical count of the neutral particle detector.

decay back to the X state.

Furthermore, a number of peaks were observed that cannot be assigned with $B-X \Delta v = -1$. These peaks are discussed in detail in the next section.

Table 3.1 and Fig. 3.4 shows the obtained spectral constants of B . Although the obtained constants are not directly relevant to future discussions, the rotational constants obtained in this study are an improvement in accuracy over previous studies, and they will serve as a benchmark for future quantum chemical calculations.

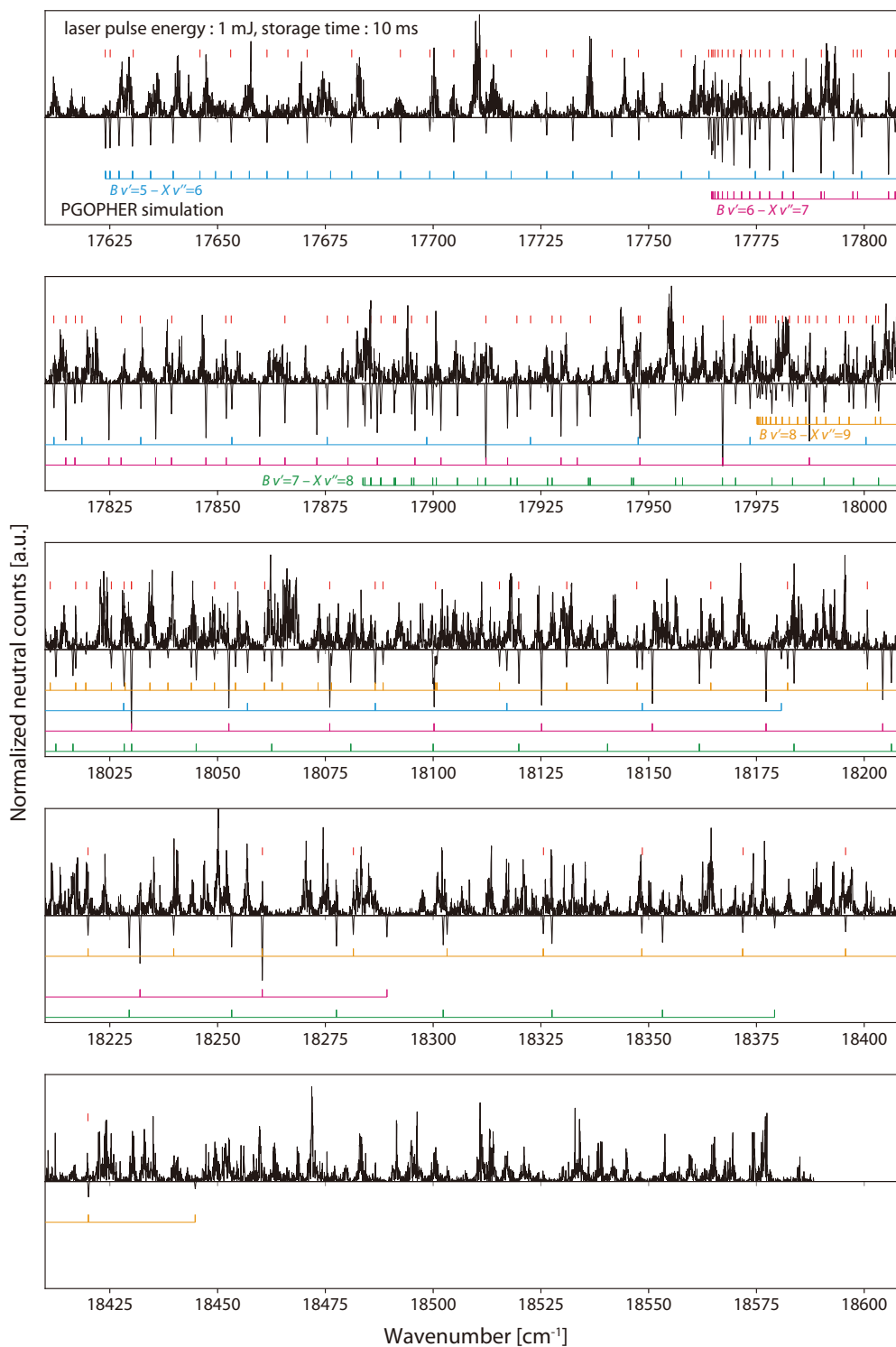


Figure 3.3: Laser-induced photodetachment spectra at 10 ms storage with a laser pulse energy of 1 mJ. Wavenumber increment was set to 0.03 cm^{-1} steps. The spectral simulation by PGOPHER is also shown for $B-X$ ($\Delta v = v' - v'' = -1$) transitions for $v' = 5-8$ assuming a molecular temperature of 5000 K. The spectral constants for the B state were fitted to the line positions of experimental spectra. The marks on the experimental spectrum indicate the peaks used for the fitting. See text for the details of the simulation and fitting. This figure is quoted from Iizawa *et al.* [159] under the CC BY 4.0 license.

Table3.1: The spectroscopic constants for the highly excited vibrational levels based on the assignments shown in Fig. 3.3. The term values T_e of the vibrational levels of the $X^2\Sigma_g^+$ and $B^2\Sigma_u^+$ states were taken from the paper by Nakajima [122], which is complementary to the works of Jones *et al.* [85] and Mead *et al.* [99]. The constants of the electronic ground state $X^2\Sigma_g^+$ were adopted from the paper by Jones *et al.* [85]. The values in parentheses indicate 1σ uncertainty. The rotational constant B_v and the centrifugal distortion constant D_v of $B v' = 8$ obtained by applying $\Delta v = -1$ transition peaks have not been previously reported. The appendix in the paper by Mead *et al.* [99] reports the spectroscopic constants of $B v' = 8$ obtained with $\Delta v = -2$.

Vibrational quantum number of $B^2\Sigma_u^+$	Rotational constant B_v		
	This work ($\Delta v = -1$)	Jones <i>et al.</i> [85] ($\Delta v = -1$)	Mead <i>et al.</i> [99] ($\Delta v = -2$)
5	1.768481(22)	1.76808(63)	1.767953(62)
6	1.745290(47)	1.74488(61)	1.744358(75)
7	1.722835(36)	1.72108(76)	1.719350(75)
8	1.692944(21)	N/A	1.69240(14)

Vibrational quantum number of $B^2\Sigma_u^+$	Centrifugal distortion constant D_v		
	This work ($\Delta v = -1$)	Jones <i>et al.</i> [85] ($\Delta v = -1$)	Mead <i>et al.</i> [99] ($\Delta v = -2$)
5	$7.876(12) \times 10^{-6}$	$7.61(49) \times 10^{-6}$	$7.5013(85) \times 10^{-6}$
6	$9.179(47) \times 10^{-6}$	$9.01(45) \times 10^{-6}$	$7.790(20) \times 10^{-6}$
7	$1.0929(22) \times 10^{-5}$	$9.66(61) \times 10^{-6}$	$8.259(29) \times 10^{-6}$
8	$1.0036(11) \times 10^{-5}$	N/A	$9.002(57) \times 10^{-6}$

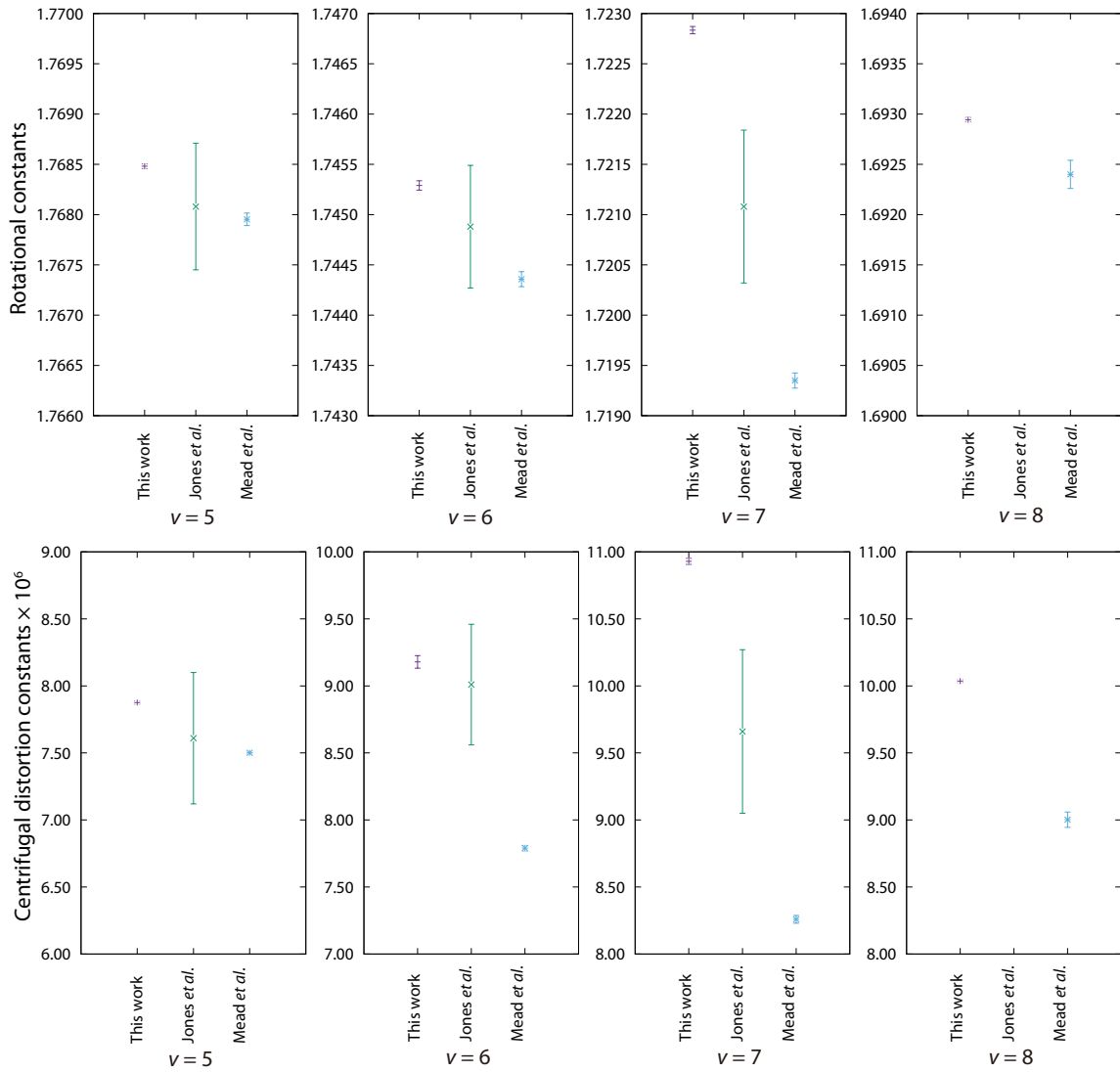


Figure 3.4: The bar plots of the rotational constants and centrifugal distortion constant of B. The error bars indicate 1σ uncertainty.

3.3 Laser-induced photodetachment spectroscopy and temporal evolution: the unassigned transitions

In the previous section, we noted that a number of peaks were observed, and they could not be explained by $B-X \Delta v = -1$. Hence we obtained time-resolved photodetachment spectra and determined the lifetimes of these peaks.

Only for the spectrum with a storage time of 0.1 ms we subtracted the counts of neutrals not attributable to the photodetachment. Fig. 3.5 shows the counts of neutral particles detected by the neutral particle detector when the laser was injected with a storage time of 0.1 ms. The count in the ROI includes the count of neutral particles that are not caused by the laser. Hence, the counts in the ROI were subtracted by the averaged counts in the portion of the ion beam bunch width of $10 \mu\text{s}$, excluding the $0.4 \mu\text{s}$ at the rising and falling edges and the ROI.

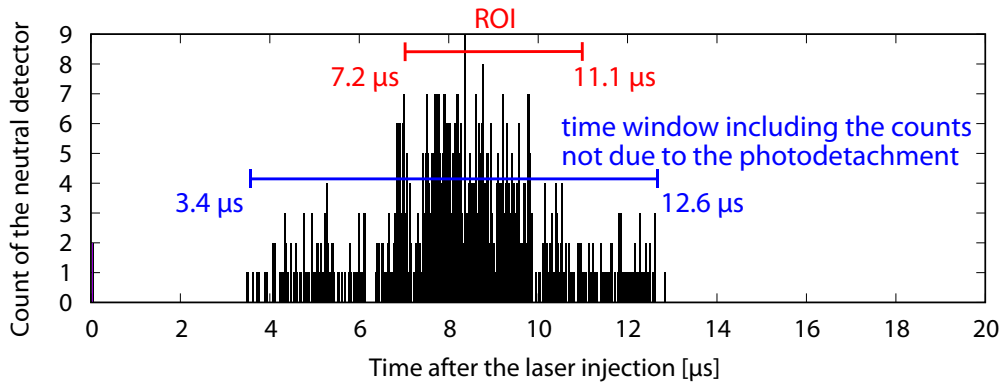


Figure 3.5: The typical raw count of the neutral particle detector at the storage time of 0.1 ms.

Fig. 3.6 (a) shows the obtained time-resolved photodetachment spectrum. The measured wavenumber range is from $18\,448$ to $18\,567 \text{ cm}^{-1}$. There is no $B-X \Delta v = -1$ transition peak in this range, as described in the previous section. The storage time was changed by laser delay, and spectra were obtained for accumulation times of 0.1, 1, 2, 3, 4, 10, 20, 40, and 80 ms. The number of ion beam injections per point was 30 injections (0.1, 1 ms), 50 injections (2–20 ms), 150 injections (40 ms), and 600 injections (80 ms). The total measurement time was about 106 hours. Fig. 3.6 (b) shows the spectrum of $B v' = 0-X v'' = 0$, the only $B-X$ transition in this wavenumber range with a laser pulse energy of 5 mJ. Simulations were performed in `PGOPHER` using Jones *et al.*'s spectral constants [85]. These peaks are not observed in the spectrum (a) measured at 1 mJ because this process is a two-photon process, as shown in Fig. 2.2, and requires a large laser pulse energy.

A number of the peaks seen at 0.1 and 1 ms in Fig. 3.6 (a) disappear after 2–3 ms storage time. On the other hand, some peaks remain until 80 ms. If these peaks are derived are $B-X$ or $A-X$ transitions, there are three possibilities in this wavenumber

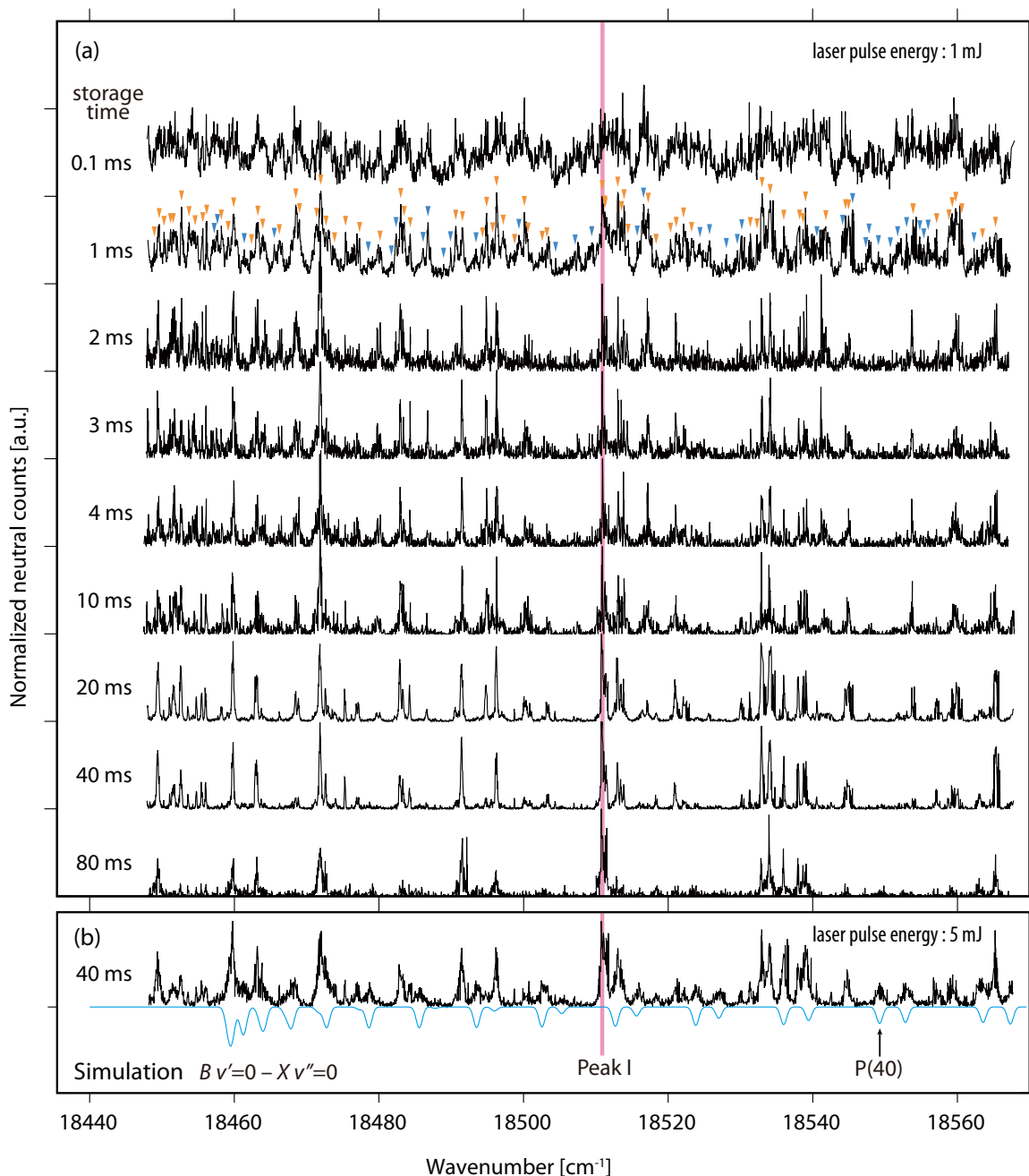


Figure 3.6: (a) The laser-induced photodetachment spectra of C_2^- from 18448 to 18567 cm^{-1} at 1 mJ. The spectra were measured at storage times of 0.1, 1, 2, 3, 4, 10, 20, 40, and 80 ms. Wavenumber increment is set to 0.03 cm^{-1} steps. For the peaks with triangular marks, the decay time constant of the peak intensity was analyzed. The resulting time constant of each peak is shown by the color of the triangles: orange (> 3.0 ms) and blue (< 3.0 ms). All spectra were normalized to the intensity of Peak I. (b) The same spectrum at 40 ms, but with a laser pulse energy of 5 mJ. The lower blue line shows the PGOPHER simulation of the $X^2\Sigma_g^+(v''=0) \rightarrow B^2\Sigma_u^+(v'=0)$ transitions.

range. The first is $B-X$ $\Delta v = -1$ ($v' > 9$). This possibility is rejected by the analysis performed in the previous section. The second possibility is $B-X$ ($X v'' \leq 5$), but as mentioned above, this is a two-photon process, and we know that it is observed when measured at 5 mJ but not when measured at 1 mJ. Therefore, it is rejected. The third is the $A-X$ transition. The energy level of $A v' > 15$ is above the detachment threshold and would be photodetached. In this wavenumber range, there are transitions of $\Delta v = 11$, such as $A v' = 16-X v'' = 5$. However, the Franck-Condon factor is very small ($< 10^{-4}$). Then this possibility is also rejected.

In addition, as shown in table 1.9, it is theoretically derived that the A state relaxes in the μs order and the B state in the ns order; then, these peaks cannot be attributed to the transitions from the A and B states. Furthermore, transitions such as those discussed above have not been observed in the previous experiments in this wavenumber range. Then, these peaks cannot be explained by the transitions between X , A , and B (doublet-doublet transitions). Therefore, it is reasonable to assume that they originate from bound electronic states other than X , A , and B .

3.4 Normalization for spectra of each storage time

In order to quantitatively compare the spectra measured at different storage times, it is necessary to normalize each spectrum by the number of ions in the ring at the time of laser irradiation.

Let $N_X(t)$ be the number of ion in the X state at the time t and S be the set of the vibrational states of the each electronic state other than X , i.e., $S = \{A v = 0, A v = 1, \dots, B v = 1, B v = 2, \dots, {}^4\Sigma_u^+ v = 0, \dots\}$. For any $i \in S$, $N_i(t)$ is defined as the number of ions in the i state at the time t . For example, $N_{Bv=2}(t)$ means the number of ions in the $B v = 2$ state at the time t . The respective peak height $h_{ij}(t)$ ($i, j \in S$) in the phoyodetachment spectrum resulting from an optical transition from state i to state j can be written as a constant multiple of $N_i(t)$, that is

$$h_{ij}(t) = c_{ij}N_i(t) \quad (3.1)$$

where c_{ij} is a constant. $N_i(t)$ decreases due to autodetachment or due to collisions with residual gas and fall out of the storage ring. The former is an exponential decrease with a lifetime τ_i unique to each state, while the latter is a state-independent but time-dependent decrease $\lambda(t)$. $N_X(t)$ is only decreased by the latter, then

$$\frac{dN_i(t)}{dt} = -\frac{1}{\tau_i}N_i(t) - \lambda(t)N_i(t) \quad (3.2)$$

$$\frac{dN_X(t)}{dt} = -\lambda(t)N_X(t). \quad (3.3)$$

Solving this, we find that

$$N_i(t) = N_i(0) \exp\left(-\frac{t}{\tau_i} - \int_1^t \lambda(\xi)d\xi\right) \quad (3.4)$$

$$N_X(t) = N_X(0) \exp\left(-\int_1^t \lambda(\xi)d\xi\right). \quad (3.5)$$

Since we want to find τ_i , the height $h_{ij}(t)$ of each peak in the detachment spectrum should be normalized by the amount of ions in the $X^2\Sigma_g^+$ state, $N_X(t)$, as in

$$\frac{h_{ij}(t)}{N_X(t)} = \frac{c_{ij}N_i(0)}{N_X(0)} \exp\left(-\frac{t}{\tau_i}\right), \quad (3.6)$$

instead of the total amount of ions, $N_{\text{tot}}(t) = \sum_i N_i(t) + N_X(t)$.

The time evolution of the ratio of the number of ion in each vibrational state of $X^2\Sigma_g^+$ to the sum of the ion abundances of the doublet states $X^2\Sigma_g^+$ and $A^2\Pi_u$ is shown in Fig. 3.7. The A coefficient of each vibrational state was derived using the program LEVEL [78], which finds the Frank-Condon coefficient by solving the Schrödinger equation in the radial direction. It was calculated by solving the rate equation with the initial temperature as 4500 K and the vibration state under calculation as $X^2\Sigma_g^+ v = 0-10$, $A^2\Pi_u v = 0-10$. Transitions from the quartet states to the doublet states are not considered because they are forbidden. In addition, since $A^2\Pi_u$ and $B^2\Sigma_u^+$ relax immediately, the number of the $X^2\Sigma_g^+$ states can be regarded as the total number of the doublet state. The change of relative population during the storage time at 0.1–80 ms is less than 4%, which is small enough to be regarded as constant in the present study. Therefore, the height of the detachment peak from $X^2\Sigma_g^+ v'' = 0$ through $B^2\Sigma_u^+ v' = 0$ is proportional to the total number of ions in the doublet states. Therefore, by normalizing $h_{ij}(t)$ using the peak height of $v'' = 0 \rightarrow v' = 0$, it is possible to determine τ_i .

For this normalization, we observed the resonance-enhanced two-photon detachment (REMPED) of the $X^2\Sigma_g^+ v = 0$ state with an increased laser pulse energy at 5 mJ (2.5×10^{-1} mJ/cm²). Fig. 3.6 (b) shows the photodetachment spectrum at 40 ms obtained with a laser pulse energy of 5 mJ, exhibiting additional peak structures that were not present at a pulse energy of 1 mJ. The positions of additional peaks agreed well with the spectral simulation for the $X v'' = 0 \rightarrow B v' = 0$ transition obtained by PGOPHER assuming a typical initial temperature for a cesium-sputter ion source (5000 K) [175]. Although these peaks are suitable in principle for normalization, the spectrum at 5 mJ is more complicated due to the two-photon processes and power broadening. For this reason, we paid attention to a peak at 18511 cm⁻¹, hereafter called Peak I, which is intense even after 80 ms of storage time. At the laser pulse energy of 5 mJ, we compared its peak intensities relative to the ro-vibrationally well-resolved transition of P(40) (the transition peak of the P branch ($\Delta J = -1$) whose initial rotational quantum number is 40) at 18549 cm⁻¹ among the $X v'' = 0 \rightarrow B v' = 0$ transitions, and found a near-constant intensity ratio of 2.9 ± 0.3 over the range of 20–80 ms as illustrated in Fig. 3.8. Assuming that this behavior also holds for storage times earlier than 20 ms, we were able to use Peak I to normalize each spectrum at the laser pulse energy of 1 mJ instead of the P(40) transition originating from the ground state X .

Here we describe additional information on the laser pulse energy dependence of the spectra. We measured the laser pulse energy dependence of Peak I and peak P(40). As shown in Fig. 3.9, the intensities of Peak I saturate with weak laser pulse energies less than 1 mJ. This explains our observation that the intensity of Peak I at

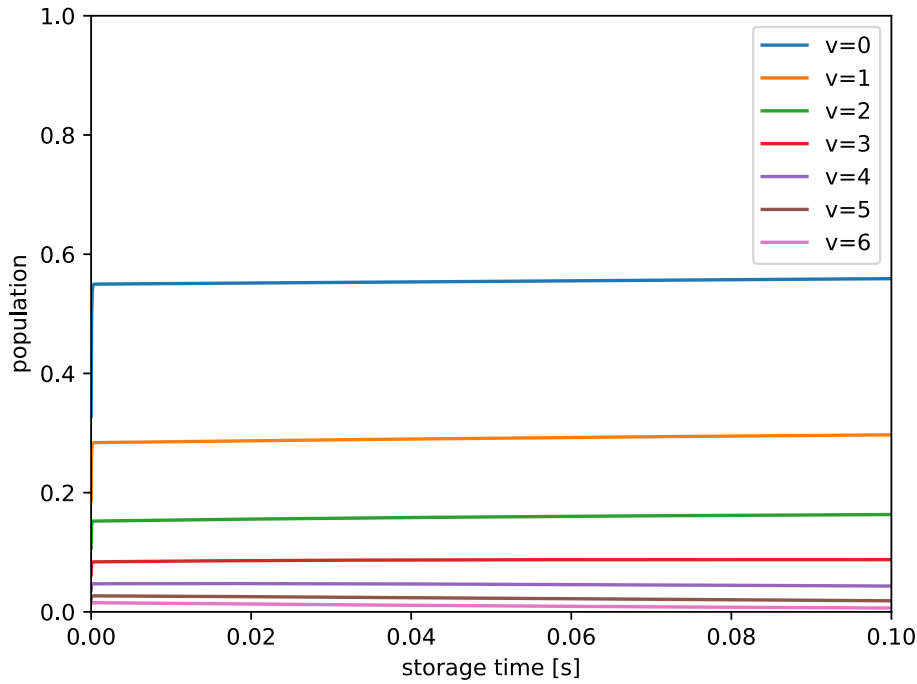


Figure 3.7: Simulation of the time evolution of the population of the doublet state. The vertical axis shows the ratio of the population of each vibrational state of the $X \ ^2\Sigma_g^+$ state to the total population of the doublet state.

40 ms is comparable at both 1 and 5 mJ pulse energies. This feature is also seen in the other unassigned peaks. Therefore, every unassigned peak in the spectra of 1 and 5 mJ at 40 ms in Fig. 3.6 is considered to be saturated. It implies that they result from a one-photon process if we assume a typical cross-section for allowed bound-bound transitions. In contrast, the peak P(40) belonging to the $B-X$ transition is observable in the spectrum at a laser pulse energy of 5 mJ but not at 1 mJ, as already described. Their intensities are linearly correlated with the laser pulse energy, as shown in Fig. 3.9. Lineberger and Patterson [120] explained that the transition from $X \ v'' = 0$ to $B \ v' = 0$ is readily saturated, and the transition probabilities from bound to continuum states $C_2^-(B \ v' = 0) \rightarrow C_2(X)$ are linearly correlated.

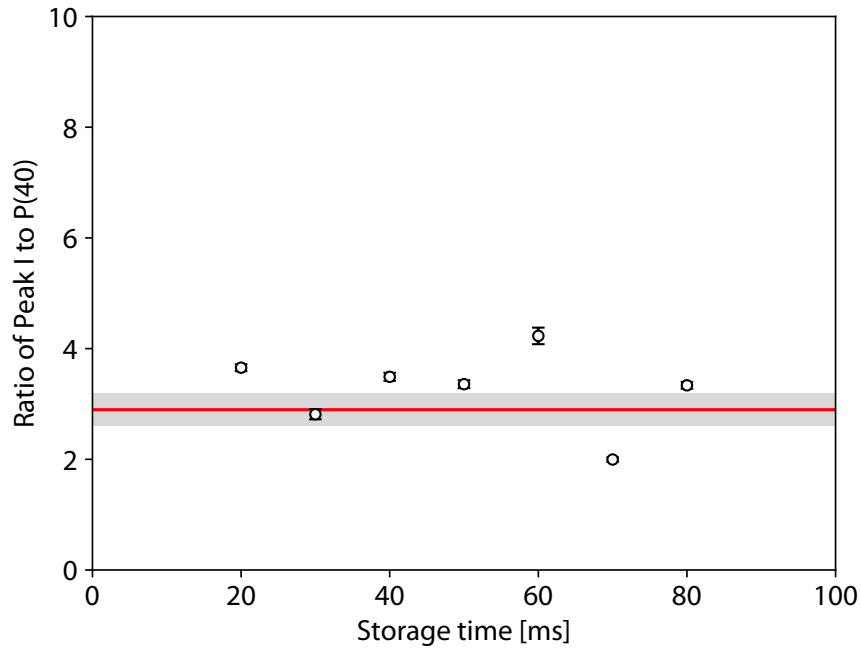


Figure3.8: The intensity ratio of Peak I and $X v'' = 0 \rightarrow B v' = 0 P(40)$ as a function of storage time. The red straight line is the average weighted by the error bar of each ratio. The gray-filled area shows the standard deviation of the average. This figure is quoted from Iizawa *et al.* [159] under the CC BY 4.0 license.

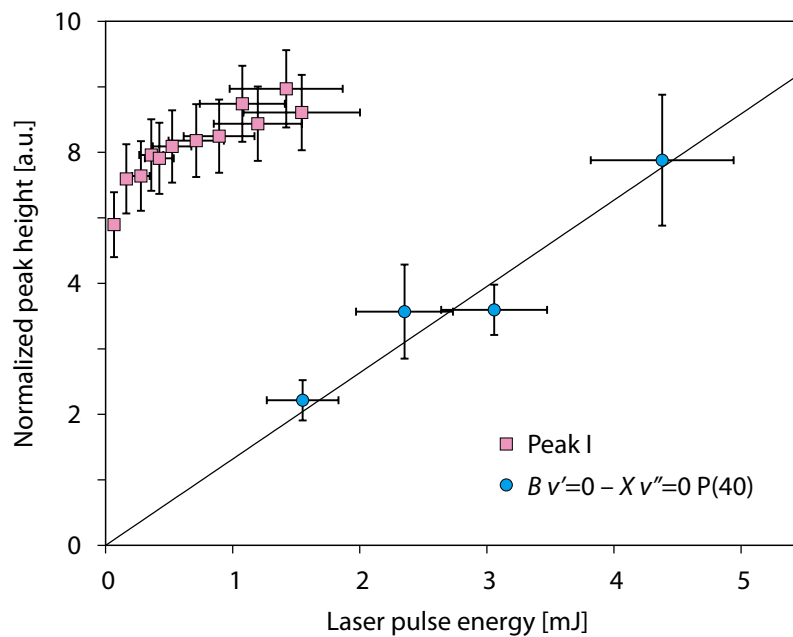


Figure3.9: Laser pulse energy dependence of the intensities of Peak I observed at a storage time of 20 ms (blue circle) and that of P(40) in $X v'' = 0 \rightarrow B v' = 0$ at a storage time of 40 ms (pink square). The straight line shows a linear fitting of P(40). This figure is quoted from Iizawa *et al.* [159] under the CC BY 4.0 license.

3.5 Lifetime analysis of the unassigned peaks

The normalization described in the previous section was performed, and the decay times of the 110 unidentified peaks were determined from the photodetachment spectra shown in Fig. 3.6(a). These peaks were selected that we recognize as peaks in the 1 ms spectrum that could also be confirmed in the 2 ms spectrum. The peaks for which lifetimes were determined are indicated by ▼ in the 1 ms spectra in Fig. 3.6(a). The heights of these peaks were determined for each storage time from 0.1 to 80 ms, and the decay times were obtained by curve fitting with a single-exponential function $f(t) = -N_0 \exp(-t/\tau) + a$. Assume a 30% uncertainty in peak height to account for the stability of the population of each vibrational and rotational state in the ion beam during the measurement time of several months. Introducing this uncertainty contributes a more accurate evaluation of the χ^2 and confidence interval but does not change the trend of the obtained time constant distribution.

The peaks were classified into long-lived and short-lived ones, and background settings were adjusted for each class. When the arithmetic mean of the peak heights at 40 and 80 ms is greater than 1/10 of the peak height at 0.1 ms, this peak was classified as a long-lived peak. If the 40 or 80 ms peak was not used for fitting, the peak height of the longest storage time was used as the reference. The other peaks were classified as short-lived peaks. Note that the 36th peak from the left in Fig. 3.6 is judged as a long-lived peak, but the peak is just picked up by the shoulder of the neighboring peak and makes the peak appear higher. Then the 36th peak was manually classified as a short-lived peak. The background a was changed depending on whether it is a long-lived or short-lived peak. For the short-lived peak, the peak height with a long storage time has decayed sufficiently, and the height is regarded as the background. Then the background a is defined as the arithmetic mean of the peak heights at 40 and 80 ms. If the 40 or 80 ms peak was not used for fitting, the background a is defined as the peak height of the longest storage time. For the long-lived peak, the background cannot be obtained from the peak heights, and then the background is defined as the integral over the wavenumber band of the 10, 20, 40, and 80 ms spectra in which no peak appears (gray part of fig. 3.10).

There are long-lived peaks whose height decays rapidly at 0.1 ms and 1 ms even though the peak height is large enough at 40 and 80 ms to be judged as a long-lived peak. In this case, 0.1 ms and 1 ms data were not used for fitting. On the spectra, there are some peaks whose height is unstable or takes a strange behavior such that suddenly peaks appear or grow. In this case, the corresponding data were not used for the fitting. The fitting results are shown in fig. 3.13. The data not used for fitting is indicated by gray color. The chi-square for each peak is shown in Fig. 3.12. There are many peaks with reduced chi-square $\chi^2/(\text{degree of freedom}) \ll 1$, but this is mainly due to the small sample size and not considered an incorrect choice of model.

The obtained lifetime for each peak is shown in Fig. 3.11. Peaks with lifetimes longer than 10 s are removed from the plot. The error bars are 95% confidence interval. Since the maximum storage time of the spectrum acquired in this study is 80 ms, peaks with lifetimes longer than around 100 ms have large error bars.

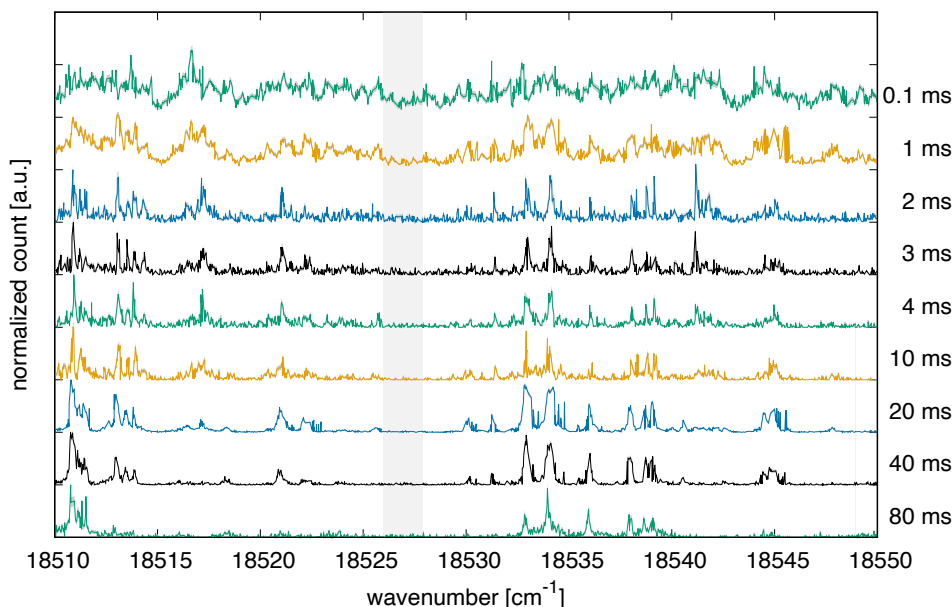


Figure 3.10: The wavenumber bands used to derive background for short-lived peak (gray part). The band of the spectrum from 10–80 ms in which the short-lived component is sufficiently decayed was selected.

The results show that the peaks can be roughly divided into two groups: peaks with lifetimes of 1.5–3.0 ms and those with longer lifetimes, and there is more scatter in the latter group. The former lifetime is in good agreement with the autodetachment lifetimes observed without laser irradiation as discussed in § 3.1. It is clear from the previous discussion that these peaks with lifetimes of 1.5–3.0 ms are not doublet–doublet transition peaks. Therefore, the initial states of the transitions from which these peaks originate are responsible for autodetachment.

We also found that there are peaks with lifetimes longer than 100 ms. Since these are also not doublet–doublet transition peaks, the long-lived states other than the ground state $X^2\Sigma_g^+$ that exceed 100 ms exist. This suggests the possibility of the existence of bound excited states other than the $X^2\Sigma_g^+$, $A^2\Pi_u$, and $B^2\Sigma_u^+$ states.

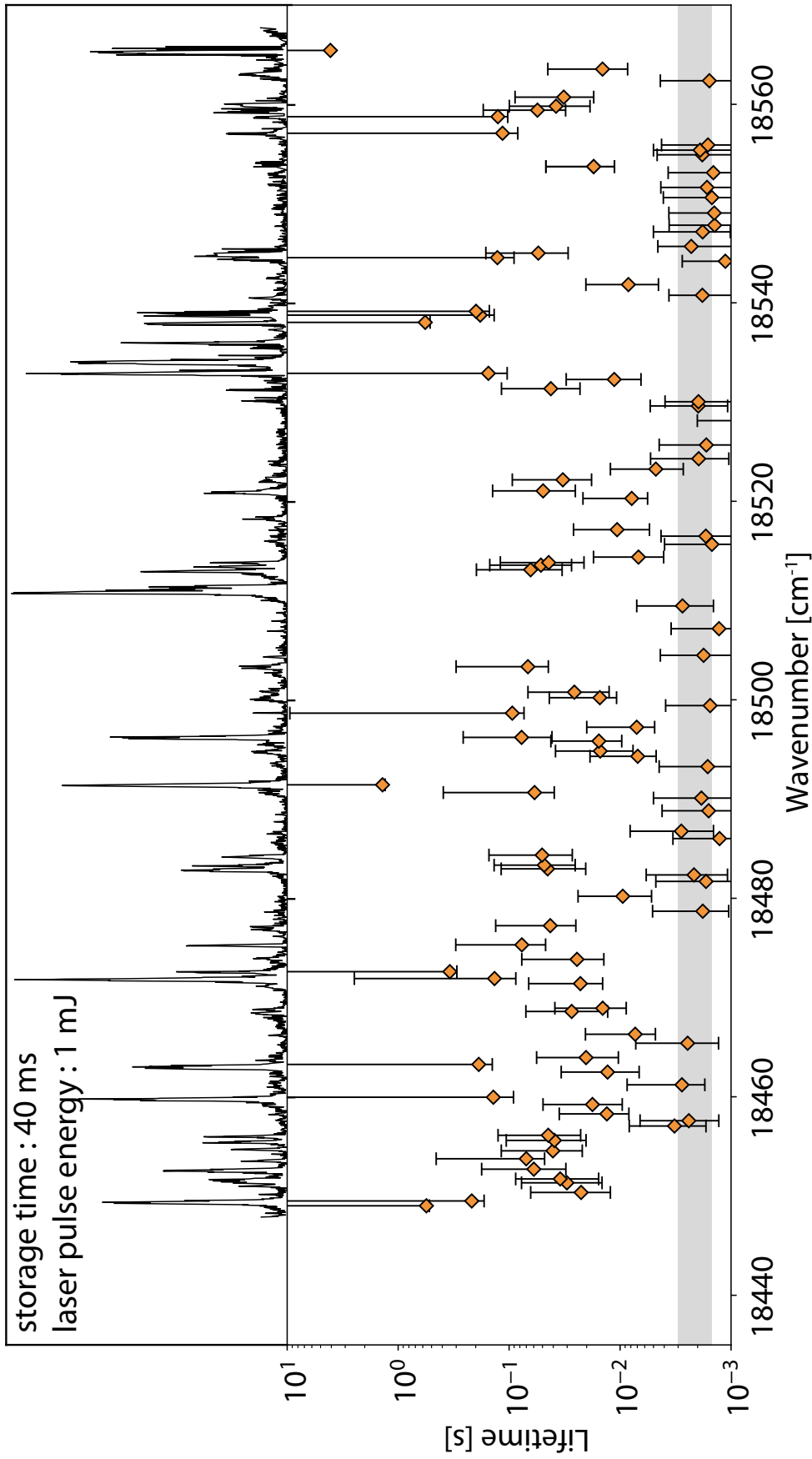


Figure 3.11: The lifetimes of the unassigned peaks specified by orange triangles \blacktriangledown in Fig. 3.6. We excluded points with a lifetime longer than 10 s due to ambiguities. Considerable ambiguities of the lifetimes longer than 10^{-1} s reflect the experimental condition that the ion storage times before laser irradiation were limited up to 80 ms. The gray region corresponds to the lifetimes of 1.5–3.0 ms.

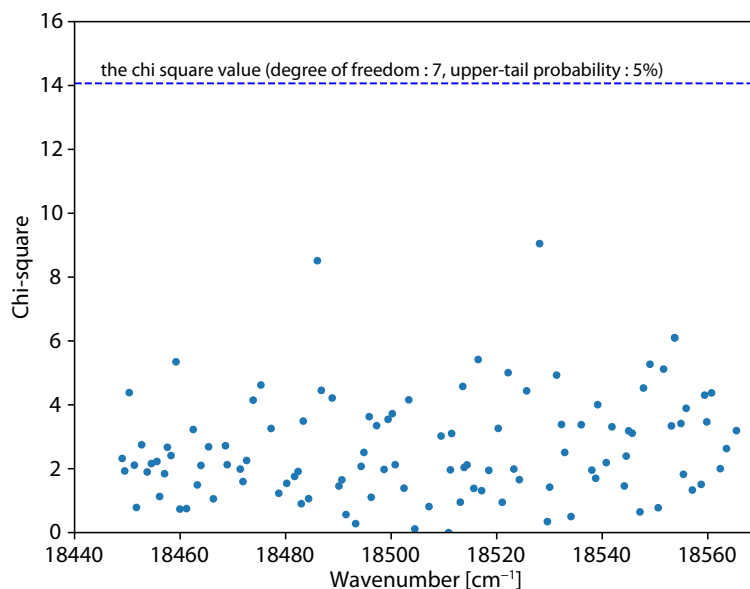
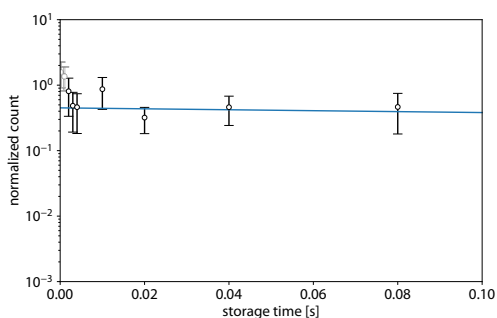


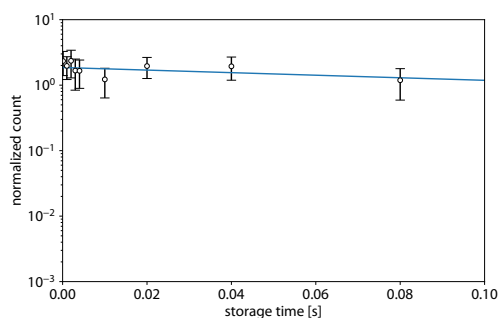
Figure 3.12: The chi-square for each peak. Because of small sample size, the reduced chi-square $\chi^2/(\text{degree of freedom})$ tends to be smaller than 1.

As noted in § 1.2.6, Pedersen *et al.* [46] observed an autodetaching component with a lifetime of 2.5 ms and proposed that the transition is due to $^4\Sigma_u^+$. Transitions from these states to the electronic ground state $X^1\Sigma_g^+$ of the neutral C_2 are forbidden and thus are expected to have long lifetimes on the time scale of ms. In addition, as shown in the potential energy curve (Fig. 1.10), the position of the potential minimum of $^4\Sigma_u^+$ is significantly shifted from that of $a^3\Pi_u$ in C_2 . Therefore, even if $^4\Sigma_u^+$ relaxes to $a^3\Pi_u$ in C_2 , it is not at all strange that a possible $^4\Sigma_u^+$ state has a long lifetime due to the small overlap of their wavefunctions. Moreover, the transitions from $^4\Sigma_u^+$ to $X^2\Sigma_g^+$, $A^2\Pi_u$, and $B^2\Sigma_u^+$ are spin forbidden as described so far, and the overlap of the wavefunctions is also tiny, then the transition probabilities have to be extremely small.

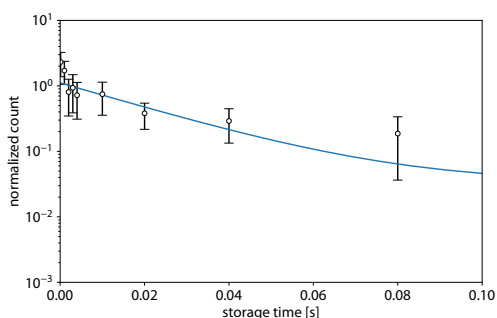
If these peaks are optical transitions from the $^4\Sigma_u^+$ state, another higher quartet state decaying to neutral C_2 is required. Indeed, the laser power dependence measurements shown in Fig. 3.6 (a) and (b) indicate that most of the long-lived unidentified peaks originate from bound-bound transitions. Although only $^4\Sigma_u^+$ and $^4\Delta_u$ are plotted in Fig. 1.10, the upper quartet states $^4\Sigma_g^+$ and $^4\Pi_g$ of the allowed transitions have also been calculated. These overlaps are generally significant. A possible curve crossing mechanism between a quartet state, produced after laser excitation, and the $a^3\Pi_u$ state of C_2 may also contribute to neutralization via purely electronic autodetachment [113]. The assignment of these peaks requires precise information about the potential curves of these highly excited electronic states and associated vibrational levels.



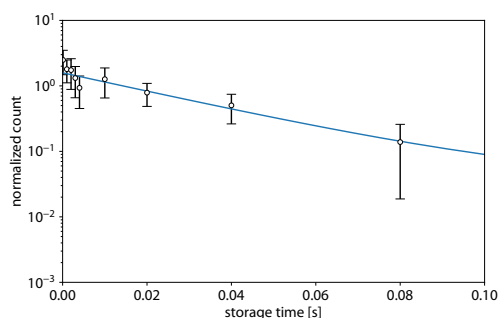
the 0th peak from the left in figure 3.6



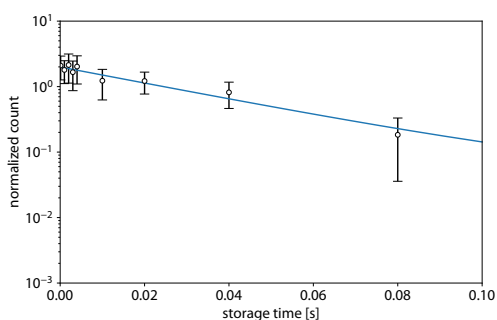
the 1st peak from the left in figure 3.6



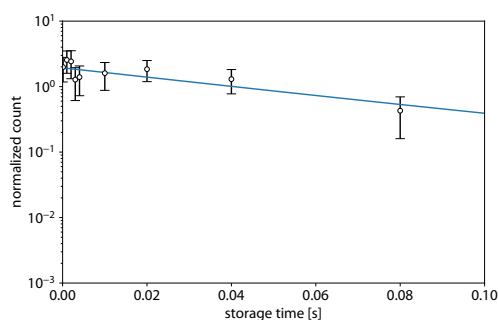
the 2nd peak from the left in figure 3.6



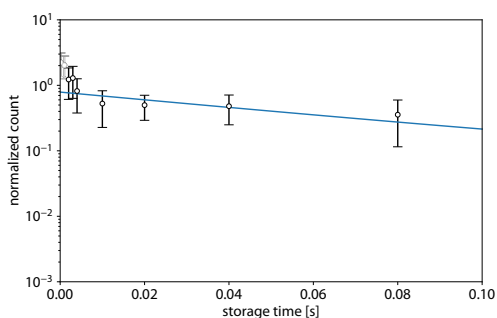
the 3rd peak from the left in figure 3.6



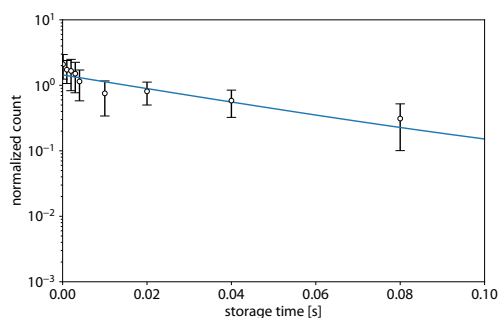
the 4th peak from the left in figure 3.6



the 5th peak from the left in figure 3.6

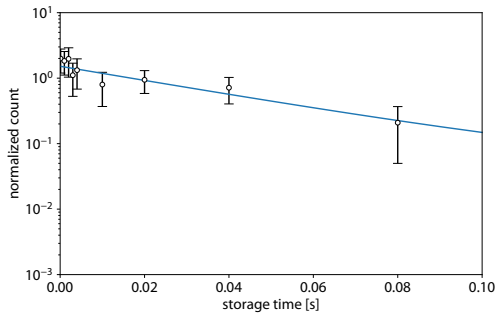
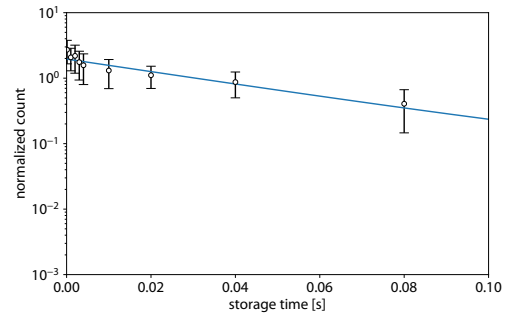
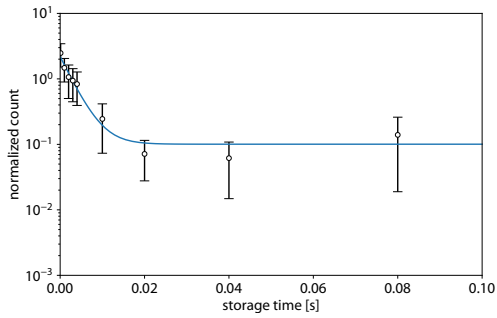
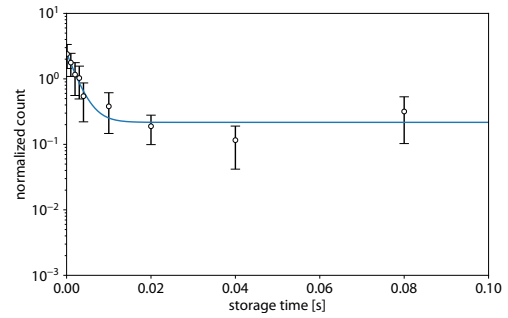
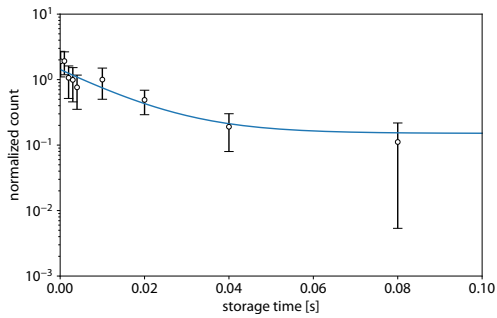
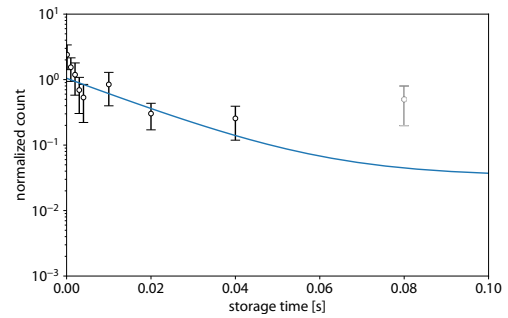
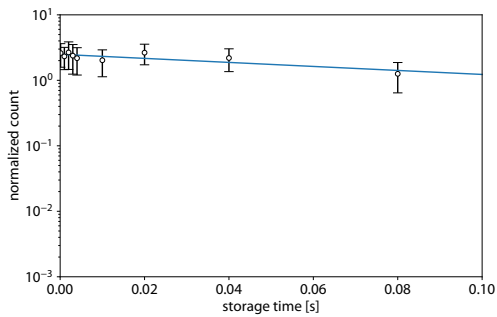
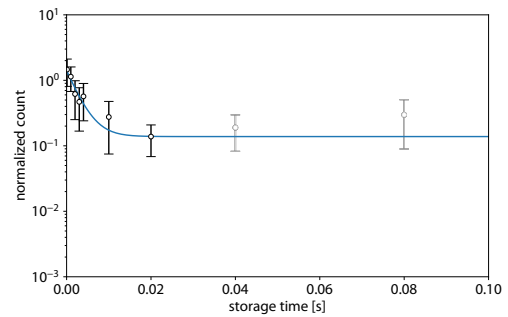


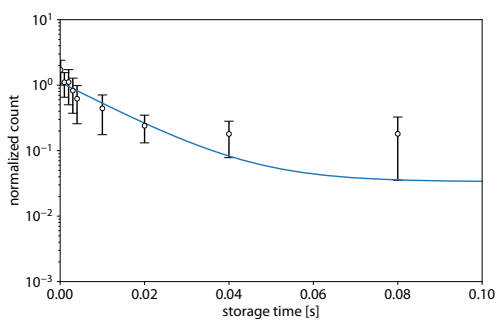
the 6th peak from the left in figure 3.6



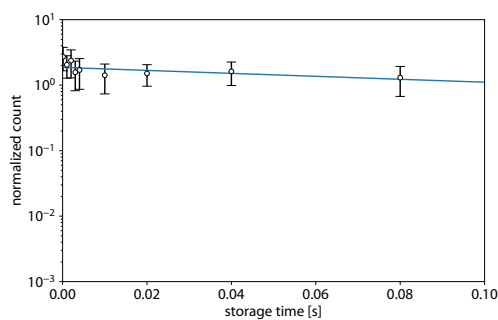
the 7th peak from the left in figure 3.6

Figure3.13: The fitting curves for each peak.

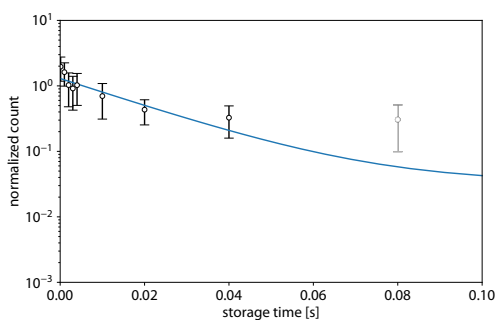
the 8th peak from the left in figure 3.6the 9th peak from the left in figure 3.6the 10th peak from the left in figure 3.6the 11th peak from the left in figure 3.6the 12th peak from the left in figure 3.6the 13th peak from the left in figure 3.6the 14th peak from the left in figure 3.6the 15th peak from the left in figure 3.6**Figure3.13:** (cont.) The fitting curves for each peak.



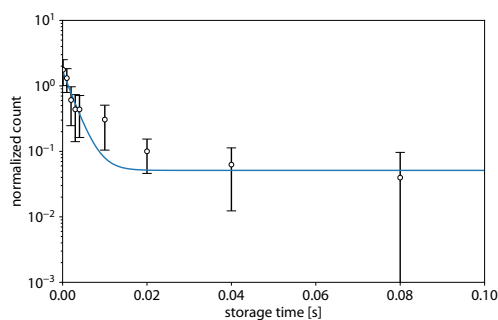
the 16th peak from the left in figure 3.6



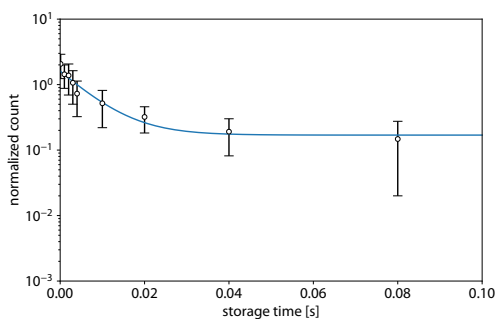
the 17th peak from the left in figure 3.6



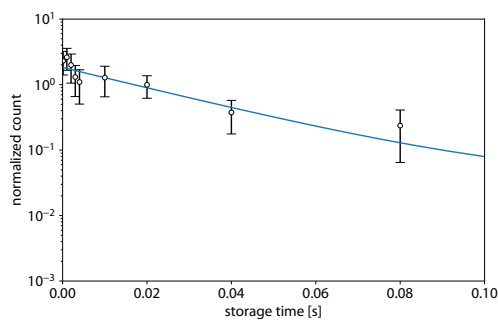
the 18th peak from the left in figure 3.6



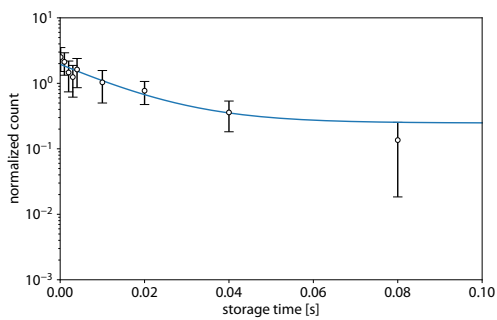
the 19th peak from the left in figure 3.6



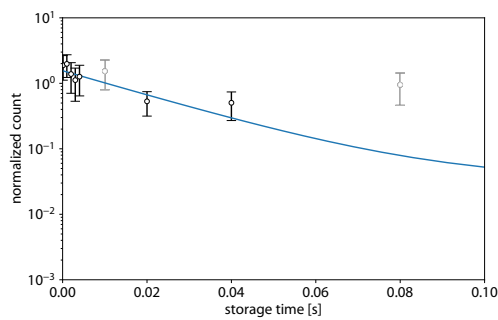
the 20th peak from the left in figure 3.6



the 21st peak from the left in figure 3.6

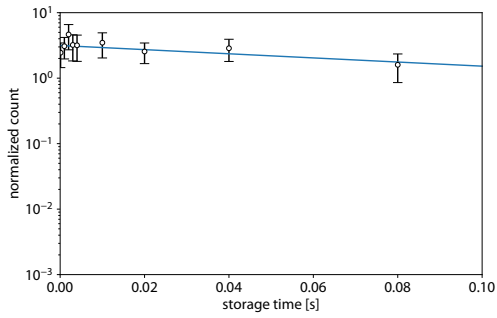
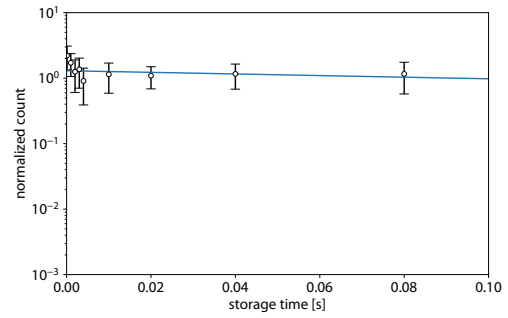
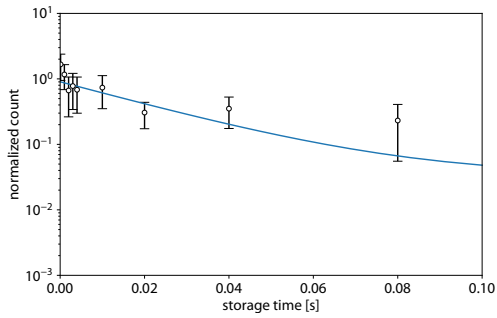
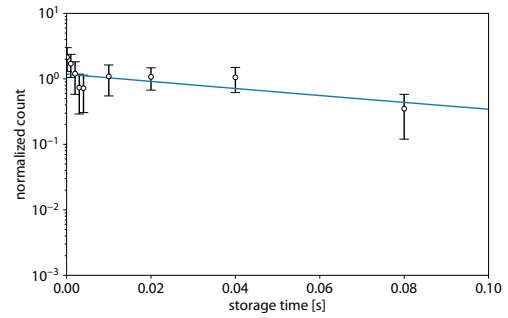
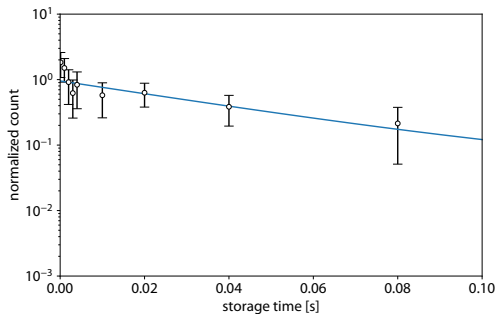
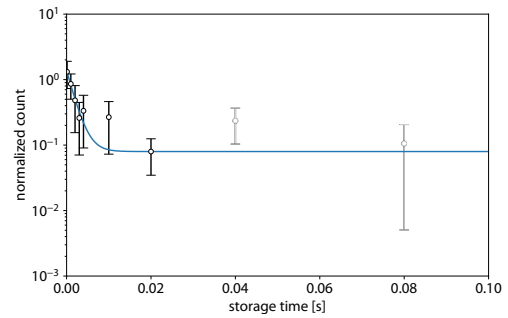
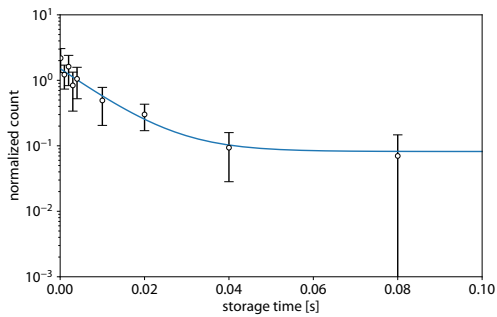
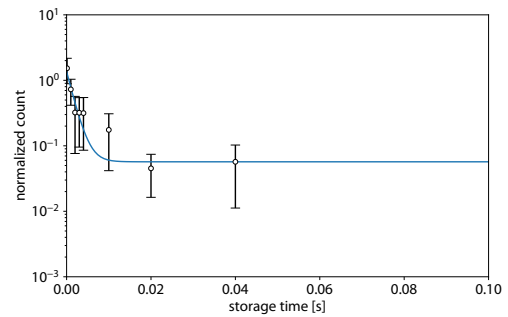


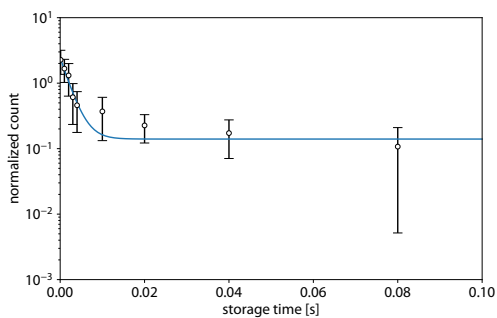
the 22nd peak from the left in figure 3.6



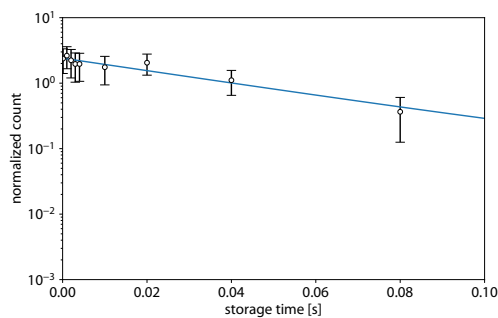
the 23rd peak from the left in figure 3.6

Figure3.13: (cont.) The fitting curves for each peak.

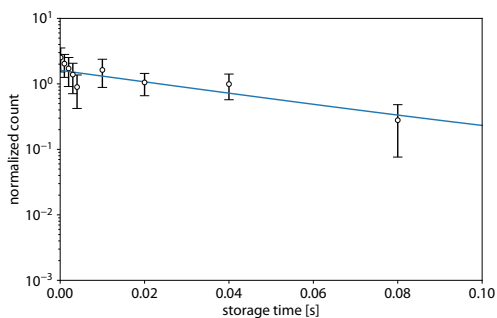
the 24th peak from the left in figure 3.6the 25th peak from the left in figure 3.6the 26th peak from the left in figure 3.6the 27th peak from the left in figure 3.6the 28th peak from the left in figure 3.6the 29th peak from the left in figure 3.6the 30th peak from the left in figure 3.6the 31st peak from the left in figure 3.6**Figure3.13:** (cont.) The fitting curves for each peak.



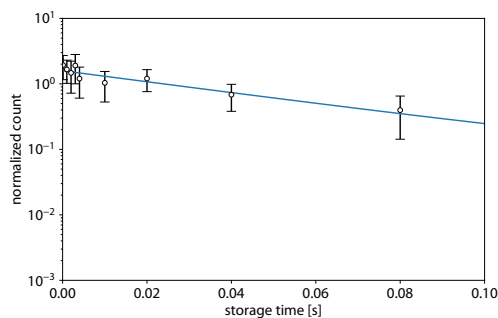
the 32nd peak from the left in figure 3.6



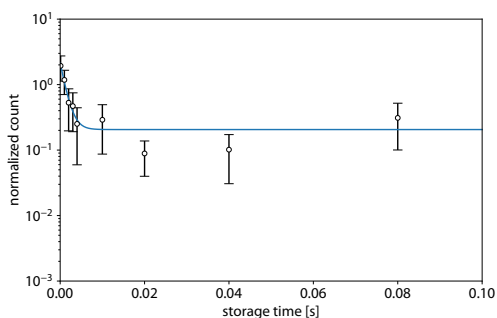
the 33rd peak from the left in figure 3.6



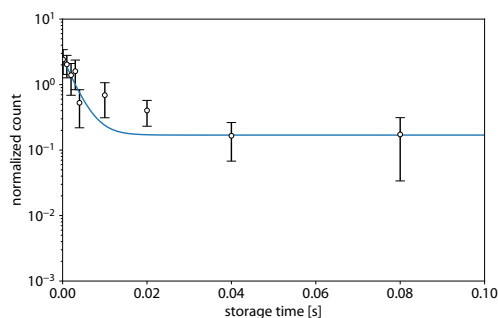
the 34th peak from the left in figure 3.6



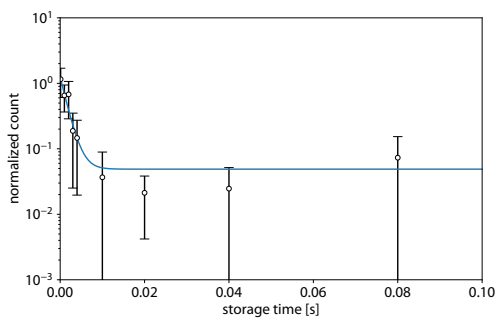
the 35th peak from the left in figure 3.6



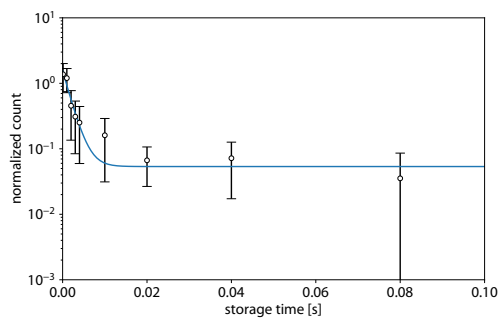
the 36th peak from the left in figure 3.6



the 37th peak from the left in figure 3.6

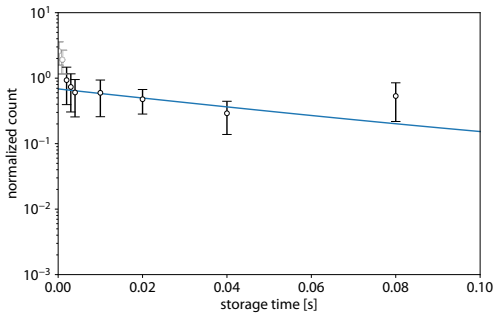
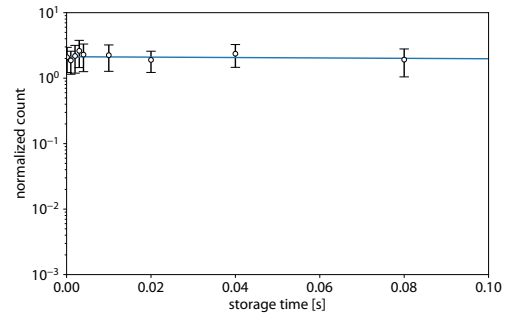
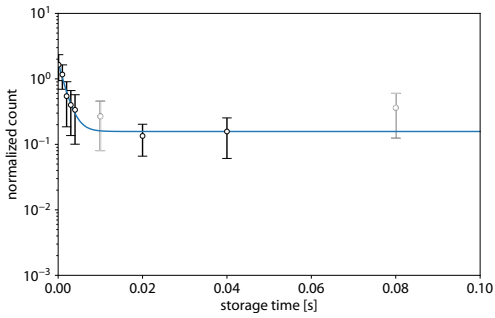
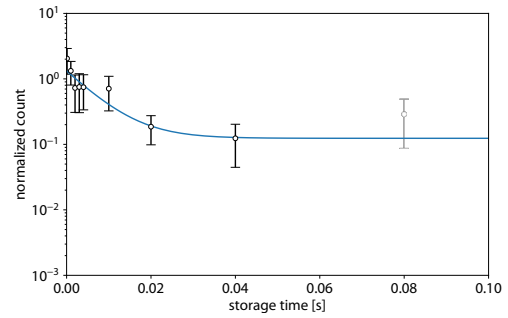
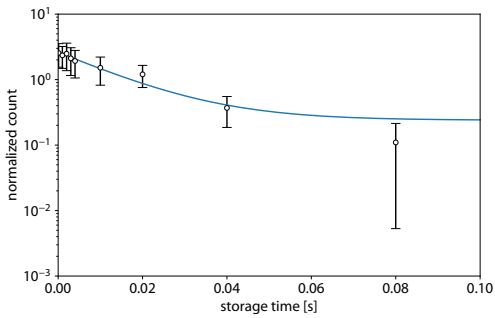
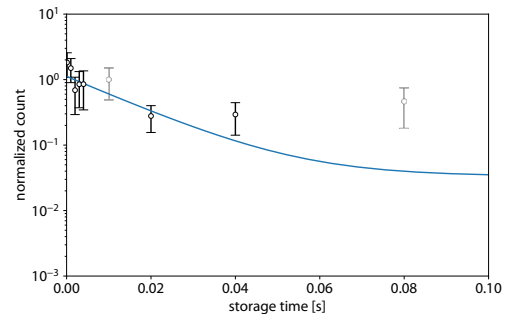
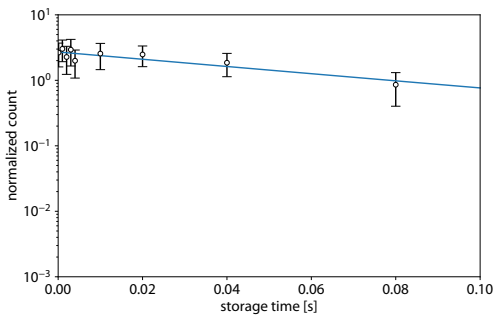
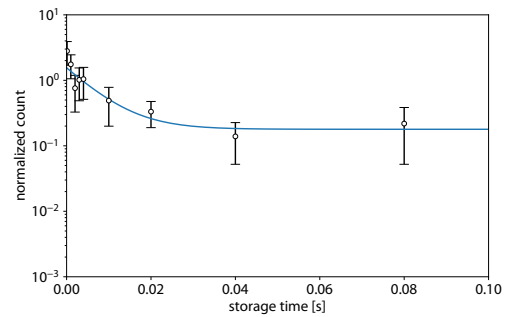


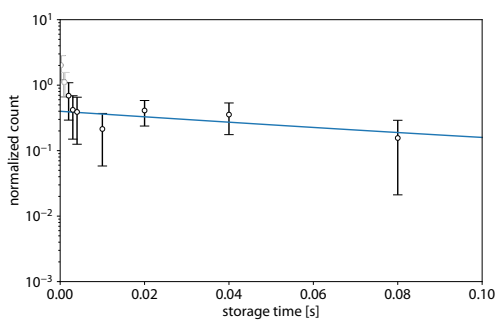
the 38th peak from the left in figure 3.6



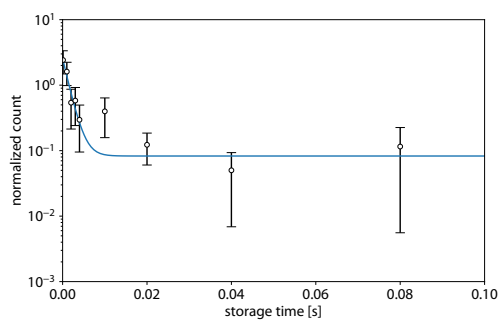
the 39th peak from the left in figure 3.6

Figure3.13: (cont.) The fitting curves for each peak.

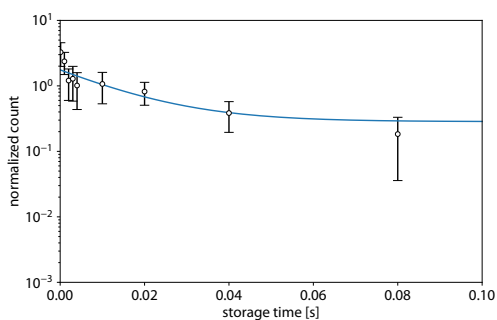
the 40th peak from the left in figure 3.6the 41st peak from the left in figure 3.6the 42nd peak from the left in figure 3.6the 43rd peak from the left in figure 3.6the 44th peak from the left in figure 3.6the 45th peak from the left in figure 3.6the 46th peak from the left in figure 3.6the 47th peak from the left in figure 3.6**Figure3.13:** (cont.) The fitting curves for each peak.



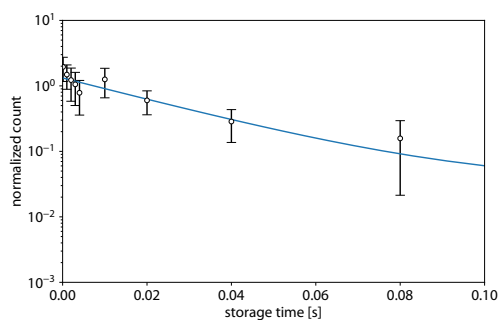
the 48th peak from the left in figure 3.6



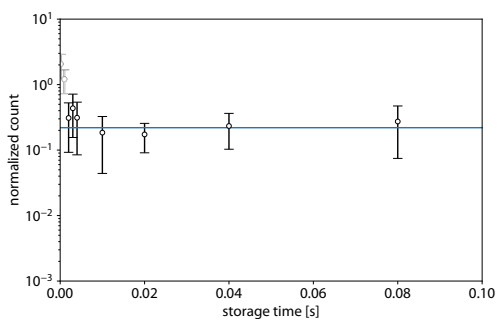
the 49th peak from the left in figure 3.6



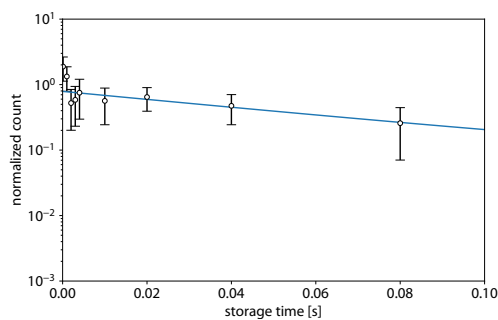
the 50th peak from the left in figure 3.6



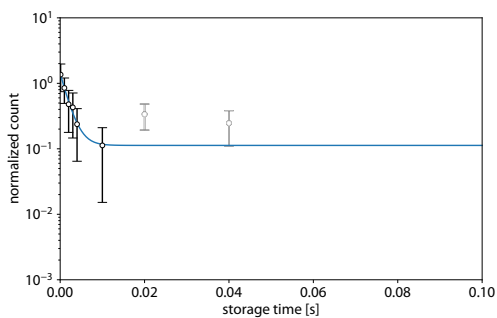
the 51st peak from the left in figure 3.6



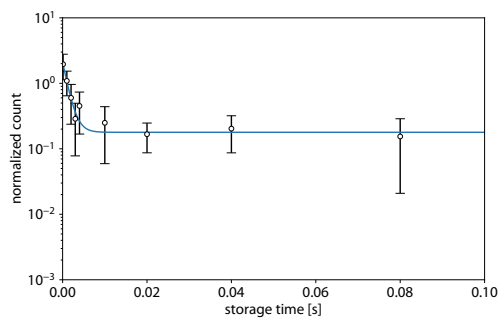
the 52nd peak from the left in figure 3.6



the 53rd peak from the left in figure 3.6

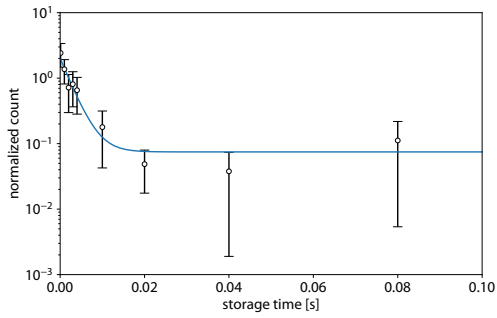
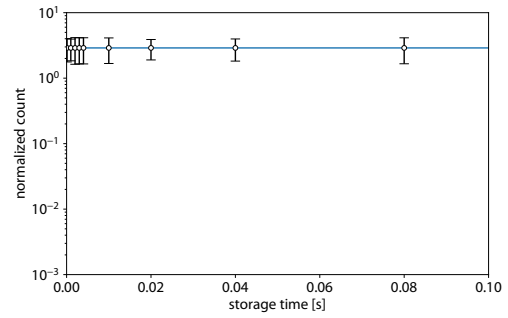
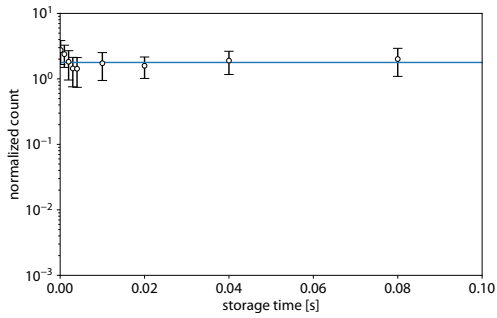
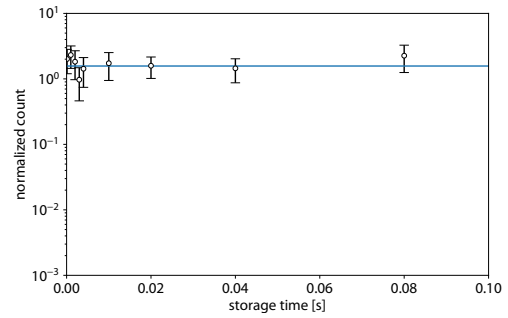
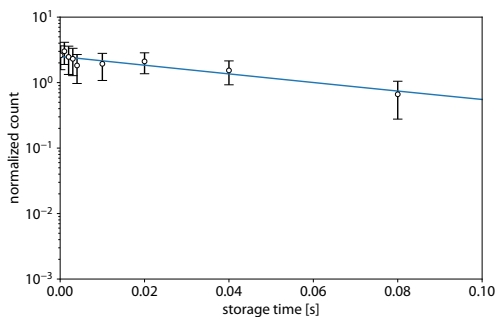
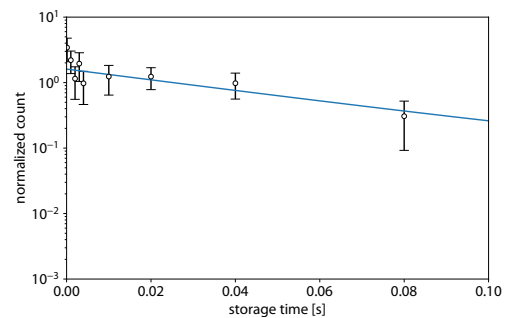
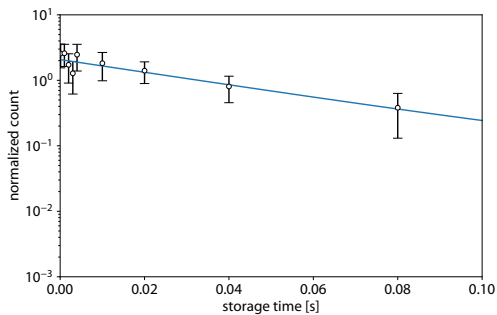
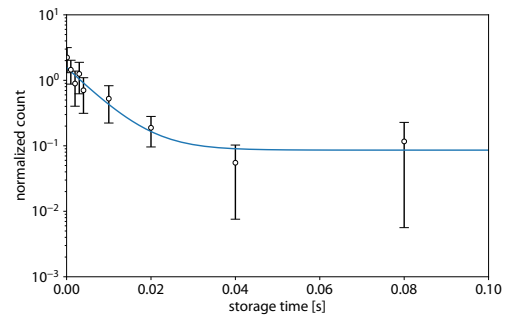


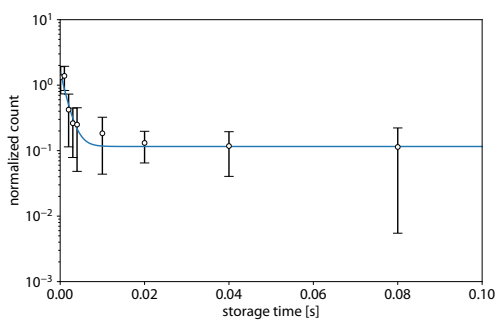
the 54th peak from the left in figure 3.6



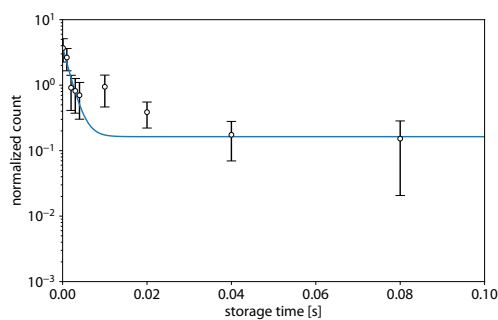
the 55th peak from the left in figure 3.6

Figure3.13: (cont.) The fitting curves for each peak.

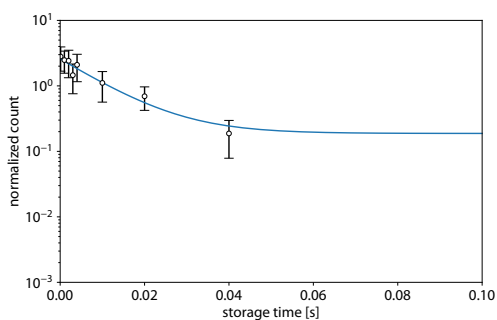
the 56th peak from the left in figure 3.6the 57th peak from the left in figure 3.6the 58th peak from the left in figure 3.6the 59th peak from the left in figure 3.6the 60th peak from the left in figure 3.6the 61st peak from the left in figure 3.6the 62nd peak from the left in figure 3.6the 63rd peak from the left in figure 3.6**Figure3.13:** (cont.) The fitting curves for each peak.



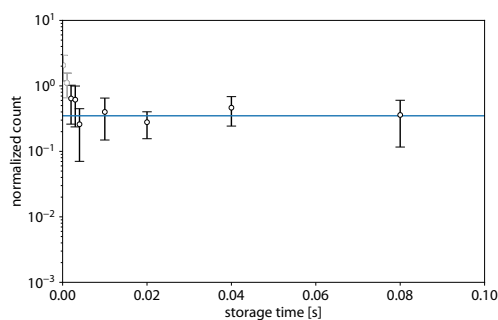
the 64th peak from the left in figure 3.6



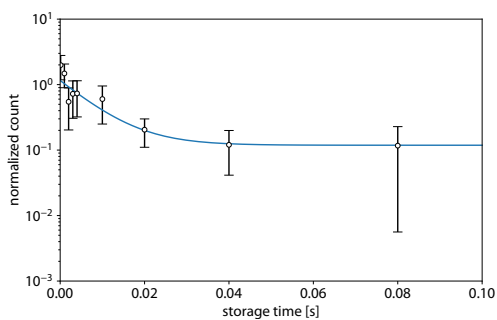
the 65th peak from the left in figure 3.6



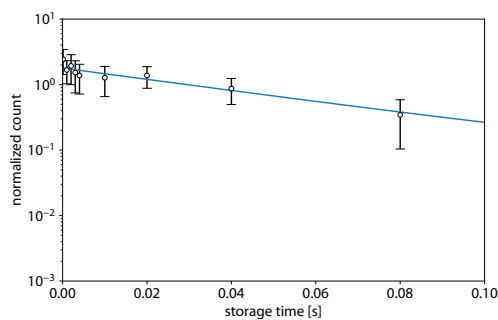
the 66th peak from the left in figure 3.6



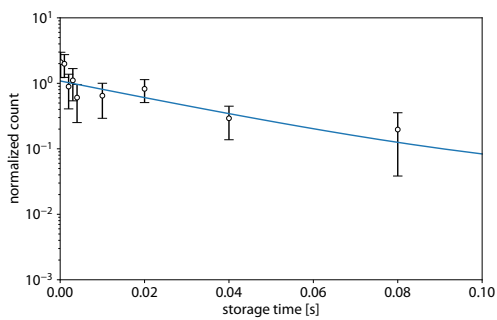
the 67th peak from the left in figure 3.6



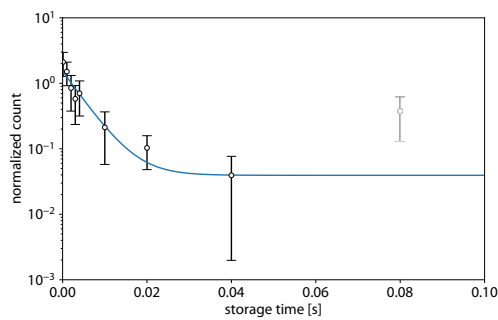
the 68th peak from the left in figure 3.6



the 69th peak from the left in figure 3.6

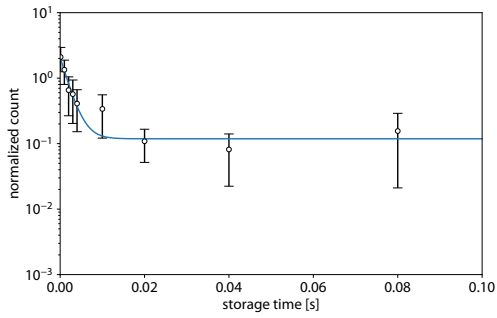
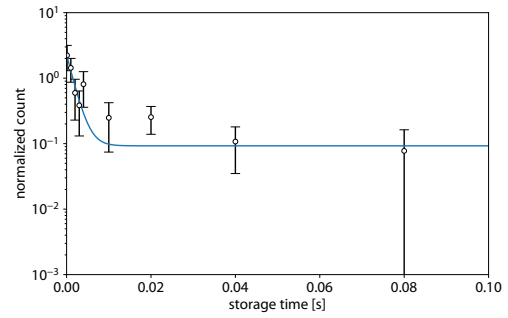
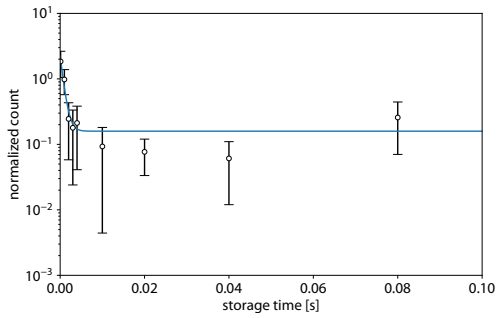
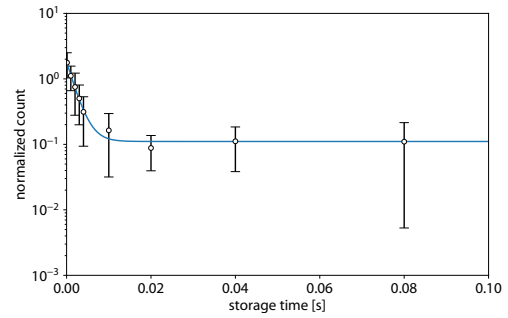
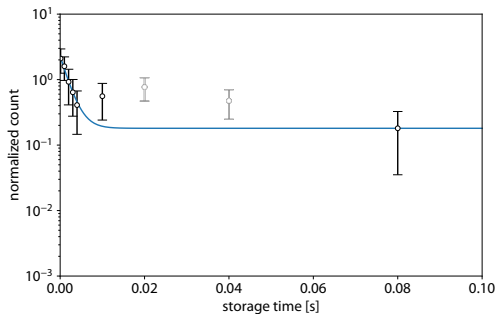
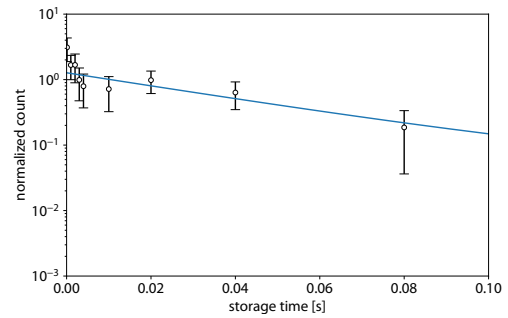
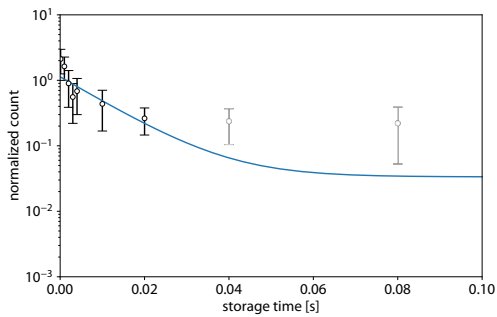
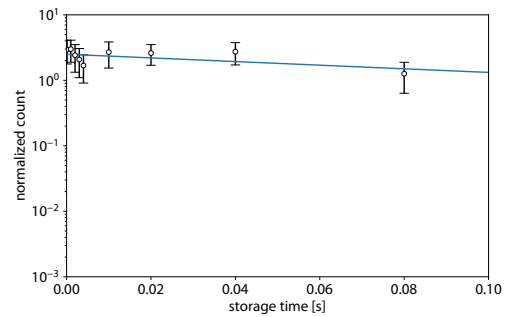


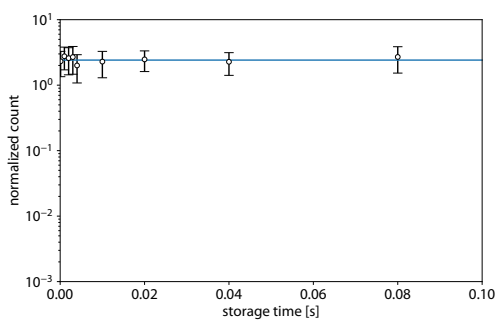
the 70th peak from the left in figure 3.6



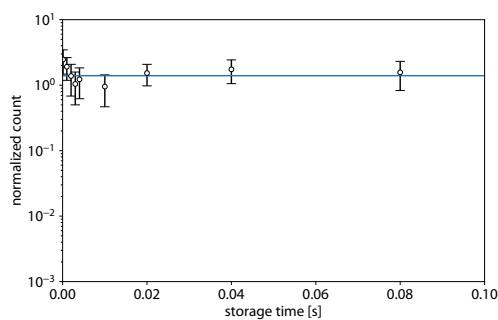
the 71st peak from the left in figure 3.6

Figure3.13: (cont.) The fitting curves for each peak.

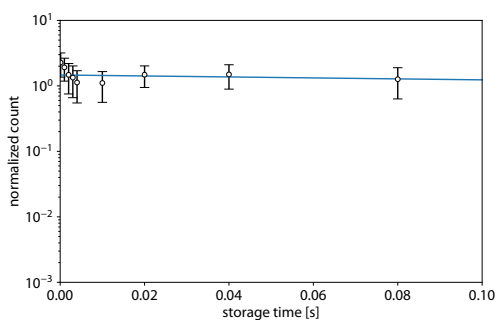
the 72nd peak from the left in figure 3.6the 73rd peak from the left in figure 3.6the 74th peak from the left in figure 3.6the 75th peak from the left in figure 3.6the 76th peak from the left in figure 3.6the 77th peak from the left in figure 3.6the 78th peak from the left in figure 3.6the 79th peak from the left in figure 3.6**Figure3.13:** (cont.) The fitting curves for each peak.



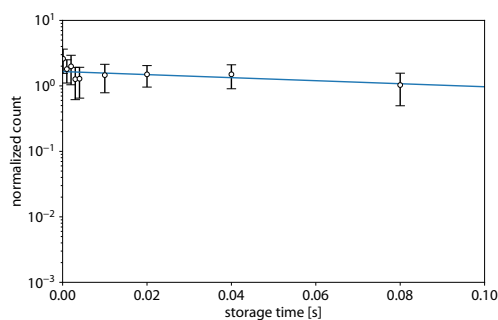
the 80th peak from the left in figure 3.6



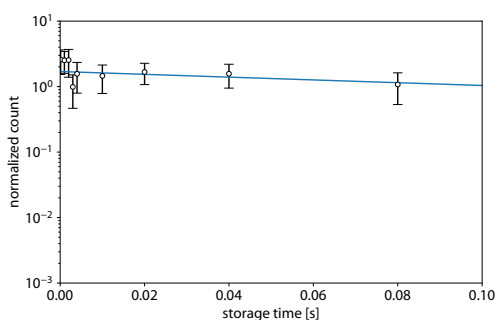
the 81st peak from the left in figure 3.6



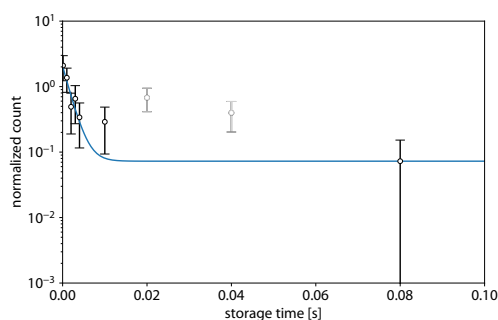
the 82nd peak from the left in figure 3.6



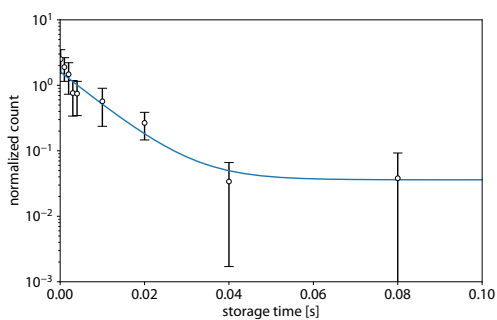
the 83rd peak from the left in figure 3.6



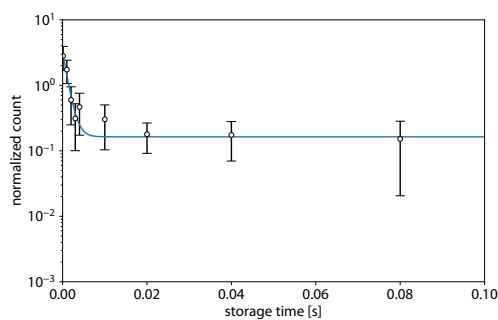
the 84th peak from the left in figure 3.6



the 85th peak from the left in figure 3.6

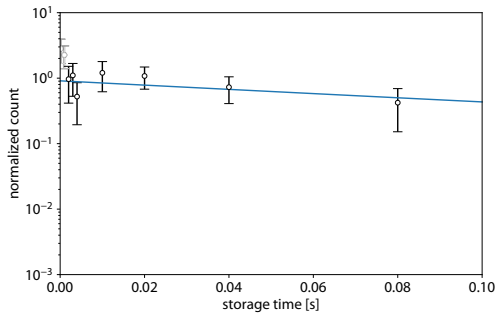
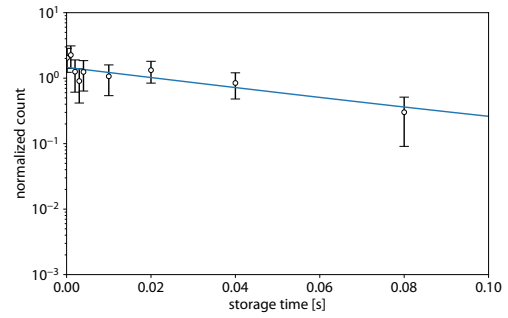
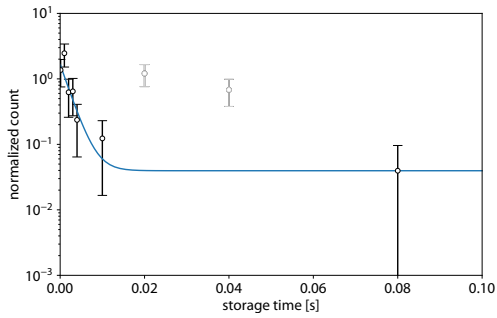
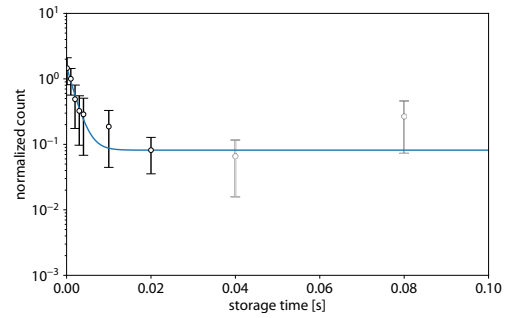
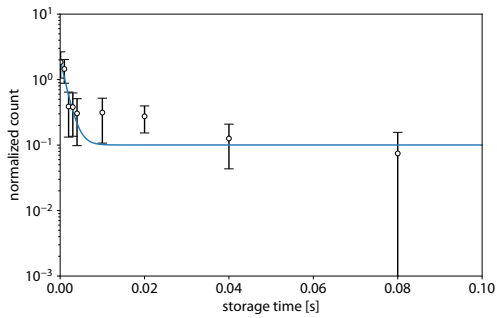
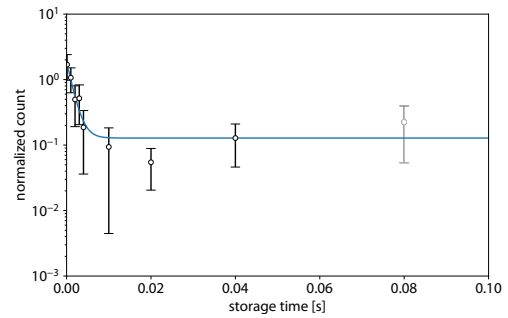
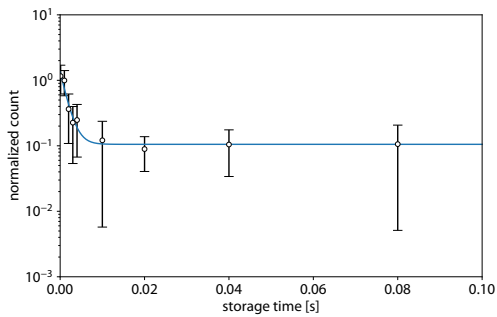
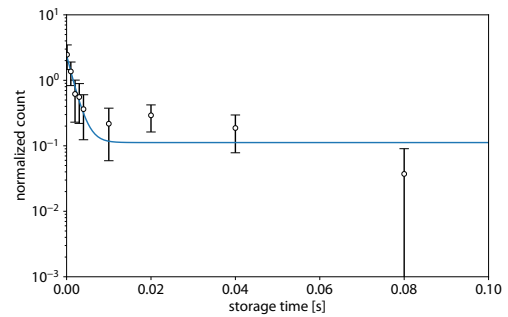


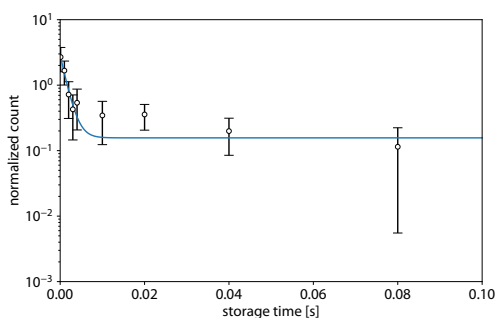
the 86th peak from the left in figure 3.6



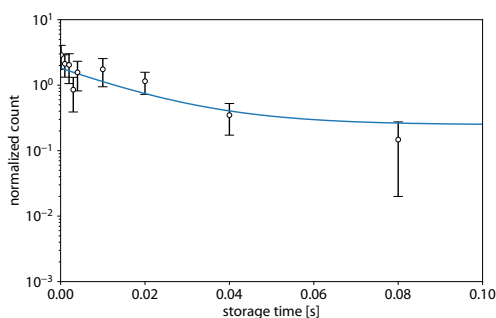
the 87th peak from the left in figure 3.6

Figure3.13: (cont.) The fitting curves for each peak.

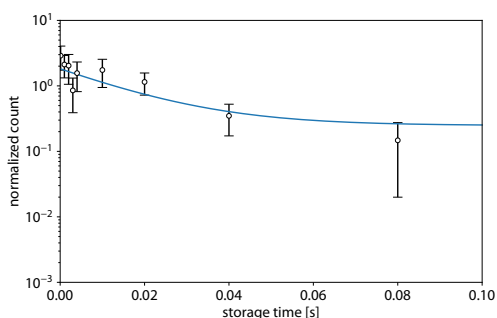
the 88th peak from the left in figure 3.6the 89th peak from the left in figure 3.6the 90th peak from the left in figure 3.6the 91st peak from the left in figure 3.6the 92nd peak from the left in figure 3.6the 93rd peak from the left in figure 3.6the 94th peak from the left in figure 3.6the 95th peak from the left in figure 3.6**Figure3.13:** (cont.) The fitting curves for each peak.



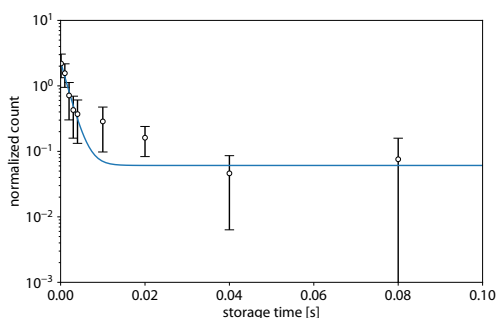
the 96th peak from the left in figure 3.6



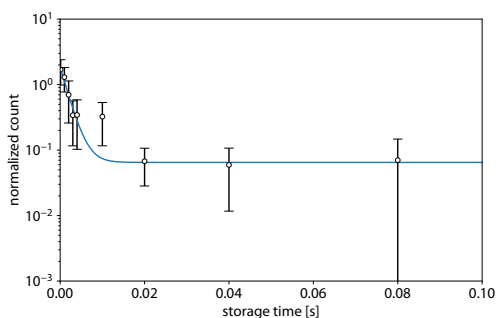
the 97th peak from the left in figure 3.6



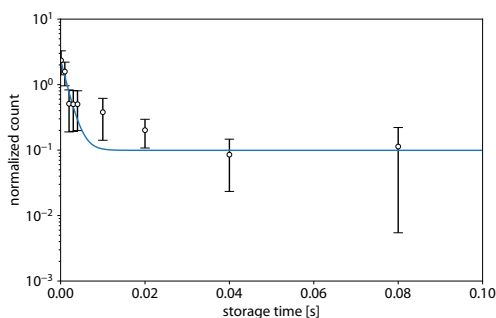
the 98th peak from the left in figure 3.6



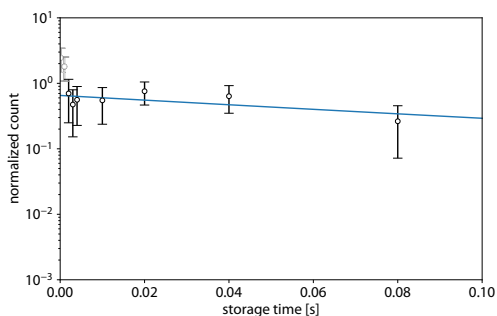
the 99th peak from the left in figure 3.6



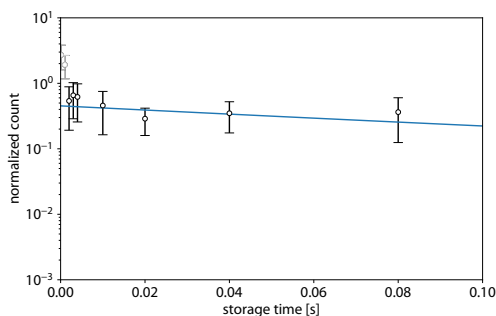
the 100th peak from the left in figure 3.6



the 101st peak from the left in figure 3.6

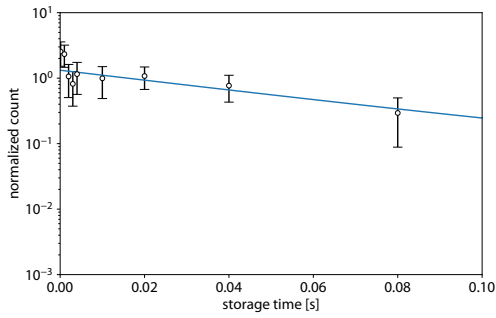
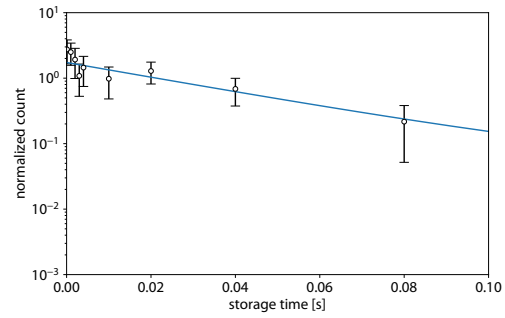
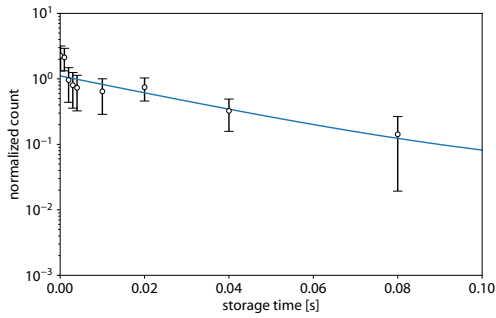
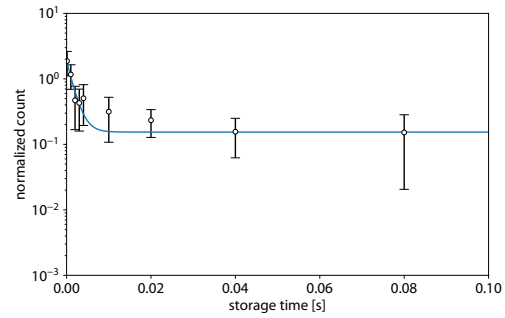
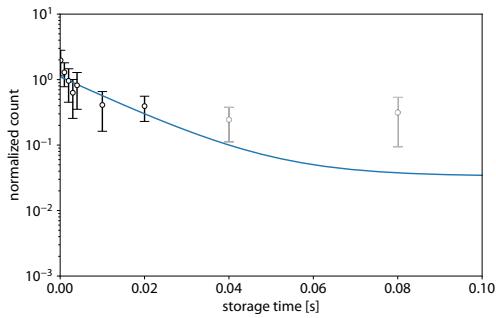
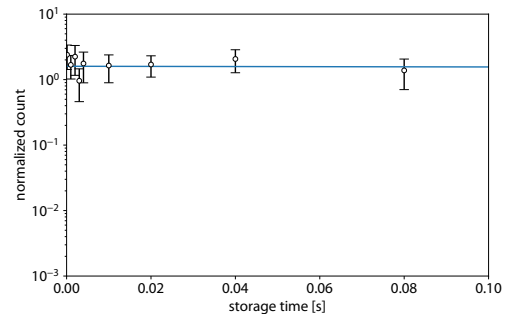


the 102nd peak from the left in figure 3.6



the 103rd peak from the left in figure 3.6

Figure3.13: (cont.) The fitting curves for each peak.

the 104th peak from the left in figure 3.6the 105th peak from the left in figure 3.6the 106th peak from the left in figure 3.6the 107th peak from the left in figure 3.6the 108th peak from the left in figure 3.6the 109th peak from the left in figure 3.6**Figure3.13:** (cont.) The fitting curves for each peak.

3.6 Negative ion formation in the cesium-sputter source

All of the autodetachment experiments of C_2^- reported so far have been performed using cesium sputter ion sources. On the other hand, no peaks other than $X^2\Sigma_g^+ - B^2\Sigma_u^+$ were reported in the photodetachment spectroscopy experiments using a discharge ion source, and the unidentified peaks discussed in this paper were not observed. Similarly, the present peak was not observed in the photodetachment spectroscopy performed using a laser ablation ion source. Therefore, the negative ion formation

process in the cesium sputter ion source causes the long-lived excited state of C_2^- observed in this experiment.

As already mentioned in § 2.2, the Cs sputter ion source produces negative ions by sputtering the sample cathode with thermally ionized Cs^+ cations. However, the detailed mechanism has yet to be fully elucidated, and no established theory exists. Nevertheless, there have been several studies on the electronic and vibrational temperatures of molecular anion beams produced by Cs sputter and gas discharge ion sources. Corderman *et al.* [175, 176] measured the temperature of O_2^- produced by Cs^+ sputtering of an Fe metal target. They reported the electronic and vibrational temperatures to be $T_{elec} \approx 1500 \pm 500$ K and $T_{vib} \approx 5000$ K, respectively. In contrast, they found that O_2^- produced by gas discharge of neutral O_2 has electronic and vibrational temperatures of about 1000 K. Similarly, Breitenfeldt *et al.* [177] compared different ion sources, the metal-ion sputter source (MISS) and laser vaporization source (LVAP), and found the temperature of Co_4^- from the MISS to be much higher than those from LVAP.

According to a recent Vogel's theoretical suggestion [178–180], in anion production in cesium-sputter sources, resonant electron transfer from excited neutral cesium is considered to play an important role. In the present case, this would contribute to producing the C_2^- in highly excited states because the electron binding energies of excited cesium are much smaller than that of the ground-state C_2^- .

Safvan *et al.* [181] claimed that the C_2^- produced by the cesium sputter ion source is almost the ground electronic state. They have measured the ratio of dissociated to non-dissociated cross sections in two-electron detachment by collisions with argon gas. Assuming this ratio should be different depending on the states of C_2^- , they delayed the time-of-flight of C_2^- ions produced by the cesium sputter ion source to decay the $A^2\Pi_u$ state, and found no change in the ratio. They, therefore, concluded that the C_2^- ions produced by the cesium sputter ion source populated is a very few amount of $A^2\Pi_u$ state and were predominantly in the ground electronic state. However, this report does not assume any state other than $X^2\Sigma_g^+$ and $A^2\Pi_u$. We have observed many transition peaks that cannot be explained by any of $X^2\Sigma_g^+$, $A^2\Pi_u$, or $B^2\Sigma_u^+$, which negates their claim.

Chapter 4

Conclusions

Although the diatomic carbon anion C_2^- is one of the most well-studied molecular negative ions, its reaction and transition processes are not fully understood due to its complex electronic structure. Previous experiments suggested the autodetachment process $C_2^{*-} \rightarrow C_2 + e^-$ takes place via an unidentified spin-quartet state. There were several theoretical calculations on the quartet states, but whether or not such bound states exist in the C_2^- is still being debated.

In this thesis, I have performed an experimental study on the electronic excited states of C_2^- and their relaxation dynamics using a cryogenic ion storage ring RICE combined with a high-resolution laser spectroscopy technique. First, the rate of autodetachment of C_2^- was measured in the RICE. A cesium sputter ion source, which is expected to produce beams with high electron and oscillation temperatures, was used as the ion source. From the temporal decay rate of the C_2^- beam intensity in the ring, the autodetachment rate was obtained to be 2.929 ± 0.011 ms, which is in good agreement with previous studies.

Second, to elucidate the origin of the autodetachment process, I have performed a high-resolution photodetachment spectroscopy using a pulsed optical parametric oscillator (OPO) laser. At 10 ms storage time, the photodetachment spectrum was obtained by detecting neutral C_2 molecules produced by photodetachment $C_2^- + h\nu \rightarrow C_2 + e^-$. From the obtained spectrum, the spectroscopic constants for $B^2\Sigma_u^+$ $v' = 5-8$ by applying the $B-X$ transition of $\Delta v = -1$ was determined using spectrum simulation program PGOPHER. Since no peaks attributable to $X v'' > 9$ were detected and A and B states are quickly decayed in μ s and ns order, the initial states to be considered in this spectrum are restricted to $X v'' \leq 9$. The precisions of rotational constants obtained in this study are higher than those of previous studies. These improved experimental values are expected to serve as a benchmark for quantum chemical calculations.

Finally, we observed a large number of unassigned peaks found in the photodetachment spectrum. These unassigned peaks could not be explained as the transitions between the well-investigated electronic states of $X^2\Sigma_g^+$, $A^2\Pi_u$ and $B^2\Sigma_u^+$. Therefore, supposing the existence of an additional electronic excited state, I have studied the lifetime of this state by observing the storage time dependence of the photodetachment spectra: the time-resolved high-resolution spectroscopy of C_2^- . In the result, about one third of the unassigned peaks were found to decay with a lifetime of 1.5 ms to 3 ms. These lifetimes well agree with the autodetachment lifetime of C_2^- which was

2.9 ms. This suggests a possible detachment channel from the unidentified bound states we observed. In addition, the long-lived states other than the ground state $X^2\Sigma_g^+$ were found with a lifetime longer than 100 ms. This suggests the possibility of bound excited states other than the $X^2\Sigma_g^+$, $A^2\Pi_u$ and $B^2\Sigma_u^+$ states.

To summarize, the results obtained in this study strongly suggest the existence of long-lived bound states other than the known bound states ($X^2\Sigma_g^+$, $A^2\Pi_u$ and $B^2\Sigma_u^+$), which are involved in the long-unresolved ms order autodetachment. Although the origin of the unidentified peak is not yet known, the results of this study are expected to be the starting point for many future experimental and theoretical studies as a clue to elucidate the details of the electronic structure of C_2^- .

This study also demonstrates that time-resolved photodetachment spectroscopy using ion storage rings is an effective method for studying the bound excited states of molecular anions. This method, together with the recent lifetime measurements of the long-lived excited states of CH^- (> 10 s) at DESIREE [182], will be a powerful technique for analyzing long-lived excited states.

For further understanding, spectra should be obtained by varying the initial electronic temperature of the ion beam. There were no unidentified peaks in previous spectra obtained with the discharge-type ion source and with the laser ablation ion source. These ion sources are known to produce the molecular ion beams with lower electronic and vibrational temperatures than the cesium sputter ion source, which was used in this study. Similar results are expected to be obtained with these ion sources even if measurement is performed in the cryogenic ion storage ring RICE, where there is no effect of background radiation.

To obtain the lifetime of the long-life component it is necessary to conduct experiments using a cesium sputter ion source with an extended storage time of a few seconds. If the storage time is increased by a factor of ten, the time required for measurement will also increase by a factor of ten, and the number of stored ions will also decrease. For example, it is expected to take several months to obtain the spectrum of Fig. 3.3 with a storage time of 1 second. During this time, the ion source has to be in stable operation. Therefore, it will be necessary to develop a technology to make the ion source output at the electronic, vibrational, and rotational temperatures stable for an extended time.

Appendix A

State-selective ion–Neutral low-energy collision experiments

In this appendix, the state dependence of chemical reactions will be discussed. When atomic molecules collide at very low energies, the reaction branching ratio is highly dependent on the electronic, vibrational, and rotational state of each atomic molecule. This may be why many molecules exist in interstellar space, although the density of matter is rare and the chance for collisions between atoms and molecules should be rare due to the extremely low temperatures. Therefore, we planned to conduct an ultra-low-energy collision experiment using the merged-beam method. We focus on neutral-ion collisions, an exothermic reaction, and present the results of testing a beam source that produces neutral beams with controlled internal states.

A.1 Background from astrochemistry

Since 1937, when it was discovered that molecules exist in interstellar space [27], about 200 species of molecules have already been discovered [183]. In 2016, the Atacama Large Millimeter/submillimeter Array (ALMA), the world's largest radio telescope developed jointly by the United States, Japan, and Europe, will begin full-scale operations, collecting astronomical data with unprecedented sensitivity and resolution. Radio observations with high spatial resolution using ALMA have revealed the distribution and diversity of matter in the forming regions of planetary systems [184], and the study of the origin of planetary systems has made great strides.

The surrounding physical and chemical conditions determine the evolutionary process of molecules in this region. Therefore, it has been newly recognized that the chemical-physical knowledge of interstellar molecules is crucial to investigating the origin of the solar system and various forms of exoplanets. Against this background, the study of elementary processes of reactions by atoms, molecules, and photons in low-temperature and dilute environments is becoming increasingly important.

The reaction between neutral atoms and molecular ions is one of the significant

chemical reactions in interstellar space. In recent years, the reaction between neutral atoms and molecular ions has attracted much attention as an essential reaction process in the formation of complex organic molecules (COMs) [185,186], the building blocks of life. Unfortunately, however, experimental studies of low-energy atomic and molecular reaction processes involving neutral atoms have not progressed because it is difficult to control the motion of neutral atoms by electric or magnetic fields since they have no electric charge, and experiments controlling the collision velocity have rarely been performed. Therefore, we planned to conduct a merged-beam experiment using ion and neutral atomic and molecular beams in order to experimentally pursue the process of matter evolution in interstellar space by measuring its cross section and state dependence and use this knowledge to further our understanding of the origin of star and planet formation. This appendix describes the evaluation of neutral atomic beams suitable for merged-beam experiments and the progress of the preliminary merged-beam experiments [187].

A.2 Overview : merged beam experiment

The merged-beam method is a method in which two or more beams are merged with equal velocity so that their particles collide with each other at a relatively low velocity. In the merged-beam method, the collision energy itself can be controlled, whereas in the ion trap method, only the temperature, i.e., the collision energy distribution, can be controlled. Therefore, the collisional cross-section, rather than the reaction rate, can be measured, and more physically essential discussions can be made.

The primitive merged-beam experiments were alpha particle–electron collisions performed by Davis and Barnes reported in 1929 [188]. The first fruitful result using the merged-beam method was the cation–neutral collision cross-section measurement of Trujillo *et al.* [189], and Belyaev *et al.* [190,191] in 1966. Trujillo *et al.* [189] observed charge transfer from Ar to Ar⁺ and neutral Ar beam is generated with charge transfer cell. Belyaev *et al.* [190,191] observed charge transfer from H to H⁺, and neutral H beams were produced by collisions with He^{*1}.

In low-energy collisions, the collision energy and the internal state affect the reaction cross section. In recent years, it has been known that not only electronic and vibrational states but also rotational states affect the reaction cross section [193,194]. To measure such state-selective cross sections, it is necessary to conduct a merged-beam experiment with a molecular beam whose internal state is controlled. For this measurement, an ion storage ring is appropriate for generating molecular anion beam [195]. Ion storage rings have the advantages of not only phase space compression of ion beams but also vibrational and rotational cooling for molecules with permanent dipole moments.

All of the recently developed cryogenic ion storage rings are also designed for merged-beam experiments, with ion–electron and ion–neutral collisions planned for CSR [154,155], positive ion–negative ion collisions for DESIREE [151,152], and ion–neutral collisions for RICE [57]. CSR have already been used for ion–electron merged-

^{*1} Their paper published in 1967, uses CO₂ to produce neutral H beams [192].

beam experiments [194] and ion-neutral merged-beam experiment [196].

A.3 Overview : neutral beam source

A.3.1 Requirement of neutral beam source

The merged beam experiment requires controlling the collision energy by controlling the collision velocity. Let the velocities of the two beams be v_1 and v_2 , and the angle between them be θ , then the relative velocity is $v_r = \sqrt{v_1^2 + v_2^2 - 2v_1v_2 \cos \theta}$. Therefore, the relative energy E_r at the center-of-mass system in the non-relativistic limit is

$$E_r = \frac{1}{2}\mu v_r^2 = \mu \left(\frac{E_1}{m_1} + \frac{E_2}{m_2} - 2\sqrt{\frac{E_1 E_2}{m_1 m_2}} \cos \theta \right), \quad (\text{A.1})$$

where E_1 and E_2 are kinetic energies, m_1 and m_2 are masses, μ is a reduced mass, i.e., $\mu = m_1 m_2 / (m_1 + m_2)$. As seen above, controlling the relative energy requires not only reducing the variance of E_1 and E_2 but also reducing the variance of θ , i.e., the angular spread of the beam. The phase space of the molecular ion beam is compressed by the ion storage ring. The neutral atomic beam is generated by neutralizing the collimated anionic beam to control the kinetic energy and angular spread of the neutral atom beam.

The internal state must be controlled to measure the state-selective cross-section. The molecular ion beam is radiatively cooled employing the cryogenic ion storage ring RICE. The neutral atomic beam does not need to consider vibrational and rotational levels, so only the electronic state needs to be considered.

Therefore, the requirements to be satisfied by the neutralization apparatus for a neutral atomic beam source are: 1. the variance of kinetic energy and angular spread should not be increased by neutralization, and 2. no electronic excitation should occur. There are two possible neutralization methods, detachment by collision with gas and photodetachment at wavelengths near the electron affinity. In the present study, we employed photodetachment, which satisfies both requirements.

A.3.2 Neutral carbon atomic beam

In this study, neutral carbon atoms are produced photodetached with a photon at 808 nm. The energy diagram of C^- and C is shown in Fig. A.1. There are two electronic levels in C^- below the detachment threshold, ^4S and ^2D [197–201]. If the C^- beam consists only of the ^4S state, the C^- transitions to the neutral ground state $\text{C } ^3\text{P}$ by photodetachment. Note that we cannot control the level of fine splitting, $^3\text{P}_0$, $^3\text{P}_1$, and $^3\text{P}_2$. If the C beam contains $^2\text{D}_{3/2}$ and $^2\text{D}_{5/2}$, it can transition to $\text{C } ^1\text{D}$ by photodetachment. Since the lifetime of $\text{C } ^3\text{P}$ is 10^6 – 10^8 s [202], it is not relaxed before arriving at the interaction region of the merged beam apparatus. Therefore, the photodetached beam will contain electronically excited states.

According to Scheer *et al.* [199] and Takao *et al.* [47], the C beam produced by

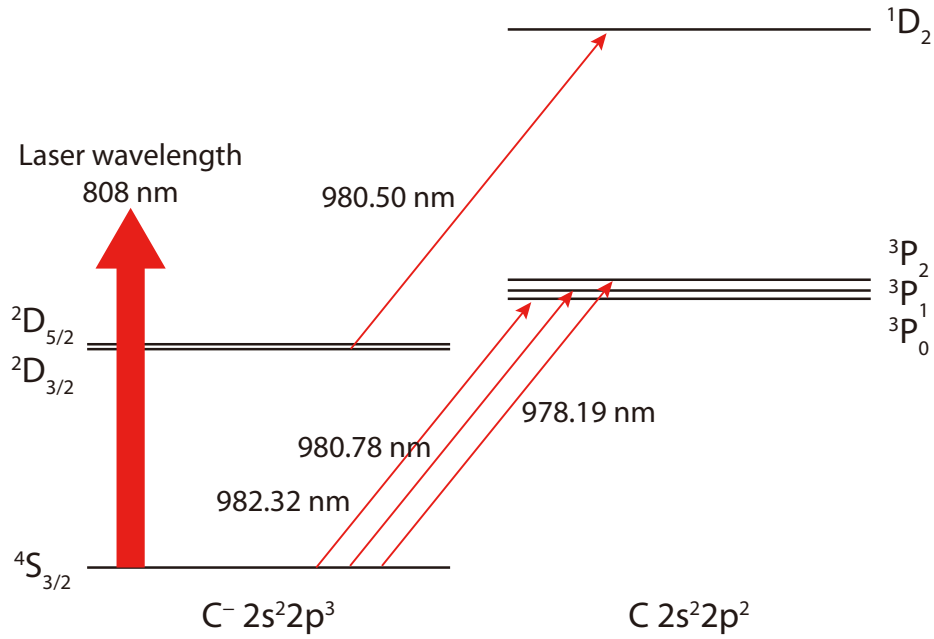


Figure A.1: Energy Diagrams for C^- and C based on [197–201,203]

a cesium sputter ion source contains almost few 2D states. Therefore, the cesium sputter ion source is employed in this experiment.

The beam intensity needs to be 10 nA in terms of monovalent ions. For example, suppose the reaction cross sections of $C + H_3^+ \rightarrow CH^+ + H^2$ and $C + H_3^+ \rightarrow CH_2^+ + H$ are to be measured on the condition that H_3^+ is on the order of 1 μA , the beam diameter of both is about 20ϕ , the beam energy of both is about 21 keV in C , and the merging region is about 1 m. Then the neutral carbon atom beam of the order of 10 nA is required to detect the sub cps order of the reaction product since the reaction cross-section is around 10^{-15} – 10^{-16} cm^2 [204].

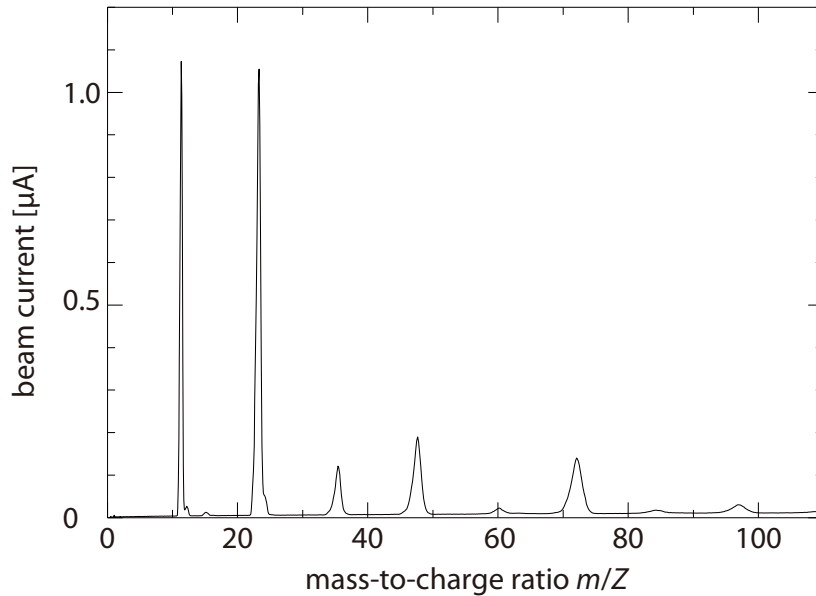
Fig. A.2 shows a typical mass spectrum of the output from the cesium sputter ion source SNICS II with a carbon cathode. To obtain an output of about 10 nA from this source, the detachment efficiency has to be about 1 %.

To minimize the momentum perturbation of the neutral carbon beam due to residual gas, the flight distance should be shortened. Therefore, a semiconductor laser array (808 nm, 60 diodes, 105 mm width, 5000 W, custom-made by Northrop Grumman) was orthogonally set up to the C^- beam.

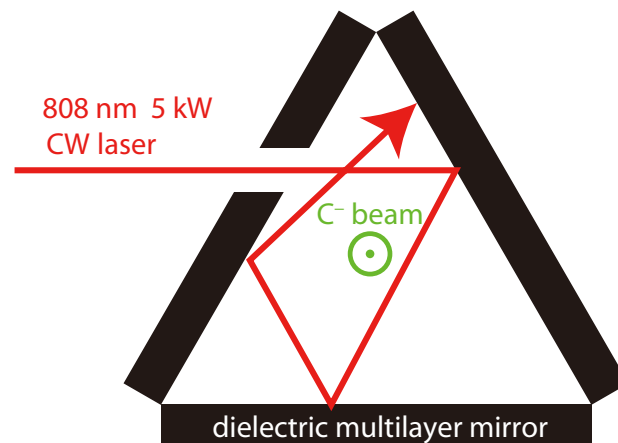
The photodetachment efficiency is obtained by

$$\eta = 1 - \exp\left(-\frac{P\sigma}{vmE}\right) \quad (A.2)$$

where P is the laser power, E is the laser energy, σ is the photodetachment cross section, v is the beam velocity and w is the laser spot width along the beam. Since the photodetachment cross-section is about 1.4×10^{-17} cm^2 for photon energy of 1.5 eV [205–208], the photodetachment efficiency is on the order of 10^{-3} and does not meet the necessary requirement. Therefore, an optical amplifier with three dielectric



FigureA.2: Typical Mass to charge ratio of carbon ion obtained by the SNICS II.



FigureA.3: Scheme of the optical amplifier for anion neutralizer.

multilayer mirrors was built to improve the photon flux density. Fig. A.3 is the scheme of the optical amplifier.

The amplifier is installed in a vacuum chamber. For this reason, the amplifier should be water-cooled. Because the water-cooling system must be made of a material with high thermal conductivity, arc welding and resistance welding cannot be used. Then, machining and EB welding were mainly used with aluminium for base material.

Three AR-coated cylindrical lenses made of synthetic fused silica are used for longitudinal focusing, as shown in fig. A.4. Lenses made of BK7 are unsuitable for this experiment because they quickly break due to large coefficient of thermal expansion.

Other examples of photodetachment devices are introduced here: O'Connor *et*

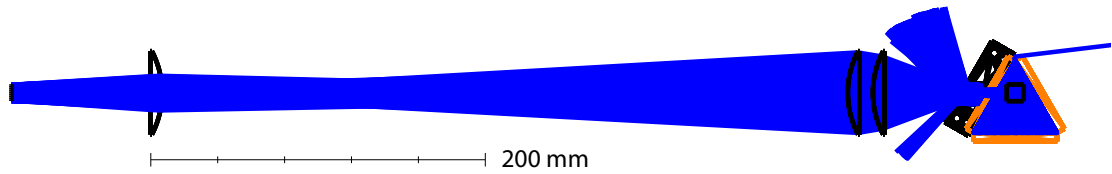


Figure A.4: Scheme of the optical system and laser path for the optical amplifier.

al. [204] have developed a device without mirrors and put the laser at a slight angle to the C^- beam. This device eliminates the possibility of cooling water leakage into the chamber and maintains low pressure because there are no devices in the chamber. Bresteau *et al.* [209, 210] use a low-power laser and amplify the light using a cavity outside the chamber. This apparatus does not need a high-power laser and increases safety, but it is not easy to maintain stable oscillation over a long time using a cavity.

A.3.3 Brief evaluation of neutral beam source

An optical ray tracing simulation by Zemax Optic Studio estimates that the amplified total photon flux is 8 times as much as that expected in the single-pass configuration at a reflection rate of 95%. The efficiency was enhanced by an order of magnitude by the optical amplifier. At a laser power of 5000 W, the expected neutral C beam intensity would be ~ 25 nA out of $1 \mu\text{A}$ negative ion beam in preliminary trial.

This optical amplifier has two problems: 1. The EB welds are damaged by the piping removal and attachment due to the adjustment. Then the cooling water significantly leaked, and the chamber pressure deteriorated. 2. Due to the optical durability of the dielectric multilayer, the laser power that can realistically be input is about 2 kW. These problems could be solved by developing an optical amplifier that uses a gold mirror and is formed by machining with a cooling section.

A.4 Outlook: merged beam experiment with RICE

The cation beam's state is controlled by a cryogenic ion storage ring. Therefore, the ion without a permanent dipole moment is unsuitable for the target ion. For instance, HD^+ is appropriate, but not H_2^+ or H_3^+ . Fig. A.5 (a) shows a radiative cooling simulation of HD^+ , obtained by the solving rate equation [211]. The Einstein's A coefficients are taken from Amitay *et al.* [212] and Pilon *et al.* [213], and the initial distribution is assumed to be the Boltzmann distribution at 1000 K. The cooling time that the 80% ions are in the ground state is the order of 10^2 seconds.

The bottleneck of the cooling process is the long time to stay in $v = 0, J = 1$ state. Pumping up from the $v = 0, J = 1$ state to the $v = 2, J = 0$ state by photon ($2.68 \mu\text{m}$) can speed up the cooling time. Fig. A.5 (b) shows a cooling simulation with the pump-up laser, which can bring about 80% of the system to the ground state in the order of 10^1 seconds.

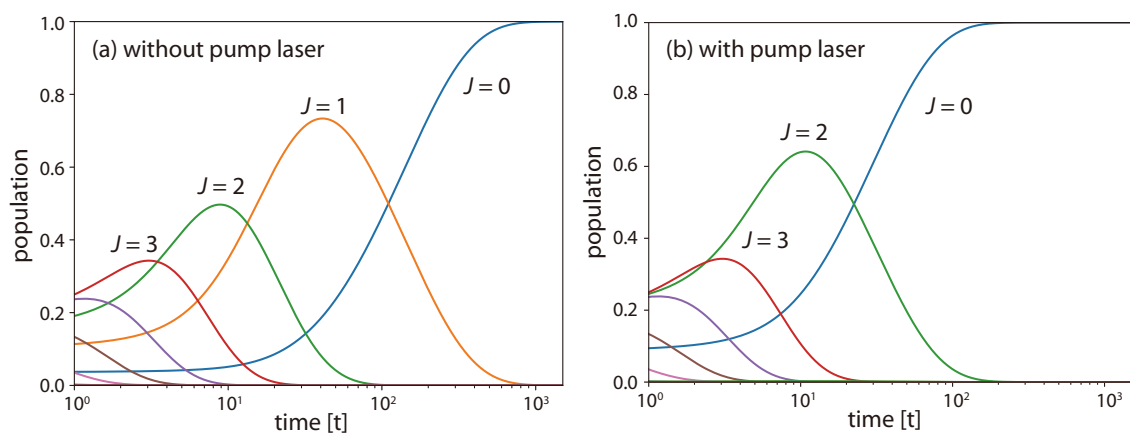


Figure A.5: (a) The radiative cooling simulation of HD^+ . (b) The simulation with $2.68 \mu\text{m}$ laser pumping from $v = 0, J = 1$ to $v = 2, J = 0$.

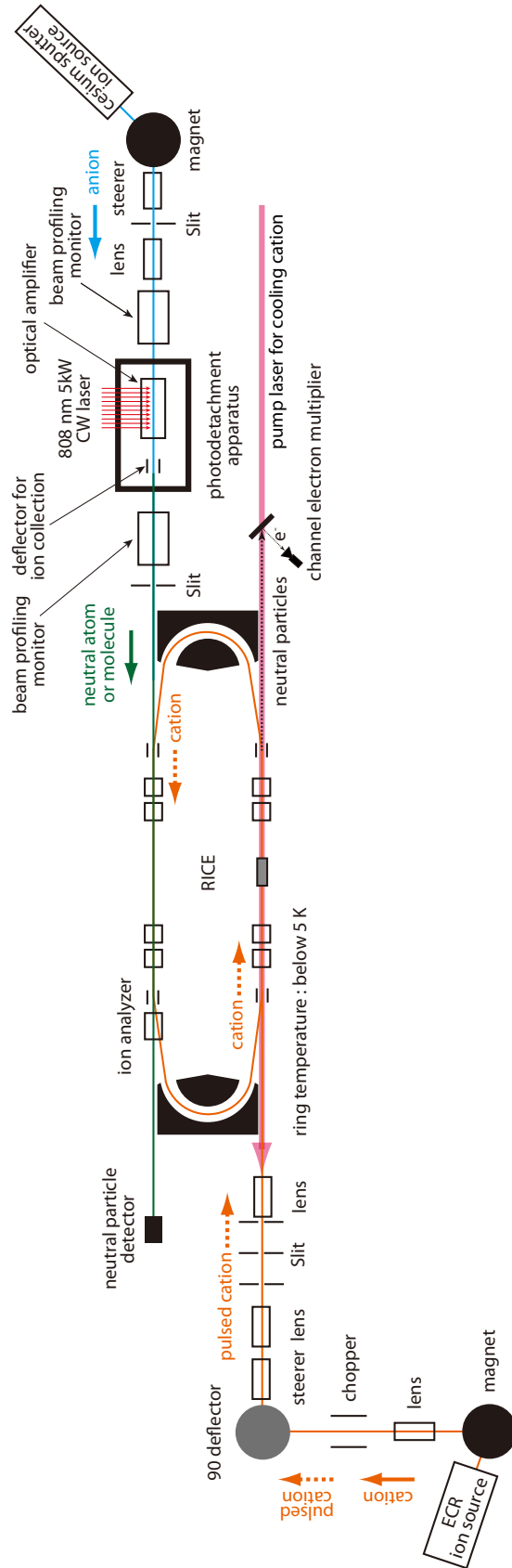


Figure A.6: Brief schematics of the merged beam experiment with RICE.

Fig. A.6 shows the schematics of the merged beam experiment with RICE. There are three issues that will make this scheme feasible. The first is the stable operation of the ion and neutral beam sources. As mentioned earlier, the neutral atom beam source is being redeveloped for stable operation. The second is the development of product detectors. O'Connor *et al.* [204] and Hillenbrand *et al.* [214] employed three 90-degree deflectors to separate C^+ , CH^+ and CH_2^+ . The detector for our experiment is currently under development. The third is the decrease in the number of stored ions during cooling. The number of stored ions decreases by two orders of magnitude or more from the number of incident ions after storing the order of 10^2 seconds. Therefore, long time measurement is necessary. Before conducting a merged-beam experiment using RICE, we should try merging the beams extracted from the ion source without the storage ring.

Acknowledgements

First and foremost, I am extremely grateful to my supervisor, Prof. Yuji Nakano, who has made numerous scientific and technical instructions and financial support to continue my work. His practical coaching was essential to this work. I also want to thank Prof. Toshiyuki Azuma for all his enormous help and advice with this Ph.D. I am deeply grateful not only for the great amount of scientific instruction but also for allowing me to employ RICE for a long time.

Also, thanks to Dr. Susumu Kuma, Dr. Naoki Kimura, and Dr. Kiattichart Chartkunchand. Their immense knowledge and plentiful experience have encouraged me all the time in my research and daily life. When I was at a loss in front of a complex and challenging spectrum, Prof. Masaaki Baba carefully guided me through the rudiments of the spectral analysis method and also made me feel positive. I appreciate his kindness. Prof. Masakazu Nakajima, Prof. Toshiyuki Takayanagi, and Prof. Motomichi Tashiro for their much support in the preliminary theoretical calculations. Thanks very much for undertaking the complex calculations and their explanations regarding the existing theoretical calculations. I also would like to thank Prof. Haruo Shiromaru for his advice on my JPSJ paper.

Furthermore, I was fortunate to have many colleagues. Mr. Sakumi Harayama helped me with operating and maintaining RICE and the ion source, and Dr. Takuma Okumura taught me various things and gave me a pep talk. Mr. Go Kawakami, Mr. Takahiro Oaku, and Dr. Yoko Shina, who is the colleagues at Rikkyo University pushed forward with the merging beam experiment.

I also appreciate Prof. Yoshiro Azuma and Prof. Fumihiro Koike, who were my advisors during my undergraduate and master's programs. My colleague at that time, Dr. Satoshi Kosugi, also gave me encouragement.

I would like to thank those who were not directly involved in this study. Dr. Francesco Fumarola provided me with a room to write my Ph.D. thesis and constantly encouraged me to write it. In addition, Ms. Mahomi Kamada helped me with drawing figures. Prof. Satoru Saito was always heartwarmingly supportive, and Dr. Yasuhito Narita gave me advice on my Ph.D. life. Dr. Ayako Ajima and all the Riken tea club members were always encouraging, and Dr. Masamitsu Watanabe, the club president, taught me how to be a doctoral student. This work was done with the support of many other people as well. I would like to reiterate my gratitude for their support.

This work was supported by RIKEN Junior Research Associate Program (JRA). I could not have accomplished this work without this program. In addition, Rikkyo University Special Fund for Research (SFR) and Rikkyo University emergency salary scholarship were essential to the continuation of the work.

Bibliography

- [1] E. J. D. Mahoney, B. S. Truscott, M. N. R. Ashfold, and Yu. A. Mankelevich. Optical emission from C_2^- anions in microwave-activated CH_4 / H_2 plasmas for chemical vapor deposition of diamond. *The Journal of Physical Chemistry A*, 121(14):2760–2772, April 2017. doi:10.1021/acs.jpca.7b00814.
- [2] Richard E. Honig. Mass spectrometric study of the molecular sublimation of graphite. *The Journal of Chemical Physics*, 22(1):126–131, January 1954. doi:10.1063/1.1739819.
- [3] Kenneth S. Pitzer and Enrico Clementi. Large molecules in carbon vapor. *Journal of the American Chemical Society*, 81(17):4477–4485, September 1959. doi:10.1021/ja01526a010.
- [4] H. Hintenberger, J. Franzen, and K. D. Schuy. Notizen: Die periodizitäten in den häufigkeitsverteilungen der positiv und negativ geladenen vielatomigen kohlenstoffmolekülonen C_n^+ und C_n^- im hochfrequenzfunken zwischen graphitelektroden. *Zeitschrift für Naturforschung A*, 18(11):1236–1237, November 1963. doi:10.1515/zna-1963-1113.
- [5] N. Fürstenau and F. Hillenkamp. Laser-induced cluster-ions from thin foils of metals and semiconductors. *International Journal of Mass Spectrometry and Ion Physics*, 37(2):135–151, February 1981. doi:10.1016/0020-7381(81)80002-2.
- [6] J. Bernholc and J. C. Phillips. Kinetics of cluster formation in the laser vaporization source: Carbon clusters. *The Journal of Chemical Physics*, 85(6):3258–3267, September 1986. doi:10.1063/1.450996.
- [7] Shihe Yang, K.J. Taylor, M.J. Craycraft, J. Conceicao, C.L. Pettiette, O. Cheshnovsky, and R.E. Smalley. UPS of 2–30-atom carbon clusters: Chains and rings. *Chemical Physics Letters*, 144(5-6):431–436, May 1988. doi:10.1016/0009-2614(88)87291-9.
- [8] Mireille Leleyter and Pierre Joyes. Secondary emission of molecular ions from light-element targets. *Radiation Effects*, 18(1-2):105–109, January 1973. doi:10.1080/00337577308234724.
- [9] M. Leleyter and P. Joyes. Étude expérimentale et théorique de l'émission secondaire d'ions moléculaires. cas des éléments du groupe IV-B. *Journal de Physique*, 36(5):343–355, May 1975. doi:10.1051/jphys:01975003605034300.
- [10] Mireille LELEYTER and Pierre JOYES. Mise en évidence de propriétés électroniques de petits agrégats d'atomes par émission ionique secondaire. *Le Journal de Physique Colloques*, 38(C2):C2-11–C2-17, July 1977. doi:10.1051/jphyscol:1977203.
- [11] P. Joyes and M. Leleyter. Etude théorique des alternances pair-impair dans les propriétés des amas C_n , C_n^+ et C_n^- linéaires. *Journal de Physique*, 45(10):1681–

- 1688, October 1984. doi:10.1051/jphys:0198400450100168100.
- [12] Kiyoshi Chiba, Takanao Akamatsu, and Masaaki Kawamura. Intensity variation dependence of secondary ion emission of carbon clusters from graphite, diamond-like carbon and diamond surfaces on number of carbon atoms. *Chemical Physics Letters*, 419(4-6):506–510, February 2006. doi:10.1016/j.cplett.2005.12.032.
- [13] R. Middleton and Charles T. Adams. A close to universal negative ion source. *Nuclear Instruments and Methods*, 118(2):329–336, June 1974. doi:10.1016/0029-554x(74)90634-x.
- [14] R. Middleton. A versatile high intensity negative ion source. *Nuclear Instruments and Methods in Physics Research*, 214(2-3):139–150, September 1983. doi:10.1016/0167-5087(83)90580-x.
- [15] Roy Middleton. A negative ion cookbook. Technical report, University of Pennsylvania, February 1990. URL: <https://www.pelletron.com/cookbook.pdf>.
- [16] L. M. Branscomb and B. E. J. Pagel. Atomic and molecular negative ions in stellar atmospheres. *Monthly Notices of the Royal Astronomical Society*, 118(3):258–270, June 1958. doi:10.1093/mnras/118.3.258.
- [17] M. S. Vardya. Role of negative ions in late-type stars. *Memoirs of the Royal Astronomical Society*, 71(1):249–269, 1967. URL: <http://adsabs.harvard.edu/abs/1967MmRAS..71..249V>.
- [18] Theodore Fay and Hollis R. Johnson. A search for C_2^- in spectra of HD 201626 and the sun. *Publications of the Astronomical Society of the Pacific*, 84:284, April 1972. doi:10.1086/129284.
- [19] M.S. Vardya and K.S.Krishna Swamy. Can lines of C_2^- be observed in carbon stars? *Chemical Physics Letters*, 73(3):616–617, August 1980. doi:10.1016/0009-2614(80)80730-5.
- [20] George Wallerstein. A search for C_2^- features in the hydrogen-poor carbon star hd 182040. *Astronomy and Astrophysics*, 105(1):219–220, January 1982. URL: <https://ui.adsabs.harvard.edu/abs/1982A%26A...105..219W>.
- [21] Philip C. Keenan. The spectra of CH stars. *The Astrophysical Journal*, 96:101, July 1942. doi:10.1086/144435.
- [22] George Wallerstein and Jesse L. Greenstein. The chemical composition of two CH stars, HD 26 and HD 201626. *The Astrophysical Journal*, 139:1163, May 1964. doi:10.1086/147858.
- [23] J. H. Goebel, J. D. Bregman, D. M. Cooper, D. Goorvitch, S. R. Langhoff, and F. C. Witteborn. The C_2H , C_2 , and CN electronic absorption bands in the carbon star HD 19557. *Astrophysical Journal*, 270:190, July 1983. doi:10.1086/161110.
- [24] Tim Kendall, Nicolas Mauron, June McCombie, and Peter Sarre. Probing the IRC+10 ° 216 circumstellar envelope using spectroscopic observations of background stars. *Astrophysics and Space Science*, 289(3/4):203–206, January 2004. doi:10.1023/b:astr.0000014943.39725.26.
- [25] V. G. Klochkova, R. Szczerba, and V. E. Panchuk. Optical spectrum of the infrared source IRAS 23304+6147. *Astronomy Letters*, 26(2):88–103, February 2000. doi:10.1134/1.20372.
- [26] M. R. Schmidt, L. Začs, M. Pućcka, and R. Szczerba. The excitation of cir-

- cumstellar C_2 in carbon-rich post-AGB object IRAS 22272+5435. *Astronomy & Astrophysics*, 556:A46, July 2013. doi:10.1051/0004-6361/201220808.
- [27] P. Swings and L. Rosenfeld. Considerations regarding interstellar molecules. *The Astrophysical Journal*, 86:483–486, November 1937. doi:10.1086/143880.
- [28] L. M. Hobbs. Interstellar C_2 molecules toward ζ persei. *Astrophysical Journal*, 232:L175, September 1979. doi:10.1086/183059.
- [29] Ewine F. van Dishoeck and Tim de Zeeuw. Observations of interstellar C_2 toward χ oph, HD 154368, 147889 and 149404. *Monthly Notices of the Royal Astronomical Society*, 206(2):383–406, January 1984. doi:10.1093/mnras/206.2.383.
- [30] S. R. Federman, C. J. Strom, D. L. Lambert, Jason A. Cardelli, V. V. Smith, and C. L. Joseph. Chemical transitions for interstellar C_2 and CN in cloud envelopes. *The Astrophysical Journal*, 424:772, April 1994. doi:10.1086/173930.
- [31] J. A. Thorburn, L. M. Hobbs, B. J. McCall, T. Oka, D. E. Welty, S. D. Friedman, T. P. Snow, P. Sonnentrucker, and D. G. York. Some diffuse interstellar bands related to interstellar C_2 molecules. *The Astrophysical Journal*, 584(1):339–356, February 2003. doi:10.1086/345665.
- [32] G. A. Galazutdinov, P. Gnaciński, Inwoo Han, Byeong-Cheol Lee, Kang-Min Kim, and J. Krelowski. On the diffuse bands related to the C_2 interstellar molecule. *Astronomy & Astrophysics*, 447(2):589–595, February 2006. doi:10.1051/0004-6361:20053410.
- [33] P. Sonnentrucker, D. E. Welty, J. A. Thorburn, and D. G. York. Abundances and behavior of ^{12}CO , ^{13}CO , and C_2 in translucent sight lines. *The Astrophysical Journal Supplement Series*, 168(1):58–99, January 2007. doi:10.1086/508687.
- [34] Daniel E. Welty, J. Christopher Howk, Nicolas Lehner, and John H. Black. Detection of interstellar C_2 and C_3 in the small magellanic cloud. *Monthly Notices of the Royal Astronomical Society*, 428(2):1107–1115, October 2012. doi:10.1093/mnras/sts093.
- [35] P.J. Sarre. On the possible detection of negative ions in the interstellar medium. *Journal de Chimie Physique et de Physico-Chimie Biologique*, 77:769–771, May 1980. doi:10.1051/jcp/1980770769.
- [36] Svatopluk Civiš, Yukio Hosaki, Eriko Kagi, Hideyuki Izumiura, Kenshi Yanagisawa, Tereza Šedivcová, and Kentarou Kawaguchi. Search for C_2^- in diffuse clouds. *Publications of the Astronomical Society of Japan*, 57(4):605–609, August 2005. doi:10.1093/pasj/57.4.605.
- [37] KI Churyumov, GF Chernyi, and AI Shapovalova. Discovery of emission from the negative carbon ion C_2^- in comet scorichenko-george (1990 vi). *Astronomy Letters*, 19:332–334, September 1993. URL: <https://ui.adsabs.harvard.edu/abs/1993AstL...19..332C>.
- [38] Klim I. Churyumov, Igor V. Luk'yanyk, Alexei A. Berezhnoi, Vahram H. Chavushyan, Lourdes S. Sandoval, and Alejandro A. Palma. *Earth, Moon, and Planets*, 90(1/4):361–368, 2002. doi:10.1023/a:1021586401331.
- [39] E. Picazzio, A.A. de Almeida, S.M. Andrievskii, K.I. Churyumov, and I.V. Luk'yanyk. A high spectral resolution atlas and catalogue of emission lines of the comet C/2000 WM1 (LINEAR). *Advances in Space Research*, 39(3):462–467,

- January 2007. doi:10.1016/j.asr.2003.06.048.
- [40] A. Palma, L. Sandoval, K. Churyumov, V. Chavushyan, and A. Berezhnoy. Franck-condon factors for molecules observed in comets. *International Journal of Quantum Chemistry*, 107(14):2650–2653, 2007. doi:10.1002/qua.21467.
- [41] William Huggins. Aus einem schreiben des herrn William Huggins an den herausgeber. *Astronomische Nachrichten*, 71(24):382–384, 1868. doi:10.1002/asna.18680712405.
- [42] P. Swings. Spectra of comets. *Publications of the Astronomical Society of the Pacific*, 54:123, June 1942. doi:10.1086/125418.
- [43] Gy. M. Szabó, L. L. Kiss, K. Sárneczky, and K. Sziládi. Spectrophotometry and structural analysis of 5 comets. *Astronomy & Astrophysics*, 384(2):702–710, March 2002. doi:10.1051/0004-6361:20020023.
- [44] Pauline Yzombard, Mehdi Hamamda, Sebastian Gerber, Michael Doser, and Daniel Comparat. Laser cooling of molecular anions. *Physical Review Letters*, 114(21):213001, May 2015. doi:10.1103/physrevlett.114.213001.
- [45] J.U. Andersen, C. Brink, P. Hvelplund, M.O. Larsson, and H. Shen. Carbon clusters in a storage ring. *Zeitschrift für Physik D Atoms, Molecules and Clusters*, 40(1):365, 1997. doi:10.1007/s004600050229.
- [46] H. B. Pedersen, C. Brink, L. H. Andersen, N. Bjerre, P. Hvelplund, D. Kella, and H. Shen. Experimental investigation of radiative lifetimes of vibrational levels at the electronic ground state of C_2^- . *The Journal of Chemical Physics*, 109(14):5849–5855, October 1998. doi:10.1063/1.477207.
- [47] T Takao, S Jinno, K Hanada, M Goto, K Oshikiri, K Okuno, H Tanuma, T Azuma, and H Shiromaru. Storage of negative carbon ions in an electrostatic ring. *Journal of Physics: Conference Series*, 88:012044, November 2007. doi:10.1088/1742-6596/88/1/012044.
- [48] N. Kono, R. Paul, E. K. Anderson, M. Gatchell, H. Zettergren, and H. T. Schmidt. Spontaneous decay of highly excited C_2^- : electron emission versus fragmentation. In *The 32nd International Conference on Photonic, Electronic and Atomic Collisions (ViCPEAC 2021)*, page 175, July 2021. URL: https://icpeac2021.ca/abstracts/ViCPEAC2021_Abstract_Book-PUBLIC.pdf.
- [49] A. Naaman, K. G. Bhushan, H. B. Pedersen, N. Altstein, O. Heber, M. L. Rappaport, R. Moalem, and D. Zajfman. Metastable states of negative carbon clusters: C_n^- , $n = 2-6$. *The Journal of Chemical Physics*, 113(11):4662–4667, September 2000. doi:10.1063/1.1286978.
- [50] Jurgen Barsuhn. Nonempirical calculations on the electronic spectrum of the molecular ion C_2^- . *Journal of Physics B: Atomic and Molecular Physics*, 7(1):155–162, January 1974. doi:10.1088/0022-3700/7/1/025.
- [51] Poul W. Thulstrup and Erik W. Thulstrup. A theoretical investigation of the low-lying states of the C_2^- ion. *Chemical Physics Letters*, 26(1):144–148, May 1974. doi:10.1016/0009-2614(74)89105-0.
- [52] Monika Zeitz, Sigrid D. Peyerimhoff, and Robert J. Buenker. A theoretical study of the bound electronic states of the C_2^- negative ion. *Chemical Physics Letters*, 64(2):243–249, July 1979. doi:10.1016/0009-2614(79)80505-9.
- [53] Gabriela Halmová, J D Gorfinkiel, and Jonathan Tennyson. Low-energy electron collisions with C_2 using the R-matrix method. *Journal of Physics*

- B: Atomic, Molecular and Optical Physics*, 39(12):2849–2860, June 2006. doi: 10.1088/0953-4075/39/12/018.
- [54] Gabriela Halmová. *R-matrix calculations of electron-molecule collisions with C₂ and C₂⁻*. PhD thesis, University of London, January 2008. URL: <http://discovery.ucl.ac.uk/1446444/>.
- [55] G. Herzberg and A. Lagerqvist. A new spectrum associated with diatomic carbon. *Canadian Journal of Physics*, 46(21):2363–2373, November 1968. doi: 10.1139/p68-596.
- [56] V. E. Bondybey and L. E. Brus. Photophysics of C₂⁻ (*B*²Σ_u⁺) in rare gas lattices: Vibrational relaxation through intermediate *a*⁴Σ_u⁺ levels. *The Journal of Chemical Physics*, 63(5):2223–2231, September 1975. doi: 10.1063/1.431605.
- [57] Y. Nakano, Y. Enomoto, T. Masunaga, S. Menk, P. Bertier, and T. Azuma. Design and commissioning of the RIKEN cryogenic electrostatic ring (RICE). *Review of Scientific Instruments*, 88(3):033110, March 2017. doi: 10.1063/1.4978454.
- [58] Sason Shaik, David Danovich, Wei Wu, Peifeng Su, Henry S. Rzepa, and Philippe C. Hiberty. Quadruple bonding in C₂ and analogous eight-valence electron species. *Nature Chemistry*, 4(3):195–200, January 2012. doi: 10.1038/nchem.1263.
- [59] Jon M. Matxain, Fernando Ruipérez, Ivan Infante, Xabier Lopez, Jesus M. Ugalde, Gabriel Merino, and Mario Piris. Communication: Chemical bonding in carbon dimer isovalent series from the natural orbital functional theory perspective. *The Journal of Chemical Physics*, 138(15):151102, April 2013. doi: 10.1063/1.4802585.
- [60] David Danovich, Philippe C. Hiberty, Wei Wu, Henry S. Rzepa, and Sason Shaik. The nature of the fourth bond in the ground state of C₂: The quadruple bond conundrum. *Chemistry — A European Journal*, 20(21):6220–6232, April 2014. doi: 10.1002/chem.201400356.
- [61] Jörg Grunenberg. Comment on “the nature of the fourth bond in the ground state of C₂: The quadruple bond conundrum”. *Chemistry — A European Journal*, 21(47):17126–17126, October 2015. doi: 10.1002/chem.201500130.
- [62] Sason Shaik, David Danovich, and Philippe C. Hiberty. Response to the comment by j. grunenberg on “the nature of the fourth bond in the ground state of C₂: The quadruple bond conundrum”. *Chemistry — A European Journal*, 21(47):17127–17128, October 2015. doi: 10.1002/chem.201503882.
- [63] B. A. Laws, S. T. Gibson, B. R. Lewis, and R. W. Field. The dicarbon bonding puzzle viewed with photoelectron imaging. *Nature Communications*, 10(1):5199, November 2019. doi: 10.1038/s41467-019-13039-y.
- [64] Kazunori Miyamoto, Shodai Narita, Yui Masumoto, Takahiro Hashishin, Taisei Osawa, Mutsumi Kimura, Masahito Ochiai, and Masanobu Uchiyama. Room-temperature chemical synthesis of C₂. *Nature Communications*, 11(1):2134, May 2020. doi: 10.1038/s41467-020-16025-x.
- [65] Jon T Hougen. The calculation of rotational energy levels and rotational line intensities in diatomic molecules. Technical report, 1970. doi: 10.6028/nbs.mono.115.
- [66] Jon T. Hougen. Classification of rotational energy levels for symmetric-top

- molecules. *The Journal of Chemical Physics*, 37(7):1433–1441, October 1962. doi : 10.1063/1.1733301.
- [67] Jon T. Hougen. Classification of rotational energy levels. II. *The Journal of Chemical Physics*, 39(2):358–365, July 1963. doi : 10.1063/1.1734253.
- [68] Laura K McKemmish, Anna-Maree Syme, Jasmin Borsovszky, Sergei N Yurchenko, Jonathan Tennyson, Tibor Furtenbacher, and Attila G Császár. An update to the MARVEL data set and ExoMol line list for $^{12}\text{C}_2$. *Monthly Notices of the Royal Astronomical Society*, 497(1):1081–1097, July 2020. doi : 10.1093/mnras/staa1954.
- [69] William Swan. XXIX.—on the prismatic spectra of the flames of compounds of carbon and hydrogen. *Transactions of the Royal Society of Edinburgh*, 21(3):411–429, 1857. doi : 10.1017/s0080456800032233.
- [70] John G. Phillips. A new band system of the C_2 molecule. *The Astrophysical Journal*, 107:389, May 1948. doi : 10.1086/145023.
- [71] Niccolò Bigagli, Daniel W. Savin, and Sebastian Will. Laser cooling scheme for the carbon dimer ($^{12}\text{C}_2$). *Physical Review A*, 105(5), may 2022. doi : 10.1103/physreva.105.1051301.
- [72] Philip M. Morse. Diatomic molecules according to the wave mechanics. II. vibrational levels. *Physical Review*, 34(1):57–64, July 1929. doi : 10.1103/physrev.34.57.
- [73] E. K. Anderson, A. F. Schmidt-May, P. K. Najeeb, G. Eklund, K. C. Chartkunchand, S. Rosén, Å. Larson, K. Hansen, H. Cederquist, H. Zettergren, and H. T. Schmidt. Spontaneous electron emission from hot silver dimer anions: Breakdown of the born-oppenheimer approximation. *Physical Review Letters*, 124(17):173001, April 2020. doi : 10.1103/physrevlett.124.173001.
- [74] J. L. Dunham. The energy levels of a rotating vibrator. *Physical Review*, 41(6):721–731, September 1932. doi : 10.1103/physrev.41.721.
- [75] Ragnar Rydberg. Graphische darstellung einiger bandenspektroskopischer ergebnisse. *Zeitschrift für Physik*, 73(5-6):376–385, May 1932. doi : 10.1007/bf01341146.
- [76] O. Klein. Zur berechnung von potentialkurven für zweiatomige moleküle mit hilfe von spektraltermen. *Zeitschrift für Physik*, 76(3-4):226–235, March 1932. doi : 10.1007/bf01341814.
- [77] A L G Rees. The calculation of potential-energy curves from band-spectroscopic data. *Proceedings of the Physical Society*, 59(6):998–1008, November 1947. doi : 10.1088/0959-5309/59/6/310.
- [78] Robert J. Le Roy. LEVEL: A computer program for solving the radial schrödinger equation for bound and quasibound levels. *Journal of Quantitative Spectroscopy and Radiative Transfer*, 186:167–178, January 2017. doi : 10.1016/j.jqsrt.2016.05.028.
- [79] William H. Miller. Additional WKB inversion relations for bound-state and scattering problems. *The Journal of Chemical Physics*, 54(10):4174–4177, May 1971. doi : 10.1063/1.1674655.
- [80] Ellis E. Whiting and Ralph W. Nicholls. Reinvestigation of rotational-line intensity factors in diatomic spectra. *The Astrophysical Journal Supplement Series*,

- 27:1, January 1974. doi:10.1086/190286.
- [81] Ellis E. Whiting, Aert Schadee, Jeremy B. Tatum, Jon T. Hougen, and Ralph W. Nicholls. Recommended conventions for defining transition moments and intensity factors in diatomic molecular spectra. *Journal of Molecular Spectroscopy*, 80(2):249–256, April 1980. doi:10.1016/0022-2852(80)90137-x.
- [82] Gerhard Herzberg. *Molecular spectra and molecular structure, I. Spectra of diatomic molecules*. Van Nostrand company, Inc., 1950.
- [83] Annie Hansson and James K.G. Watson. A comment on hönl-london factors. *Journal of Molecular Spectroscopy*, 233(2):169–173, October 2005. doi:10.1016/j.jms.2005.06.009.
- [84] Sumner P. Davis, John G. Phillips, M. L. P. Rao, and Mark C. Abrams. Infrared bands of the C₂ phillips system. *Journal of the Optical Society of America B*, 5(10):2280, October 1988. doi:10.1364/josab.5.002280.
- [85] P. L. Jones, R. D. Mead, B. E. Kohler, S. D. Rosner, and W. C. Lineberger. Photodetachment spectroscopy of C₂⁻ autodetaching resonances. *The Journal of Chemical Physics*, 73(9):4419–4432, November 1980. doi:10.1063/1.440678.
- [86] F. Hund. Allgemeine quantenmechanik des atom- und molekelbaues. In H. Bethe, F. Hund, N. F. Mott, W. Pauli, A. Rubinowicz, G. Wentzel, and A. Smekal, editors, *Quantentheorie*, Handbuch der Physik, pages 561–694. Springer Berlin Heidelberg, 1933. doi:10.1007/978-3-642-52619-0_4.
- [87] L. D. Landau and E. M. Lifshitz. *Quantum Mechanics: Non-Relativistic Theory*, volume 3 of *Course of Theoretical Physics*. Pergamon Press, 3rd edition edition, 1977.
- [88] Peter F. Bernath. *Spectra of Atoms and Molecules*. Oxford University Press, 4th edition edition, 2020.
- [89] Robert S. Mulliken. The interpretation of band spectra. parts I, IIa, IIb. *Reviews of Modern Physics*, 2(1):60–115, January 1930. doi:10.1103/revmodphys.2.60.
- [90] Alan Carrington, Christopher H. Pyne, Andrew M. Shaw, Susie M. Taylor, Jeremy M. Hutson, and Mark M. Law. Microwave spectroscopy and interaction potential of the long-range He ··· Kr⁺ ion: An example of hund’s case (e). *The Journal of Chemical Physics*, 105(19):8602–8614, November 1996. doi:10.1063/1.472999.
- [91] L.H. Andersen, T. Andersen, and P. Hvelplund. Studies of negative ions in storage rings. In Benjamin Bederson and Herbert Walther, editors, *Advances In Atomic, Molecular, and Optical Physics*, volume 38, pages 155–191. Academic Press, 1998. doi:10.1016/s1049-250x(08)60052-x.
- [92] Jack Simons. Molecular anions. *The Journal of Physical Chemistry A*, 112(29):6401–6511, July 2008. doi:10.1021/jp711490b.
- [93] Gerhard Herzberg. *The spectra and structures of simple free radicals: an introduction to molecular spectroscopy*. Cornell University Press, 1971.
- [94] K. P. Huber and G. Herzberg. *Molecular Spectra and Molecular Structure, IV. Constants of diatomic molecules*. Van Nostrand Reinhold, Inc., 1979. doi:10.1007/978-1-4757-0961-2.
- [95] William Weltner and Richard J. Van Zee. Carbon molecules, ions, and clusters. *Chemical Reviews*, 89(8):1713–1747, December 1989. doi:10.1021/cr00098a005.

- [96] David R. Bates. Negative ions: Structure and spectra. In *Advances In Atomic, Molecular, and Optical Physics*, pages 1–80. Elsevier, 1990. doi:10.1016/s1049-250x(08)60148-2.
- [97] Takeshi Oka. Infrared spectroscopy of carbo-ions. *Philosophical Transactions of the Royal Society of London. Series A, Mathematical and Physical Sciences*, 324(1578):81–95, January 1988. doi:10.1098/rsta.1988.0002.
- [98] Brent D. Rehfuss, Di-Jia Liu, Bianca M. Dinelli, Mary-Frances Jagod, Wing C. Ho, Mark W. Crofton, and Takeshi Oka. Infrared spectroscopy of carbo-ions. IV. the $A^2\Pi_u - X^2\Sigma_g^+$ electronic transition of C_2^- . *The Journal of Chemical Physics*, 89(1):129–137, July 1988. doi:10.1063/1.455731.
- [99] Roy D. Mead, U. Hefter, P. A. Schulz, and W. C. Lineberger. Ultrahigh resolution spectroscopy of C_2^- : The $A^2\Pi_u$ state characterized by deperturbation methods. *The Journal of Chemical Physics*, 82(4):1723–1731, February 1985. doi:10.1063/1.448960.
- [100] C. Amiot, J. Chauville, and J.-P. Maillard. New analysis of the C_2 ballik-ramsay system from flame emission spectra. *Journal of Molecular Spectroscopy*, 75(1):19–40, April 1979. doi:10.1016/0022-2852(79)90143-7.
- [101] Kent M. Ervin and W. C. Lineberger. Photoelectron spectra of C_2^- and C_2H^- . *The Journal of Physical Chemistry*, 95(3):1167–1177, February 1991. doi:10.1021/j100156a026.
- [102] Jonathan C. Rienstra-Kiracofe, Gregory S. Tschumper, Henry F. Schaefer, Sreela Nandi, and G. Barney Ellison. Atomic and molecular electron affinities: Photoelectron experiments and theoretical computations. *Chemical Reviews*, 102(1):231–282, January 2002. doi:10.1021/cr990044u.
- [103] John D. Watts and Rodney J. Bartlett. Coupled-cluster calculations on the C_2 molecule and the C_2^+ and C_2^- molecular ions. *The Journal of Chemical Physics*, 96(8):6073–6084, April 1992. doi:10.1063/1.462649.
- [104] Shih-I Lu. Electron affinities with diffusion quantum monte carlo for C_2 and BO molecules. *The Journal of Chemical Physics*, 121(21):10495–10497, December 2004. doi:10.1063/1.1811610.
- [105] L. v. Trepka and H. Neuert. Über die entstehung von negativen ionen aus einigen kohlenwasserstoffen und alkoholen durch elektronenstoß. *Zeitschrift für Naturforschung A*, 18(12):1295–1303, December 1963. doi:10.1515/zna-1963-1208.
- [106] D. Feldmann. Photoablösung von elektronen bei einigen stabilen negativen ionen. *Zeitschrift für Naturforschung A*, 25(5):621–626, May 1970. doi:10.1515/zna-1970-0508.
- [107] R. Loch and J. Momigny. Mass spectrometric determination of the electronaffinities of radicals. *Chemical Physics Letters*, 6(4):273–276, August 1970. doi:10.1016/0009-2614(70)85072-2.
- [108] D. W. Arnold, S. E. Bradforth, T. N. Kitsopoulos, and D. M. Neumark. Vibrationally resolved spectra of $C_2 - C_{11}$ by anion photoelectron spectroscopy. *The Journal of Chemical Physics*, 95(12):8753–8764, December 1991. doi:10.1063/1.461211.
- [109] L S Cederbaum, W Domcke, and W von Niessen. Many-body calculation of

- electron affinities: C_2 and a prediction for P_2 . *Journal of Physics B: Atomic and Molecular Physics*, 10(14):2963–2970, October 1977. doi:10.1088/0022-3700/10/14/028.
- [110] M. Dupuis and B. Liu. Theoretical study of C_2 and C_2^- . *The Journal of Chemical Physics*, 73(1):337–342, July 1980. doi:10.1063/1.439879.
- [111] H Gollisch. Density matrix calculations for molecules and clusters II. first-row diatomic molecules. *Journal of Physics B: Atomic and Molecular Physics*, 14(23):4451–4468, December 1981. doi:10.1088/0022-3700/14/23/010.
- [112] Juan J. Novoa and Fernando Mota. Accurate electron affinities of several diatomic and triatomic molecules. *Chemical Physics Letters*, 123(5):399–401, January 1986. doi:10.1016/0009-2614(86)80030-6.
- [113] Jeffrey A. Nichols and Jack Simons. Theoretical study of C_2 and C_2^- : $X^1\Sigma_g^+$, $a^3\Pi_u$, $X^2\Sigma_g^+$, and $B^2\Sigma_u^+$ potentials. *The Journal of Chemical Physics*, 86(12):6972–6981, June 1987. doi:10.1063/1.452345.
- [114] J. A. Sordo. Performance of CCSDT for first row AB/AB⁻ diatomics: Dissociation energies and electron affinities. *The Journal of Chemical Physics*, 114(5):1974–1980, February 2001. doi:10.1063/1.1335617.
- [115] Monika Musiał and Rodney J. Bartlett. Equation-of-motion coupled cluster method with full inclusion of connected triple excitations for electron-attached states: EA-EOM-CCSDT. *The Journal of Chemical Physics*, 119(4):1901–1908, July 2003. doi:10.1063/1.1584657.
- [116] David Feller. Application of a convergent, composite coupled cluster approach to bound state, adiabatic electron affinities in atoms and small molecules. *The Journal of Chemical Physics*, 144(1):014105, January 2016. doi:10.1063/1.4939184.
- [117] Sahil Gulania, Thomas-C. Jagau, and Anna I. Krylov. EOM-CC guide to fock-space travel: the C_2 edition. *Faraday Discussions*, 217:514–532, 2019. doi:10.1039/c8fd00185e.
- [118] W. S. Cathro and J. C. Mackie. Oscillator strength of the C_2^- $B^2\Sigma-X^2\Sigma$ transition: a shock-tube determination. *Journal of the Chemical Society, Faraday Transactions 2: Molecular and Chemical Physics*, 69(0):237–245, 1973. doi:10.1039/f29736900237.
- [119] R. D. Mead, P. A. Schulz, C. S. Feigerle, and W. C. Lineberger. Laser spectroscopy of negative ion beams. *IEEE Transactions on Nuclear Science*, 28(2):1194–1197, 1981. doi:10.1109/tns.1981.4331377.
- [120] W.C. Lineberger and T.A. Patterson. Two photon photodetachment spectroscopy: The C_2^- $^2\Sigma$ states. *Chemical Physics Letters*, 13(1):40–44, February 1972. doi:10.1016/0009-2614(72)80037-x.
- [121] Patrick Lawrence Jones. *Experimental studies of autodetachment in diatomic carbon negative ions*. PhD thesis, University of Colorado, March 1980. URL: <http://libraries.colorado.edu/record=b1543319~S3>.
- [122] Masakazu Nakajima. Observation of the $X^2\Sigma_g^+$ ($v = 4-6$) levels of C_2^- . *Journal of Molecular Spectroscopy*, 331:106–108, January 2017. doi:10.1016/j.jms.2016.11.002.
- [123] Esther de Beer, Yuexing Zhao, Ivan Yourshaw, and Daniel M. Neumark.

- Stimulated raman pumping of C_2^- probed via resonant two-photon detachment. *Chemical Physics Letters*, 244(5-6):400–406, October 1995. doi:10.1016/0009-2614(95)00967-9.
- [124] Arthur E. Bragg, Roland Wester, Alison V. Davis, Aster Kammrath, and Daniel M. Neumark. Excited-state detachment dynamics and rotational coherences of C_2^- via time-resolved photoelectron imaging. *Chemical Physics Letters*, 376(5-6):767–775, July 2003. doi:10.1016/s0009-2614(03)01060-1.
- [125] P. Royen and M. Zackrisson. Spin-splitting analysis of the $B^2\Sigma_u^+$ ($v = 0$) state of C_2^- , using velocity modulation laser spectroscopy. *Journal of Molecular Spectroscopy*, 155(2):427–429, October 1992. doi:10.1016/0022-2852(92)90534-u.
- [126] Markus Nötzold, Robert Wild, Christine Lochmann, and Roland Wester. Spectroscopy and ion thermometry of C_2^- using laser-cooling transitions. *Physical Review A*, 106(2), August 2022. doi:10.1103/physreva.106.023111.
- [127] Yu Shan-Shan, Yang Xiao-Hua, Li Ben-Xia, Kaniki Kakule, Wu Sheng-Hai, Guo Ying-Chun, Liu Yu-Yan, and Chen Yang-Qin. Study of hot bands in the $B^2\Sigma_u^+ - X^2\Sigma_g^+$ system of C_2^- anion. *Chinese Physics*, 12(7):745–749, June 2003. doi:10.1088/1009-1963/12/7/308.
- [128] Ming Luo, Zhiyi Bi, Peipei Cai, Rongjun Wang, Xiaohua Yang, Yangqin Chen, and Longsheng Ma. Optical heterodyne magnetic rotation enhanced velocity modulation spectroscopy: A sensitive absorption-based scheme for paramagnetic molecular ions. *Review of Scientific Instruments*, 72(6):2691–2696, June 2001. doi:10.1063/1.1376141.
- [129] Jie Ma, James C. Richley, Michael N. R. Ashfold, and Yuri A. Mankelevich. Probing the plasma chemistry in a microwave reactor used for diamond chemical vapor deposition by cavity ring down spectroscopy. *Journal of Applied Physics*, 104(10):103305, November 2008. doi:10.1063/1.3021095.
- [130] Dolphus E. Milligan and Marilyn E. Jacox. Studies of the photoproduction of electrons in inert solid matrices. the electronic spectrum of the species C_2^- . *The Journal of Chemical Physics*, 51(5):1952–1955, September 1969. doi:10.1063/1.1672283.
- [131] R. P. Frosch. C_2 and C_2^- spectra produced by the x irradiation of acetylene in rare-gas matrices. *The Journal of Chemical Physics*, 54(6):2660–2666, March 1971. doi:10.1063/1.1675229.
- [132] W. R. M. Graham, K. I. Dismuke, and W. Weltner. ESR and optical spectra of C_2^- in various ion pairs trapped at 4°K in solid argon. *The Journal of Chemical Physics*, 61(11):4793–4799, December 1974. doi:10.1063/1.1681804.
- [133] L. E. Brus and V. E. Bondybey. Molecular ions and electron transport in rare gas lattices: C_2^- formation mechanism and $X^2\Sigma_g^+ \leftrightarrow B^2\Sigma_u^+$ spectroscopy. *The Journal of Chemical Physics*, 63(7):3123, 1975. doi:10.1063/1.431740.
- [134] R.I. Personov, E.I. Al'Shits, and L.A. Bykovskaya. The effect of fine structure appearance in laser-excited fluorescence spectra of organic compounds in solid solutions. *Optics Communications*, 6(2):169–173, October 1972. doi:10.1016/0030-4018(72)90220-9.
- [135] M. Rasanen, J.Y. Liu, T.P. Dzugas, and V.E. Bondybey. Matrix studies of the products of laser vaporization of graphite. *Chemical Physics Letters*, 142(5):308–

- 312, December 1987. doi:10.1016/0009-2614(87)85112-6.
- [136] H. E. Popkie and W. H. Henneker. Theoretical electronic transition probabilities in diatomic molecules II. 13-electron sequence. *The Journal of Chemical Physics*, 55(2):617–628, July 1971. doi:10.1063/1.1676128.
- [137] Paul E. Cade and Arnold C. Wahl. Hartree-fock-roothaan wavefunctions for diatomic molecules. *Atomic Data and Nuclear Data Tables*, 13(4):339–389, January 1974. doi:10.1016/0092-640x(74)90006-0.
- [138] Pavel Rosmus and Hans-Joachim Werner. Multireference-CI calculations of radiative transition probabilities in C_2^- . *The Journal of Chemical Physics*, 80(10):5085–5088, May 1984. doi:10.1063/1.446579.
- [139] P. Botschwina, S. Seeger, M. Mladenović, B. Schulz, M. Horn, S. Schmatz, J. Flügge, and R. Oswald. Quantum-chemical investigations of small molecular anions. *International Reviews in Physical Chemistry*, 14(2):169–204, September 1995. doi:10.1080/01442359509353308.
- [140] Pablo J. Bruna and Friedrich Grein. Ab initio study of the electron-spin magnetic moments (g-factors) of C_2^- , CSi^- , Si_2^- , LiC_2 , NaC_2 , and $LiSi_2$. *The Journal of Chemical Physics*, 112(24):10796–10805, June 2000. doi:10.1063/1.481723.
- [141] J. D. Gorfinkiel, A. Faure, S. Taioli, C. Piccarreta, G. Halmová, and J. Tennyson. Electron-molecule collisions at low and intermediate energies using the R-matrix method. *The European Physical Journal D*, 35(2):231–237, June 2005. doi:10.1140/epjd/e2005-00179-4.
- [142] T. Šedivcová and V. Špirko. Potential energy and transition dipole moment functions of C_2^- . *Molecular Physics*, 104(13-14):1999–2005, July 2006. doi:10.1080/00268970600662689.
- [143] Weixin Shi, Chuanliang Li, Huiyan Meng, Jilin Wei, Lunhua Deng, and Chuanlu Yang. Ab initio study of the low-lying electronic states of the C_2^- anion. *Computational and Theoretical Chemistry*, 1079:57–63, March 2016. doi:10.1016/j.comptc.2016.01.015.
- [144] Samuel Leutwyler, John P. Maier, and Liubomir Misev. Lifetimes of C_2^- in rotational levels of the $\tilde{B}^2\Sigma_u^+$ state in the gas phase. *Chemical Physics Letters*, 91(3):206–208, September 1982. doi:10.1016/0009-2614(82)83642-7.
- [145] Shimpei Iida, Susumu Kuma, Hajime Tanuma, Toshiyuki Azuma, and Haruo Shiromaru. State-selective observation of radiative cooling of vibrationally excited C_2^- . *The Journal of Physical Chemistry Letters*, 11(24):10526–10531, December 2020. doi:10.1021/acs.jpcllett.0c03196.
- [146] U. Hefter, Roy D. Mead, P. A. Schulz, and W. C. Lineberger. Ultrahigh-resolution study of autodetachment in C_2^- . *Physical Review A*, 28(3):1429–1439, September 1983. doi:10.1103/physreva.28.1429.
- [147] R Stensgaard. ASTRID — the Aarhus storage ring. *Physica Scripta*, T22:315–317, January 1988. doi:10.1088/0031-8949/1988/t22/051.
- [148] S.P. Møller. ASTRID — a storage ring for ions and electrons. In *Conference Record of the 1991 IEEE Particle Accelerator Conference*, pages 2811–2813. IEEE, May 1991. doi:10.1109/pac.1991.165111.
- [149] P. Tykesson, H. H. Andersen, and J. Heinemeier. Further investigations of ANIS (the aarhus negative ion source). *IEEE Transactions on Nuclear Science*,

- 23(2):1104–1108, April 1976. doi : 10.1109/tns.1976.4328414.
- [150] S. Jinno, T. Takao, Y. Omata, A. Satou, H. Tanuma, T. Azuma, H. Shiromaru, K. Okuno, N. Kobayashi, and I. Watanabe. TMU electrostatic ion storage ring designed for operation at liquid nitrogen temperature. *Nuclear Instruments and Methods in Physics Research Section A: Accelerators, Spectrometers, Detectors and Associated Equipment*, 532(1-2):477–482, October 2004. doi : 10.1016/j.nima.2004.06.070.
- [151] R. D. Thomas, H. T. Schmidt, G. Andler, M. Björkhage, M. Blom, L. Brännholm, E. Bäckström, H. Danared, S. Das, N. Haag, P. Halldén, F. Hellberg, A. I. S. Holm, H. A. B. Johansson, A. Källberg, G. Källersjö, M. Larsson, S. Leontein, L. Liljeby, P. Löfgren, B. Malm, S. Mannervik, M. Masuda, D. Misra, A. Orbán, A. Paál, P. Reinhed, K.-G. Rensfelt, S. Rosén, K. Schmidt, F. Seitz, A. Simonsson, J. Weimer, H. Zettergren, and H. Cederquist. The double electrostatic ion ring experiment: A unique cryogenic electrostatic storage ring for merged ion-beams studies. *Review of Scientific Instruments*, 82(6):065112, June 2011. doi : 10.1063/1.3602928.
- [152] H. T. Schmidt, R. D. Thomas, M. Gatchell, S. Rosén, P. Reinhed, P. Löfgren, L. Brännholm, M. Blom, M. Björkhage, E. Bäckström, J. D. Alexander, S. Leontein, D. Hanstorp, H. Zettergren, L. Liljeby, A. Källberg, A. Simonsson, F. Hellberg, S. Mannervik, M. Larsson, W. D. Geppert, K. G. Rensfelt, H. Danared, A. Paál, M. Masuda, P. Halldén, G. Andler, M. H. Stockett, T. Chen, G. Källersjö, J. Weimer, K. Hansen, H. Hartman, and H. Cederquist. First storage of ion beams in the double electrostatic ion-ring experiment: DESIREE. *Review of Scientific Instruments*, 84(5):055115, May 2013. doi : 10.1063/1.4807702.
- [153] Jürgen Michael Göck. *A novel approach for mid-infrared spectroscopy of large carbon systems and the nonthermal fragmentation process of diatomic anions*. PhD thesis, Ruprecht-Karls-Universität, Heidelberg, 2020. doi : 10.17617/2.3262723.
- [154] R. von Hahn, F. Berg, K. Blaum, J.R. Crespo Lopez-Urrutia, F. Fellenberger, M. Froese, M. Grieser, C. Krantz, K.-U. Kühnel, M. Lange, S. Menk, F. Laux, D.A. Orlov, R. Repnow, C.D. Schröter, A. Shornikov, T. Sieber, J. Ullrich, A. Wolf, M. Rappaport, and D. Zajfman. The electrostatic cryogenic storage ring CSR — mechanical concept and realization. *Nuclear Instruments and Methods in Physics Research Section B: Beam Interactions with Materials and Atoms*, 269(24):2871–2874, December 2011. doi : 10.1016/j.nimb.2011.04.033.
- [155] R. von Hahn, A. Becker, F. Berg, K. Blaum, C. Breitenfeldt, H. Fadil, F. Fellenberger, M. Froese, S. George, J. Göck, M. Grieser, F. Grussie, E. A. Guerin, O. Heber, P. Herwig, J. Karthein, C. Krantz, H. Kreckel, M. Lange, F. Laux, S. Lohmann, S. Menk, C. Meyer, P. M. Mishra, O. Novotný, A. P. O’Connor, D. A. Orlov, M. L. Rappaport, R. Repnow, S. Saurabh, S. Schippers, C. D. Schröter, D. Schwalm, L. Schweikhard, T. Sieber, A. Shornikov, K. Spruck, S. Sunil Kumar, J. Ullrich, X. Urbain, S. Vogel, P. Wilhelm, A. Wolf, and D. Zajfman. The cryogenic storage ring CSR. *Review of Scientific Instruments*, 87(6):063115, June 2016. doi : 10.1063/1.4953888.
- [156] Kaija Spruck, Arno Becker, Florian Fellenberger, Manfred Grieser, Robert von Hahn, Vincent Klinkhamer, Oldřich Novotný, Stefan Schippers, Stephen Vogel, Andreas Wolf, and Claude Krantz. An efficient, movable single-particle detec-

- tor for use in cryogenic ultra-high vacuum environments. *Review of Scientific Instruments*, 86(2):023303, February 2015. doi:10.1063/1.4907352.
- [157] J. Fedor, K. Hansen, J. U. Andersen, and P. Hvelplund. Nonthermal power law decay of metal dimer anions. *Physical Review Letters*, 94(11):113201, March 2005. doi:10.1103/physrevlett.94.113201.
- [158] W. Carl Lineberger. Once upon anion: A tale of photodetachment. *Annual Review of Physical Chemistry*, 64(1):21–36, April 2013. doi:10.1146/annurev-physchem-032511-143753.
- [159] Masatomi Iizawa, Susumu Kuma, Naoki Kimura, Kiattichart Chartkunchand, Sakumi Harayama, Toshiyuki Azuma, and Yuji Nakano. Photodetachment spectroscopy of highly excited C_2^- and their temporal evolution in the ion storage ring RICE. *Journal of the Physical Society of Japan*, 91(8), August 2022. doi:10.7566/jpsj.91.084302.
- [160] Hiroshi Tsuji, Junzo Ishikawa, Tetsuo Tomita, Takaaki Yoshihara, and Yasuhito Gotoh. Extraction of molecular negative-ion beams of CN from radio frequency plasma-sputter-type heavy negative ion source for negative-ion beam deposition. *Review of Scientific Instruments*, 69(2):884–886, February 1998. doi:10.1063/1.1148628.
- [161] S. Jinno, T. Takao, K. Hanada, M. Goto, K. Okuno, H. Tanuma, T. Azuma, and H. Shiromaru. Storage and mass-selective control of ions in an electrostatic ion storage ring. *Nuclear Instruments and Methods in Physics Research Section A: Accelerators, Spectrometers, Detectors and Associated Equipment*, 572(2):568–579, March 2007. doi:10.1016/j.nima.2006.11.043.
- [162] W. Arnold, P. Baumann, M. Blum, P. Brix, A. Friedrich, M. Grieser, D. Habs, E. Jaeschke, Dietrich Krämer, B. V. Kruchten, C. Martin, K. Matl, B. Povh, R. Repnow, A. Rudnik, H. Sailer, U. Schmidt-Rohr, Schuch, Markus Steck, E. Steffens, and C. A. Wiedner. The heidelberg heavy ion test storage ring TSR. In *13th International Conference on High-energy Accelerators*, pages 334–340, August 1986. URL: <https://inspirehep.net/literature/939447>.
- [163] P. Baumann, M. Blum, A. Friedrich, C. Geyer, M. Grieser, B. Holzer, E. Jaeschke, D. Krämer, C. Martin, K. Matl, R. Mayer, W. Ott, B. Povh, R. Repnow, M. Steck, E. Steffens, and W. Arnold. The heidelberg heavy ion test storage ring TSR. *Nuclear Instruments and Methods in Physics Research Section A: Accelerators, Spectrometers, Detectors and Associated Equipment*, 268(2-3):531–537, May 1988. doi:10.1016/0168-9002(88)90573-6.
- [164] P. Forck, M. Grieser, D. Habs, A. Lampert, R. Repnow, D. Schwalm, A. Wolf, and D. Zajfman. Dissociative recombination of cold HD^+ at the test storage ring. *Physical Review Letters*, 70(4):426–429, January 1993. doi:10.1103/physrevlett.70.426.
- [165] T. Tanabe, I. Katayama, N. Inoue, K. Chida, Y. Arakaki, T. Watanabe, M. Yoshizawa, S. Ohtani, and K. Noda. Dissociative recombination of HeH^+ at large center-of-mass energies. *Physical Review Letters*, 70(4):422–425, January 1993. doi:10.1103/physrevlett.70.422.
- [166] S.P. Møller. The Aarhus storage ring for ions and electrons ASTRID. In *Proceedings of International Conference on Particle Accelerators*, pages 1741–1743. IEEE, May 1993. doi:10.1109/pac.1993.309118.

- [167] L. H. Andersen, J. H. Posthumus, O. Vahtras, H. Ågren, N. Elander, A. Nunez, A. Scrinzi, M. Natiello, and M. Larsson. Very slow spontaneous dissociation of CO^{2+} observed by means of a heavy ion storage ring. *Physical Review Letters*, 71(12):1812–1815, September 1993. doi:10.1103/physrevlett.71.1812.
- [168] M. Larsson, H. Danared, J. R. Mowat, P. Sigray, G. Sundström, L. Broström, A. Filevich, A. Källberg, S. Mannervik, K. G. Rensfelt, and S. Datz. Direct high-energy neutral-channel dissociative recombination of cold H_3^+ in an ion storage ring. *Physical Review Letters*, 70(4):430–433, January 1993. doi:10.1103/physrevlett.70.430.
- [169] Søren Pape Møller. ELISA, and electrostatic storage ring for atomic physics. *Nuclear Instruments and Methods in Physics Research Section A: Accelerators, Spectrometers, Detectors and Associated Equipment*, 394(3):281–286, July 1997. doi:10.1016/s0168-9002(97)00673-6.
- [170] T Tanabe, K Chida, K Noda, and I Watanabe. An electrostatic storage ring for atomic and molecular science. *Nuclear Instruments and Methods in Physics Research Section A: Accelerators, Spectrometers, Detectors and Associated Equipment*, 482(3):595–605, April 2002. doi:10.1016/s0168-9002(01)01704-1.
- [171] J. Warbinek, D. Leimbach, D. Lu, K. Wendt, D. J. Pegg, A. Yurgens, D. Hanstorp, and J. Welander. A graphene-based neutral particle detector. *Applied Physics Letters*, 114(6):061902, February 2019. doi:10.1063/1.5080517.
- [172] F. Bonaccorso, Z. Sun, T. Hasan, and A. C. Ferrari. Graphene photonics and optoelectronics. *Nature Photonics*, 4(9):611–622, August 2010. doi:10.1038/nphoton.2010.186.
- [173] J. Bartl and M. Baranek. Emissivity of aluminium and its importance for radiometric measurement. *Measurement Science Review*, 4(3):31–36, 2004. URL: <https://www.measurement.sk/2004/S3/Bartl.pdf>.
- [174] Y. Nakano, R. Igosawa, S. Iida, S. Okada, M. Lindley, S. Menk, R. Nagaoka, T. Hashimoto, S. Yamada, T. Yamaguchi, S. Kuma, and T. Azuma. Status of the laser spectroscopy and merged-beam experiments at RICE. In *Proceedings of 10th International Conference on Nuclear Physics at Storage Rings (STORI'17)*, volume 35, page 011006. Journal of the Physical Society of Japan, June 2021. doi:10.7566/jpscp.35.011006.
- [175] Reed R. Corderman, P. C. Engelking, and W. C. Lineberger. Laser photoelectron spectrometry measurement of characteristic electronic and vibrational temperatures of sputtered negative ions. *Applied Physics Letters*, 36(7):533–535, April 1980. doi:10.1063/1.91569.
- [176] R R Corderman and W C Lineberger. Negative ion spectroscopy. *Annual Review of Physical Chemistry*, 30(1):347–378, October 1979. doi:10.1146/annurev.pc.30.100179.002023.
- [177] Christian Breitenfeldt, Klaus Blaum, Sebastian George, Jürgen Göck, Gregorio Guzmán-Ramírez, Jonas Karthein, Thomas Kolling, Michael Lange, Sebastian Menk, Christian Meyer, Jennifer Mohrbach, Gereon Niedner-Schatteburg, Dirk Schwalm, Lutz Schweikhard, and Andreas Wolf. Long-term monitoring of the internal energy distribution of isolated cluster systems. *Physical Review Letters*, 120(25):253001, June 2018. doi:10.1103/physrevlett.120.253001.

- [178] John S. Vogel. Neutral resonant ionization in the high-intensity cesium sputter source. *AIP Conference Proceedings*, 1515:89–98, February 2013. doi:10.1063/1.4792774.
- [179] John S. Vogel. Anion formation by neutral resonant ionization. *Nuclear Instruments and Methods in Physics Research Section B: Beam Interactions with Materials and Atoms*, 361:156–162, October 2015. doi:10.1016/j.nimb.2015.02.062.
- [180] J. S. Vogel. Anion formation in sputter ion sources by neutral resonant ionization. *Review of Scientific Instruments*, 87(2):02A504, February 2016. doi:10.1063/1.4934618.
- [181] C.P. Safvan, V.R. Bhardwaj, D. Mathur, and A.K. Gupta. Double detachment of electrons from C_2^- . *Chemical Physics Letters*, 259(3-4):415–419, September 1996. doi:10.1016/0009-2614(96)00776-2.
- [182] Gustav Eklund, Moa K. Kristiansson, K. C. Chartkunchand, Emma K. Anderson, Malcolm Simpson, Roland Wester, Henning T. Schmidt, Henning Zettergren, Henrik Cederquist, and Wolf D. Geppert. Experimental lifetime of the $a^1\delta$ electronically excited state of CH^- . *Physical Review Research*, 4(1):L012016, February 2022. doi:10.1103/physrevresearch.4.1012016.
- [183] Brett A. McGuire. 2018 census of interstellar, circumstellar, extragalactic, protoplanetary disk, and exoplanetary molecules. *The Astrophysical Journal Supplement Series*, 239(2):17, November 2018. doi:10.3847/1538-4365/aae5d2.
- [184] Holger S. P. Müller, Arnaud Belloche, Li-Hong Xu, Ronald M. Lees, Robin T. Garrod, Adam Walters, Jennifer van Wijngaarden, Frank Lewen, Stephan Schlemmer, and Karl M. Menten. Exploring molecular complexity with ALMA (EMoCA): Alkanethiols and alkanols in sagittarius B2(N2). *Astronomy & Astrophysics*, 587:A92, feb 2016. doi:10.1051/0004-6361/201527470.
- [185] Karin I. Öberg, Viviana V. Guzmán, Kenji Furuya, Chunhua Qi, Yuri Aikawa, Sean M. Andrews, Ryan Loomis, and David J. Wilner. The comet-like composition of a protoplanetary disk as revealed by complex cyanides. *Nature*, 520(7546):198–201, April 2015. doi:10.1038/nature14276.
- [186] Takafumi Ootsubo, Hideyo Kawakita, Yoshiharu Shinnaka, Jun ichi Watanabe, and Mitsuhiko Honda. Unidentified infrared emission features in mid-infrared spectrum of comet 21p/giacobini-zinner. *Icarus*, 338:113450, March 2020. doi:10.1016/j.icarus.2019.113450.
- [187] M Iizawa, S Iida, S Kuma, T Azuma, and Y Nakano. Photodetachment of negative ion beams for the ion-neutral merged-beam experiments at RICE. *Journal of Physics: Conference Series*, 1412(12):122006, January 2020. doi:10.1088/1742-6596/1412/12/122006.
- [188] Bergen Davis and A. H. Barnes. The capture of electrons by swiftly moving alpha-particles. *Physical Review*, 34(1):152–156, jul 1929. doi:10.1103/physrev.34.152.
- [189] S. M. Trujillo, R. H. Neynaber, and Erhard W. Rothe. Merging beams, a different approach to collision cross section measurements. *Review of Scientific Instruments*, 37(12):1655–1661, dec 1966. doi:10.1063/1.1720077.
- [190] В. А. Бельев, Б. Г. Брежнев, and Е. М. Ерастов. Измерений сечений ионно-атомных столкновений при низких энергиях методом догоняющих

- пучков. Журнал Экспериментальной и Теоретической Физики, 3(8):321–323, feb 1966. URL: http://jetpletters.ru/ps/778/article_12031.shtml.
- [191] V. A. Belyaev, B. G. Brezhnev, and E. M. Erastov. Measurement of the cross sections of ion-atom collisions at low energies by the method of overtaking beams. *Journal of Experimental and Theoretical Physics*, 3(8):207–209, feb 1966. URL: http://jetpletters.ru/ps/1617/article_24760.shtml.
- [192] V.A. Belyaev, B.G. Brezhnev, and E.M. Erastov. Resonance charge exchange of protons and deuterons at low energies. *Journal of Experimental and Theoretical Physics*, 25(5):777–782, may 1967. URL: <http://jetp.ras.ru/cgi-bin/e/index/e/25/5/p777?a=list>.
- [193] Hidekazu Takagi. Theoretical study of the dissociative recombination of HeH^+ . *Physical Review A*, 70(2), aug 2004. doi:10.1103/physreva.70.022709.
- [194] Oldřich Novotný, Patrick Wilhelm, Daniel Paul, Ábel Kálosi, Sunny Saurabh, Arno Becker, Klaus Blaum, Sebastian George, Jürgen Göck, Manfred Grieser, Florian Grussie, Robert von Hahn, Claude Krantz, Holger Kreckel, Christian Meyer, Preeti M. Mishra, Damian Muell, Felix Nuesslein, Dmitry A. Orlov, Marius Rimmler, Viviane C. Schmidt, Andrey Shornikov, Aleksandr S. Terekhov, Stephen Vogel, Daniel Zajfman, and Andreas Wolf. Quantum-state-selective electron recombination studies suggest enhanced abundance of primordial HeH^+ . *Science*, 365(6454):676–679, August 2019. doi:10.1126/science.aax5921.
- [195] R A Phaneuf, C C Havener, G H Dunn, and A Müller. Merged-beams experiments in atomic and molecular physics. *Reports on Progress in Physics*, 62(7):1143–1180, jan 1999. doi:10.1088/0034-4885/62/7/202.
- [196] F. Grussie, A. P. O’Connor, M. Grieser, D. Müll, A. Znotins, X. Urbain, and H. Kreckel. An ion-atom merged beams setup at the cryogenic storage ring. *Review of Scientific Instruments*, 93(5):053305, May 2022. doi:10.1063/5.0086391.
- [197] W D Brandon, D H Lee, D Hanstorp, and D J Pegg. Photodetachment of the C^- ion. *Journal of Physics B: Atomic, Molecular and Optical Physics*, 31(4):751–760, feb 1998. doi:10.1088/0953-4075/31/4/022.
- [198] D. Feldmann. Infrared photodetachment measurements near thresholds of C^- . *Chemical Physics Letters*, 47(2):338–340, apr 1977. doi:10.1016/0009-2614(77)80032-8.
- [199] Michael Scheer, René C. Bilodeau, Cicely A. Brodie, and Harold K. Haugen. Systematic study of the stable states of C^- , Si^- , Ge^- and Sn^- via infrared laser spectroscopy. *Physical Review A*, 58(4):2844–2856, oct 1998. doi:10.1103/physreva.58.2844.
- [200] David Bresteau, Cyril Drag, and Christophe Blondel. Isotope shift of the electron affinity of carbon measured by photodetachment microscopy. *Physical Review A*, 93(1), jan 2016. doi:10.1103/physreva.93.013414.
- [201] V. A. Oparin, R. N. Il’in, I. T. Serenkov, and E. S. Solov’ev. Negative ion excited states and the determination of their binding energy by electron detachment by an electric field. *Journal of Experimental and Theoretical Physics*, 39(6):989–994, dec 1974. URL: <http://jetp.ras.ru/cgi-bin/e/index/r/66/6/p2008?a=list>.
- [202] Charlotte Froese Fischer. Some improved transition probabilities for neutral

- carbon. *Journal of Physics B: Atomic, Molecular and Optical Physics*, 39(9):2159–2167, apr 2006. doi:10.1088/0953-4075/39/9/005.
- [203] K. Haris and A. Kramida. Critically evaluated spectral data for neutral carbon (C I). *The Astrophysical Journal Supplement Series*, 233(1):16, nov 2017. doi:10.3847/1538-4365/aa86ab.
- [204] A. P. O’Connor, X. Urbain, J. Stützel, K. A. Miller, N. de Ruelle, M. Garrido, and D. W. Savin. Reaction studies of neutral atomic C with H_3^+ using a merged-beams apparatus. *The Astrophysical Journal Supplement Series*, 219(1):6, July 2015. doi:10.1088/0067-0049/219/1/6.
- [205] Michael L. Seman and Lewis M. Branscomb. Structure and photodetachment spectrum of the atomic carbon negative ion. *Physical Review*, 125(5):1602–1608, mar 1962. doi:10.1103/physrev.125.1602.
- [206] D. H. Lee, W. D. Brandon, D. J. Pegg, and D. Hanstorp. Cross section for photodetachment of the excited $C^- (^2D)$ ion using fast ion-laser-beam electron spectroscopy. *Physical Review A*, 56(2):1346–1350, aug 1997. doi:10.1103/physreva.56.1346.
- [207] H. L. Zhou, S. T. Manson, A. Hibbert, L. Vo Ky, N. Feautrier, and J.-C. Chang. Photodetachment of the outer shell of C^- in the ground state. *Physical Review A*, 70(2), aug 2004. doi:10.1103/physreva.70.022713.
- [208] Raphaël Marion, Kevin M. Dunseath, Mariko Terao-Dunseath, and Xavier Urbain. Absolute cross sections and asymmetry parameters for photodetachment of $C^- (^4s^0)$. *Physical Review A*, 103(2), feb 2021. doi:10.1103/physreva.103.023115.
- [209] D. Bresteau, C. Blondel, and C. Drag. Saturation of the photoneutralization of a H^- beam in continuous operation. *Review of Scientific Instruments*, 88(11):113103, November 2017. doi:10.1063/1.4995390.
- [210] Christophe Blondel, David Bresteau, and Cyril Drag. Cavity-enhanced photodetachment of H^- as a means to produce energetic neutral beams for plasma heating. *Atoms*, 7(1):32, March 2019. doi:10.3390/atoms7010032.
- [211] Masatomi Iizawa. molecular-cooling, 2022. URL: <https://figshare.com/articles/software/molecular-cooling/21076282/1>, doi:10.6084/M9.FIGSHARE.21076282.V1.
- [212] Z. Amitay, D. Zajfman, and P. Forck. Rotational and vibrational lifetime of isotopically asymmetric homonuclear diatomic molecular ions. *Physical Review A*, 50(3):2304–2308, September 1994. doi:10.1103/physreva.50.2304.
- [213] Horacio Olivares Pilón and Daniel Baye. Dipole transitions in the bound rotational-vibrational spectrum of the heteronuclear molecular ion HD^+ . *Physical Review A*, 88(3), September 2013. doi:10.1103/physreva.88.032502.
- [214] Pierre-Michel Hillenbrand, Kyle P. Bowen, Fabrice Dayou, Kenneth A. Miller, Nathalie de Ruelle, Xavier Urbain, and Daniel W. Savin. Experimental study of the proton-transfer reaction $C + H_2^+ \rightarrow CH^+ + H$ and its isotopic variant (D_2^+). *Physical Chemistry Chemical Physics*, 22(46):27364–27384, 2020. doi:10.1039/d0cp04810k.

List of Publications

The following paper is included in this thesis.

1. Masatomi Iizawa, Susumu Kuma, Naoki Kimura, Kiattichart Chartkunchand, Sakumi Harayama, Toshiyuki Azuma, and Yuji Nakano. Photodetachment Spectroscopy of Highly Excited C_2^- and Their Temporal Evolution in the Ion Storage Ring RICE. *Journal of the Physical Society of Japan*, 91(8):084302, July 2022. doi:10.7566/jpsj.91.084302.

In addition, I have contributed to several papers that are not included in this thesis. The following is a list of them.

2. S. Kosugi, R. Guillemin, O. Travnikova, T. Marchenko, D. Koulentianos, J. B. Martins, F. Hosseini, R. Püttner, D. Céolin, L. Journal, M. N. Piancastelli, I. Ismail, F. Koike, M. Iizawa, S. Sheinerman, L. Gerchikov, Y. Azuma, and M. Simon. Postcollision-interaction effects in multistep Auger transitions following Ar 1s photoionization. *Physical Review A*, 106(3):033114, September 2022. doi:10.1103/PhysRevA.106.033114.
3. Masatomi Iizawa, Satoshi Kosugi, Fumihiko Koike, and Yoshiro Azuma. The quantum and classical Fano parameter q . *Physica Scripta*, 96(5):055401, February 2021. doi:10.1088/1402-4896/abe580.
4. S. Kosugi, F. Koike, M. Iizawa, M. Oura, T. Gejo, K. Tamasaku, J. R. Harries, R. Guillemin, M. N. Piancastelli, M. Simon, and Y. Azuma. Fluorescence Time Delay in Multistep Auger Decay as an Internal Clock. *Physical Review Letters*, 124(18):183001, May 2020. doi:10.1103/PhysRevLett.124.1.
5. James R. Harries, Hiroshi Iwayama, Susumu Kuma, Masatomi Iizawa, Norihiro Suzuki, Yoshiro Azuma, Ichiro Inoue, Shigeki Owada, Tadashi Togashi, Kensuke Tono, Makina Yabashi, and Eiji Shigemasa. Superfluorescence, Free-Induction Decay, and Four-Wave Mixing: Propagation of Free-Electron Laser Pulses through a Dense Sample of Helium Ions. *Physical Review Letters*, 121(26):263201, December 2018. doi:10.1103/PhysRevLett.121.2.
6. Satoshi Kosugi, Masatomi Iizawa, Yu Kawarai, Yosuke Kuriyama, A. L. David Kilcoyne, Fumihiko Koike, Nobuhiko Kuze, Daniel S. Slaughter, and Yoshiro Azuma. Superfluorescence, PCI effects and the gradual formation of Rydberg series due to photoelectron recapture, in the Auger satellite lines upon Xe $4d_{5/2}^{-1}$ photoionization. *Journal of Physics B: Atomic, Molecular and Optical Physics*, 48(11):115003, June 2015. doi:10.1088/0953-4075/48/11/115003.